PROGRAMA DE DOCTORADO EN TECNOLOGÍAS DE LA INFORMACIÓN Y LAS COMUNICACIONES

Tesis Doctoral

# ANTENNA ARRAYS AND TARGET ELECTROMAGNETIC MODELLING TO IMPROVE PASSIVE RADAR PERFORMANCE

## (AGRUPACIONES DE ANTENAS Y MODELADO ELECTROMAGNÉTICO DE BLANCOS PARA LA MEJORA DE LAS PRESTACIONES DE LOS RADARES PASIVOS)

JAVIER ROSADO SANZ

Directora: Dra. María del Pilar Jarabo Amores
Co-Director: Dr. David Anastasio de la Mata Moya

Alcalá de Henares, 2021

# Contents

# List of Figures

# List of Tables

# List of Acronyms

| | |
|---|---|
| **3D:** | Three dimensions |
| **AA:** | Aspect Angle |
| **AF:** | Array Factor |
| **AoI** | Area of Interest |
| **AR:** | Axial Ratio |
| **BEM:** | Bistatic Equivalent Monostatic |
| **BW:** | Bandwidth |
| **CAF:** | Cross Ambiguity Function |
| **DoA:** | Direction of Arrival |
| **DPI:** | Direct Path Interference |
| **DVB-S:** | Digital Video Broadcasting-Satellite |
| **DVB-T:** | Digital Video Broadcasting-Terrestrial |
| **ECA:** | Extensive Cancellation Algorithm |
| **E-field:** | Electric Field |
| **EIRP:** | Equivalent Isotropic Radiated Power |
| **ERP:** | Equivalent Radiated Power |
| **FBR:** | Front-to-Back Ratio |
| **GLL:** | Grating Lobe Level |
| **GPS:** | Global Positioning System |
| **H-field:** | Magnetic Field |
| **HPBW:** | Half-Power Beamwidth |
| **HW:** | Half Wavelength |
| **IoO:** | Illuminator of Opportunity |
| **ISAR:** | Inverse Synthetic Aperture Radar |

**LoS:**       Line of Sight

**MSA:**       Micro-Strip Antenna

**NMLS:**      Normalized Mean Least Squares

**NULA:**      Non-Uniform Linear Array

**PCB:**       Printed Circuit Board

**PSO:**       Particle Swarm Optimization

**PR:**        Passive Radar

**RP:**        Radiation Pattern

**RCS:**       Radar Cross Section

**UAV:**       Unmanned Aerial Vehicle

**ULA:**       Uniform Linear Array

**SC:**        Scattering centres

**SAR:**       Synthetic Aperture Radar

**SIR:**       Signal-to-Interference Ratio

**SLL:**       Side-Lobe Level

# Part I

# PhD Summary

# Summary

This PhD Thesis is the result of a intense research activity focused mainly on antennas field, without compromising other aspects such as radar scenarios and targets characterization or signal processing techniques, to improve detection and tracking capabilities in passive radar systems. The research work has been carried out in the research group coordinated by Dr. María Pilar Jarabo Amores, in the frame of different national research projects: MASTERSAT (*MultichAnnel paSsive radar receiver exploiting TERrestrial and SATellite Illuminators*, TEC2015-71148-R) and KRIPTON (*A Knowledge based appRoach to passIve radar detection using wideband sPace adapTive prOcessiNg*, RTI2018-101979-B-I00); and research contracts funded by the Spanish Ministry of Defence under the framework of the European Defence Agency: MAPIS (*Multichannel passive ISAR imaging for military applications*) and JAMPAR (*JAMmer-based PAssive Radar*). The IDEPAR (Improved DEtection techniques for PAssive Radars) passive radar demonstrator developed by the research group has been the design and validation platform of the proposed solutions.

Two are the main objectives of this PhD Thesis:

- Modelling the relevant signatures of the targets and their variation along the trajectory. Depending on the passive radar resolution, the study starts with the modelling of BRCS fluctuations along the trajectory, and ends with the generation of passive ISAR images.

- Design of antenna systems fulfilling appropriate requirements defined by the surveillance channel of passive radars to improve their capabilities.

Terrestrial and satellite Illuminators of Opportunity (IoOs) have been considered, in particular those of Digital Video Broadcasting Terrestial (DVB-T) and Satellite (DVB-S) systems. Different scenarios have been studied employing those IoOs, which together with the electromagnetic characterization of targets of interest, have been employed to define the requirements that antenna systems must fulfil to improve the passive radar performance when employing each of the considered IoOs. Solutions based on microstrip technology have been designed for the radiating elements of the surveillance channel. Design techniques available in the literature have been studied and analysed, and some of them have been employed in combination with novel ones proposed in this thesis for the achievement of the challenging requirements imposed by passive radar systems. Angular

discrimination is a must as it allows the localization of targets in 3D (range, Doppler, azimuth), or even 4D (range, Doppler, azimuth, elevation) and the projection on the cartesian space. Solutions based on array geometries in the surveillance channel, combined with digital array processing techniques such as beamforming or direction of arrival estimation techniques provide that angular discrimination. In this thesis the complete design of the array antenna has been tackled: from the design of the single radiating element to the array architecture considering inter-element coupling effects and the space signal processing techniques to be applied for detection and tracking. A method based on optimization of inter-element spacing in a Non-Uniform Linear Array (NULA), considering the coupling efects, has been proposed to maximize the directivity and SLL, which will improve the targets angle estimation. This method has been applied for the design of the surveillance antenna of the passive radar demonstrator IDEPAR for exploiting multichannel DVB-T signals.

Reflectarray technology has been explored for exploiting satellite IoOs, in particular DVB-S transmitters. This technology has been selected due to the high gain required as the IoO is located at thousands of kilometres away from the targets. Two solutions have been proposed to tackle with the high gain requirement as well as a non-narrow beamwidth to provide enough angular coverage.

Also for exploiting DVB-S IoOs, commercial elements composed by a horn antenna and a LNB has been studied. An array of those elements has been designed and employed in trials to compare its performance with reflectarray's. Ambiguities occurs for small steering angles due to the high electrical size of the elements. To tackle this problem, a design based on planar geometry has been proposed.

Another objective of the presented research work is modelling targets Bistatic Radar Cross Section (BRCS) variation along their trajectory in order to better simulate real use cases and to study the potential value of BRCS fluctuations along the trajectory for detector optimization and classification features extraction. In those cases where the passive radar resolution is high enough, passive radar images can be generated. A methodology for passive images generation is proposed with the objective of generating synthetic databases for studying their potential use for the design of targets classifiers.

The main contributions of this PhD thesis are summarized as follows:

- Targets has been electromagnetically characterized through simulation of their RCS, which in combination with a deep study of the trials scenarios, their geometry and IoOs, have allowed to predict possible coverages and to define requirements for the design of antennas systems carried out in this PhD thesis. Targets RCS characterization has also been employed with classification purposes and for generating bistatic ISAR images.

- Design of two single radiating elements based on microstrip technology (patch antennas) at UHF band to acquire DVB-T signals. The designs combine different techniques to fulfil the demanding requirements imposed by passive radar systems, such as wide bandwidth, high gain combined with wide beamwidths and high front-to-back ratio. Maximum size is also limited to form an array avoiding grating lobes in a wide steering margin.

- A NULA design method to estimate the inter-element spacing that maximizes the directivity and Side Lobe Level (SLL) measured as the difference between the main beam and the highest side lobe of the antenna radiation pattern. The design method includes the coupling effects between elements in the optimization process with a novel approach that reduces significantly the computational cost without altering the results. Other planar array geometries have been proposed to achieve angular estimation in both azimuth and elevation planes for the DVB-T based system, and also for arrays acquiring DVB-S signals with commercial elements.

- Two reflectarray solutions have been proposed for DVB-S. The first one is based on a multi-beam approach through multi-feed, in which two consecutive beams provide the required angular coverage in azimuth plane. The parameters of the reflectarray have been designed and the differences between the required distribution of phases for generating each of the beams have been minimized by means of the selection of the feed position and beam steering. This solution allows the DoA estimation applying monopulse techniques. The second solution is a sectorial beam reflectarray that has been designed through a method with the novelty that the optimization is not applied to the phase distribution, but to the steering of different consecutive beams that all together provides the required sectorial beam.

Prototypes of the proposed solutions have been manufactured and characterized through measurements in anechoic chamber. The surveillance channel of IDEPAR demonstrator has been updated with the solutions proposed for each IoO, validating the suitability and performance of the antenna systems for passive radar. Trials campaigns have been carried out in different scenarios employing the designed antennas, showing good detection and tracking capabilities.

As a result of the research work carried out, two papers have been published in journals indexed in JCR and one has been recently delivered, as well as a contribution to the Boletín de Información Tecnológica en Defensa (Technological Observation and Prospective System, Subdirectorate General for Planning, Technology and Innovation of the General Directorate of Armaments and Material). It is worth mentioning the invitation to participate in three specialists' meetings (NATO-SET 284, NATO-MSG-SET 183 and 7th PCL Focus Days). Dissemination activities are completed with several contributions to international conferences.

# Part II

# Introduction and general background

# Chapter 1

# Motivation, Background and Objectives

This Chapter is intended to be an introduction to the main topics addressed in this thesis. The basics of passive radars are exposed to better capture the motivation behind this work and to highlight its main objectives and innovative contributions.

## 1.1 Motivation

Remote sensing technologies are being high-demanded by modern society, specially for control and security applications, and therefore they are under intense research. Remote sensing is defined as the action of acquiring information about something without making physical contact with it. Some well known examples of different technologies for remote sensing are: optical cameras for surveillance, infra-red sensors for detecting intrusions, Light Detection and Ranging (LIDAR) for topography and measuring concentration of chemicals in the air, near-acoustic wave sensors (SONAR, seismogram, ultrasound) for sea monitoring or earthquakes detection and of course radar technology for classical applications such as traffic control (ground, aerial and maritime), meteorology and Earth surface observation, and a recent one with raising interest: to support autonomous driving in smart vehicles.

The research work carried out in this thesis is framed within radar technology and more specifically in its branch of systems that avoid transmitting any electromagnetic signal, by taking advantage of signals from other telecommunication systems that are available in the environment: Passive Radar technology.

Passive Radars (PRs) are systems able to detect targets, and obtain information about them, employing the signal emitted for any non-dedicated transmitter available in the area of interest for the selected application [1]. Communication systems, radio-navigation and other radars are examples of non-cooperative, non-controlled transmitters which are exploited in an opportunistic manner, and are usually called Illuminators of Opportunity (IoOs). FM radio and Digital video Broadcasting-Terrestrial are of great interest: the former because long coverages are achieved, the latter due to its higher bandwidth.

Nowadays, the use of satellite IoOs is demanding an intense research effort for exploiting their availability and almost invulnerability against natural or man-made disasters. The lack of an own transmitter also defines the necessity of acquiring the signal emitted by the IoO (reference signal) for signal processing. Because of that, passive radars are usually multichannel systems, with a reference channel for acquiring the direct signal of the IoO, and a surveillance one for acquiring the radar echoes generated by the targets when they are illuminated by the IoO [2]. Single channel receiving architectures has been proposed for systems exploiting digital signals that allow the reconstruction of the reference signal from the direct one acquired by the surveillance antenna [3] [4].

In the last years, a huge amount of electronic devices have flooded everyday life, most of which have some type of transmission overflowing the electromagnetic spectrum. One of the main advantages of PR is the avoidance of electromagnetic spectrum allocation, gaining freedom in frequency selection as term of the objective application. The lack of EM emissions make PR an attractive solution for urban environments where there are already high levels of electromagnetic pollution. In this way, PR can be employed as part of autonomous vehicles or as alert system for protecting critical infrastructures, monuments or events against incoming threats such as Unmanned Aerial Vehicles (UAVs) without interfering other critical devices. The suitability of PRs for these applications is supported by the low cost of their deployment and maintenance, to a great extent because of the lack of transmitter and power consumption associated to it.

In different scenarios, as it can be a conflict area, PR also presents some advantages due to its fast deployment, the capability of undercover operation, a low probability of interception and high immunity against jammers. Besides of that, the possibility of employment different IoOs, terrestrial or satellite, provides robustness against natural disasters or human attacks and a high availability and nearby global operation.

On the other hand, the lack of a dedicated transmitter is also the source of their main drawbacks. The exploitation of signals not designed for detection purposes and the null control of transmission parameters make complex signal processing techniques necessary to detect the low energy scattered by the targets.

Modelling and simulation are key elements in the design, analysis and performance assessment of radar systems, from the engineering point of view to the operative level, including mission planning and system management, without forgetting their use in training. Radar is a complete system that comprises a wide set of technologies: antenna design, electromagnetic signal propagation, targets scattering, radio-frequency chains (high gain-power amplification approaches, low noise amplifiers, filters, frequency converters, directional couplers, power dividers, etc), power supply systems, digitalization chains and signal processing including signal waveform design and generation. Radar scenarios simulations based on models designed for the different elements play a key role, and in the present PhD Thesis they are tackled from three points of view:

- As tools for the design of passive radar system components. More specifically, electromagnetic simulators are widely used for passive radar antenna design, evaluation and optimization from the single radiation element to the array antenna design.

- Radar systems design and evaluation, focusing in the modelling of the radar cross section of targets in bistatic scenarios at digital commercial broadcasting systems, different from typical radar ones.

- Radar imaging simulation for the generation of databases needed for classifiers design and validation.

Low slow small threats such as small and mini drones are of great interest in targets' scattering simulation field. They can be easily acquired, transported any-time and anywhere and can be almost undetectable when they fly, due to having a very low signature. The use of frequencies different from those used in typical active radars opens a research field for the characterization of targets and, specially, these low small ones.

Antennas are critical in radar, and specially in passive radar, because the available IoO was not designed for detection purposes in the considered application and desired coverage area. The design of antennas for passive radars is a challenging task in which usually demanding requirements must be fulfilled. In radar applications, besides the requirement of a high gain antenna for receiving low power scattered signals, also one with wide beamwidth is required, since the surveillance area of the radar will be limited by it. Antenna theory defines the existing inverse relation between gain and beamwidth. A study of the scenario in which the PR will operate and electromagnetic characterization of the objective targets will help finding the best compromise requirements for antenna design. Besides these, the central frequency and the bandwidth of the antenna are other design parameters to consider, and they influences directly in the system resolutions and radar image formation capability.

In active radar it is common to employ antennas arrays to electronically scan a beam tackling the challenge of achieving high gain and wide angular coverage leading to so called AESA (Active Electronically Scanned Array) [5]. In the same way, it is an increasingly tendency to employ groups of antennas or arrays in passive radars, to fulfil the challenge between gain and beamwidth, to synthesize custom patterns and to provide an estimation of the angular position of the targets through array processing and Direction of Arrival (DoA) techniques.

The scope of this PhD thesis is the simulation of bistatic radar scenarios, focusing on targets reflectivity fluctuations along the trajectory and the study and design of antennas and arrays of antennas for improving the capabilities of a PR. As it is intended that the PR could employ different IoOs, the work will consider different frequencies, scenarios and requirements.

# 1.2   Background

## 1.2.1   Passive Radar

A PR is defined as a set of techniques whose main objective is to detect targets and to estimate parameters using non-cooperative signals (such as broadcast, communications, radar, or radio-navigation signals) as Illuminators of Opportunity, rather than using a dedicated radar transmitter [6].

PRs usually have two channels: the reference one that acquires the direct signal from the IoO, and the surveillance one that points towards the area of interest for the considered application and acquires the signal scattered by the targets when they are illuminated by the IoO (Figure 1.1). PR processing is based on the correlation of the surveillance signal with Doppler shifted copies of the reference one, which is called Cross-Ambiguity Function (CAF). The acquired signal is usually divided in Coherent Processing Intervals (CPIs) of $T_{int}$ s (integration time). The CAF is applied to each CPI giving as output a Range-Doppler (RD) map.
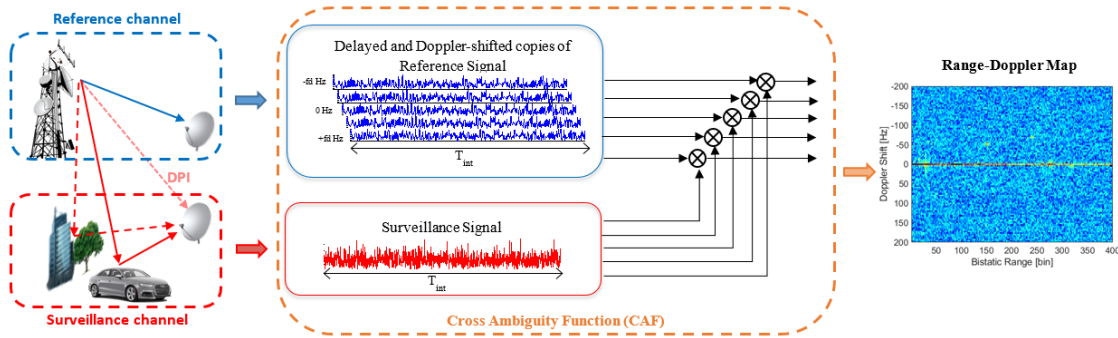


Figure 1.1: Scheme of passive radar operation: signal acquisition for generating reference (blue) and surveillance (red) signals, coherent processing based on the CAF (orange) and final RD map generated from one CPI.

The bistatic range is defined as the difference between the paths IoO-target-PR and the direct path IoO-PR: $R_B = R_{IoO-target} + R_{target-PR} - R_{IoO-PR}$. The bistatic velocity is defined in terms of Doppler shift and operation frequency: $v_B = f_D/\lambda$. The resolution of the system is defined by acquisition bandwidth and the integration time for CAF processing: the bistatic range resolution ($\Delta R_B$) depends on the acquisition bandwidth $BW_{acq}$ (Equation 1.1), while Doppler resolution ($\Delta f_D$) depends on $T_{int}$ ( 1.2).

$$\Delta R_B = \frac{c}{BW_{acq}} \tag{1.1}$$

$$\Delta f_D = \frac{1}{T_{int}} \tag{1.2}$$

The employment of different communications systems as IoOs for PR has been widely studied in literature. First, the studies were focussed on analogue television and FM broadcasting [7], [8], [9]. But these signals are characterized by low bandwidths being them dependent on information content, which is an important disadvantage taking into consideration the relation between signal bandwidth and radar range resolution. Therefore, digital signals that provide higher and data-independent bandwidths have been studied: DAB and Digital Radio Mondiale (DRM) [10], GSM [11], UMTS [12], DVB-T [13], [14], DVB-S [15] [16] [17], GPS [18] [19].

The Ambiguity Function (AF), that is the correlation of the reference signal with Doppler-shifted copies of itself, is a key tool for determining signals' detection capabilities. Signals of pseudo-random nature as DVB-T and DVB-S generate an AF of type B1, with the maximum at the origin and a pedestal that extends throughout the CAF domain [13] [20]. This AF provides good performances for PR systems. There are ambiguity peaks in both range and Doppler dimensions due to deterministic signal components required for signal decoding in the associated broadcasting system, but their locations are predictable and their effects can be reduced by signal processing. In DVB-S, ambiguity peaks are usually out of the CAF domain associated to practical operations.

Before the CAF processing, in a PR it is typical to disturbance cancellation techniques. One of the main interferences that deteriorates PR performance, besides clutter, is the Direct Path Interference (DPI). DPI is due to the acquisition of the direct signal from the IoO through the surveillance channel, which correlates with signal acquired by the reference channel and produces high level at the CAF origin and rises the CAF pedestal level. CAF contributions of echoes generated by non-desired stationary targets (ground clutter, for example) present maximum values along the zero Doppler line, with pedestal the extends throughout all the CAF domain. Different techniques for DPI and zero Doppler line interferences cancellation have been studied in literature such as Extensive Cancellation Algorithm (ECA) [21] and block Normalized Mean Least Squares (NMLS) [22] [23]. DPI can also be reduced through the antenna system, by designing an antenna with low gain in the direction where IoO is located or introducing a null by beamforming techniques if an array is being employed. This solution can be very effective if analogue beamforming techniques are applied, but requires very high dynamic ranges if digital techniques are used, because the reference signal level can be $80 - 100$ dB higher than the targets' echoes.

Other relevant sources of interference are multipaths in the reference and surveillance signals. The former is generated by the CAF delayed in time a quantity that depends on the difference between the direct signal and the ground reflected one. Again, the associated pedestal components sum up elevating the total pedestal of the CAF. Digital broadcasting signals make possible the removal of reference multipaths thanks to the possibility of reconstructing the direct IoO signal [24]. Surveillance channel multipaths are usually less important because the attenuation of the direct path is very high. They are considered as a clutter source.

Finally, in single frequency networks, the same reference signal is transmitted by different IoOs synchronously, generating ghost targets that are usually analysed after detection/tracking stages [25].

The CAF output defines the detector observation space and conventional tracking approaches use the plots generated after detection to estimate target trajectory while reducing the probability of false alarm and increasing the probability of detection.

The detector is the responsible of the decision between the presence or absence of targets in a specific location of the RD map. A common solution is the comparison between the cell amplitude and a threshold, which is usually selected to fulfil the system false alarm probability $P_{FA}$ requirements under the specific statistical conditions of the RD map. The presence of interferences, clutter or multiple targets modify the statistical distribution of the RD map along the time and between in different areas within the same CPI, making necessary the use of adaptive thresholds. Different detectors have been studied for PR systems, being the most common Constant False Alarm Rate (CFAR) ones, most of which assume Gaussian distributed disturbances [26] [27] and Likelihood Ratio (LR) detectors [28] [29] [30] .

The points declared by the detection stage can be produced by targets, clutter or other phenomena that generates false alarms. The objective of the tracker stage is the temporal analysis of the detections generated in consecutive CPIs to associate those produced by the same target and estimate its trajectory. The tracker system works as a filter that rejects the plots from false alarms and validates those that follow coherent bistatic range-velocity patterns, which are expected to be generated by real targets. Bistatic tracking schemes in RD domain are usually based on linear Kalman filter [31], [32], [33]. Azimuth information is a key for computing the target localization in Cartesian coordinates system and implementing Cartesian tracking stages. Two different strategies can be followed: the use of a first transform stage from bistatic to Cartesian coordinates, followed by a linear Kalman filter to perform the Cartesian tracking [34]; the use of extended Kalman filter or particle filters to carry out the Cartesian tracking directly from bistatic measurements [35], [36].

The generation of Inverse Synthetic Aperture Radar (ISAR) images is of great interest, because it opens the possibility of performing target classification. ISAR imaging is based on idea that a moving target changes its observation angle with respect the radar, which is equivalent to a target rotation. ISAR exploits Doppler information induced by that rotation of targets to differentiate the echoes coming from each part of the target [37]. Target must be previously detected and the trajectory information generated by the tracker can be of great relevance for image generation. In the last years, the capability of generating passive ISAR with different IoOs has been studied in literature [38], [39], [40]. The design of classifiers is an open problem because of the necessity of wideband IoOs, and databases of pre-classified examples. At this point, simulation is a key tool for evaluating the impact of frequency, bandwidth, waveform and radar scenario geometry on ISAR images from the point of view of classification and recognition applications.

## 1.2.2   Related Research Groups

In recent years, and due to its advantages, PR technology has gain a renewed interest in scientific community, giving rise to an intense research activity, literature production and even some systems have jumped to the market.

Some of the more relevant European research groups in passive radar technology are described below. Some of them also investigate in antenna systems so their main contributions in this field are highlighted. The University of Alcalá has collabore with most of them in the last years.

- **University of Naples Federico II, Italy**: In the Department of Biomedical, Electronics and Telecommunication Engineering, an intensive research focussed on statistical signal processing, radar detection, and optimization applied to radar waveforms is carried out. Relevant publications about Passive bistatic radars that use Global System for Mobile (GSM) and Universal Mobile Telecommunication System (UMTS) signals as IoOs are: [41], [42], [43], [44].

- **University College London**: The radar group of the Department of Electronic and Electrical Engineering has carried out an intensive research in radar systems and signal processing, including bistatic and multistatic radar, microdrone detection and characterization, sea clutter and maritime target analysis, and classication. They have developed NetRAD and NeXtRAD, two multistatic radar operating in S [45] and X/L band [46], respectively. Two dual polarized antennas were designed for NeXtRAD: a conical horn operating at X-band and a parabolic dish antenna for L-band [46]. Other relevant publications are [47], [48], [49].

- **University of Birmingham**. Professor Mikhail Cherniakov has been working in radar and remote sensing since 1974. He is Head of the Microwave Integrated Systems Laboratory (MISL), currently the biggest radar research group in UK universities. Examples of relevant contributions related to this PhD Thesis are: [50], [51], [52], [53].

- **Institute of Electronic Systems, Warsaw University of Technology, Poland**: In the Warsaw University of Technology, the research group on radar techniques is focussed on radar detection, parameter estimation, target tracking, classification, radar system simulations, radar imaging, SAR (Synthetic Aperture Radar) and passive radar systems.

  This group developed the family of Passive Radar Demonstrators PaRaDe (I, II and C), which operates using FM radio signals and are a basic reference in passive radar design and development [9]. It employed a circular array of 8 half-wave dipole antennas, to apply beamforming in all 360° steerings [54]. Its Digital Video Broadcasting-Terrestrial (DVB-T) demonstrator was presented in [55]. It employs commercial UHF antennas [56].

- **University of Rome, La Sapienza, Italy**: The Radar Remote Sensing & Navigation (RRSN) group belongs to the Department of Information Engineering, Electronics and Telecommunications (DIET) of the Faculty of Information Engineering, Statistics and Informatics (University of Rome, 'La Sapienza').

  An intensive activity is carried out in passive radars based on FM, Wi-Fi, DVB-T and satellite signals. In antenna terms, two commercial antennas were employed in FM radar to estimate DoA through a novel interferometric approach to improve resolution [57]. A linear array was employed to improve SNR and provide DoA estimation to a GNSS based PR [58]. Commercial parabolic dish antennas were employed for DVB-S PR [59]. A linear array of Yagi antennas is employed for the DVB-T based demonstrator [60].

  Drone reflectivity characterization related contributions are [61], [62].

- **Radar and Surveillance Systems (RaSS) center of the Italian National Interuniversity Consortium for the Telecommunications (CNIT), Italy**: RaSS centre research work is focussed on radar system design and analysis, radar data and signal processing, and electromagnetic surface and man-made target scattering modelling. An intensive research activity in passive radars using DVB-T and UMTS signals, Constant False Alarm Rate (CFAR) and Space-Time Adaptive Processing (STAP) target detection, and bistatic/multistatic Inverse SAR (ISAR) imaging formation has been carried out. The research team, under the direction of Professor Fabrizio Berizzi, has developed a dual band passive radar demonstrator to employ DVB-T and UMTS IoOs. SMARP (Software Defined Multiband Array Passive Radar demonstrator) can exploit emissions at UHF (470MHz- 790Mhz) and S (2100MHz-2200MHz) band frequencies with dual polarization (vertical and horizontal) [63], [64], [65], [66]. It employes 4 linear arrays of 8 Log-Periodic Dipoles Arrays (LDPA) patch antennas, two for each band, one for each polarization.

- **Fraunhofer FHR (Research Institute for High Frequency Physics and Radar Techniques, Germany)**: this institute investigates new and emerging IoOs, PR on moving platforms (sea, air, land), advanced signal processing techniques and builds experimental systems to proof the validity of the proposed solutions with real data. They design and developed CORA, (COVERT RADAR) capable of exploiting alternatively Digital Audio Broadcast (DAB) or DVB-T signals, using a circular antenna array with elements for the Very High Frequency (VHF) and the Ultra High Frequency (UHF) range [67], [68]; CORA11 and LORA11 [69], [70], [71], [72]; and (SABBIA, Satellite Based Bistatic Imaging Accessory)that uses Digital Video Broadcasting-Satellite (DVB-S) signals as IoO [39]. FHR also has research intensively in array processing for passive radar [73], [71].

Farther afield than just Europe, there are also some important contributions to passive radar state of art.

- China has a great contribution to this field. A GSM-based passive radar was developed in the Nanyang Technological University (Singapore) [74]. A digital television based PR for drone detection was studied at Wuhan University [75].

- In the United States, the Ohio State University (Columbus) stands out for their work in PR field specially centred in antennas array [76], [77] [78].

- In South Africa, the Council for Scientific and Industrial Research (CSIR) located in Pretoria has developed an intense research in PR, mainly employing FM and DAB signals [79], [80], [81].

Some other research groups, that are not related with passive radar but have important studies in antennas systems for radar, and therefore their contribution has been important for this PhD thesis, are summarized below:

- **The Electromagnetism and Antennas Laboratory (LEAT) from the University Cote d'Azur**, in France, has developed important antennas for radar applications, besides much more research in antennas field. Their contributions in reflectarray antennas has been specially influential for the work carried out in this thesis [82], [83], [84], [85].

- **The International Research Centre for Telecommunications and Radar (IRCTR) from Delft University of Technology**, in Netherlands, has carried out a wide research in ultra-wideband (UWB) antennas systems and array processing, automotive and ground penetrating radar (GPR) and imaging. Some of the main contributions related to this thesis are: [86], [87], [88], [89], [90], [91].

### 1.2.3 Commercial passive radar systems and demonstrators

A brief description is presented about systems and demosntrators developed by different companies [92]:

- **Leonardo**, a subsidiary of Leonardo S.p.A. (Italy), developed a Passive Coherent Location radar that exploits FM signals as IoO, called AULOS, to provide detection and tracking capability for defence and homeland security applications [93], [94], [95]. SELEX has been carried out an intense research activity in passive radar technology, developing improved AULOS passive radar that exploits multiple FM transmitters and analyses multi-band configurations such as DVB-T or GSM [96].

- **AIRBUS DEFENCE AND SPACE** designed a multiband passive radar demonstrator capable of processing DVB-T Single Frequency Network (SFN), DAB-SFN and 8 FM channels simultaneously, which was evaluated in various measurement campaigns followed by an intensive theoretical analysis of the results [97]. Multistatic configurations were presented in [98].

- **HENSOLDT** offers passive radar based solutions in its portfolios for air surveillance, and ground based air defence. TwInvis passive radar exploits FM transmissions and it is capable of detecting larger aircrafts at 250km, and DAB/DVB-illuminators for shorter ranges and smaller aircrafts.

- **ERA** The demonstrator Silent Guard operates at FM band being able to acquire up to 8 FM channels.

- **THALES** Ground Alerter 100 (GA100) multistatic passive radar that can use FM, DVB-T or a combination of FM and DVB-T transmitters, field proven for air surveillance (gap filler for detection of small targets at low altitude and low speed), and site protection sites through operational use; leveraged by numerous patents and years of product improvement.

- **PIT-RADWAR S.A.** is one of the leading suppliers of professional electronic equipment for the Armed Forces of Poland. Its Passive Location System (PLS) combines two passive subsystems: PCL subsystem (Passive Coherent Location) and PET subsystem (Passive Emitter Tracking) for a multistatic (4 identical PCL/PET stations), multiband (FM, DVB-T, GSM) and multimode operation. PET subsystem detects aircrafts on the basis on emissions of their on-board transmitters: radars (ELINT), communication (COMINT), navigation (NAF) and IFF (IFF) signals.

- **PATRIA** has developed MUSCL, a passive radar system for air surveillance exploiting FM and DVB-T signals simultaneously. It that can operate in standalone mode or in networked mode using multiple stations. Due to FM lower frequency high detection ranges are achieved and it provides classification in two classes: fixed-wing or rotary-wing.

## 1.3   Objectives

Main objectives of this PhD Thesis are the following:

- Contribution to the improvement of bistatic radar simulation scenarios focusing on targets reflectivity modelling under constraints defined by passive radars.

- Design of antenna systems to improve the performance of a passive radar employing terrestrial and satellite IoOs.

The technological demonstrator developed in the University of Alcalá research group coordinated by Dr. María Pilar Jarabo Amores, is the target system for the antennas developed in this thesis. Therefore it will be employed to study the requirements and to validate the solutions proposed.

The work carried out in thesis can be divided in smaller targets, each of them defining a research line, to achieve the final objective:

- **Targets electromagnetic characterization.** The study of the reflectivity of the targets as a function of the position where the wave falls upon it and the one in which the wave is reflected towards the PR is carried out through the Bistatic Radar Cross Section (BRCS). The characterization of the BRCS of the targets of interest allows to estimate coverages and, therefore, provides useful information for defining the requirements of surveillance antennas. Targets BRCS is not only important for detection in PR, but also can be employed with classification purposes, by studying the fluctuation of BRCS from different targets following the same trajectory or by simulating bistatic ISAR images through the multi-frequency BRCS of a set of incidence and reflection angles.

- **Scenarios study for different IoO geometries and surveillance antenna system requirements definition.** Terrestrial and satellite IoOs geometries are studied in different scenarios in order to define the main antenna design requirements. Range coverage studies will lead to the definition of the required gain, while the area and targets of interest lead to the required beamwidths in azimuth and elevation planes. Radar systems, active and passive, usually requires high gain combined with high beamwidths which entails a great challenge for antenna designers. If an array of antennas is selected for achieving angular localization of targets, the maximum size of single elements will be defined through array pattern study to avoid grating lobes.

- **Single radiating element design for DVB-T as IoO.** The design of an antenna with characteristics suitable for array grouping will allow an improvement in PR performance. An antenna design with good impedance matching will reduce its noise figure. Size, gain and radiation characteristics will be also constrained by the requirements defined by the antenna array that will be composed of a set of such single radiating elements. Critical parameters are the single antenna beamwidths (that defines the angular coverage of the array), the number of elements and their distribution along the array geometry (that defines final gain, side lobe level, and DPI rejection). The design of an array will lead to tracking improvement as angular information will be provided. Low cost and fast fabrication solutions, as there are microstrip technology antennas (MSA), will make the system more attractive for a future jump into market of an evolution of the actual technological demonstrator.

- **Array design for DVB-T as IoO improving SLL and directivity.** Different array geometries are studied with commercial and designed elements. The objective is to achieve an array design that improves the directivity, which means better detection and angular resolution and minimizes side-lobe level (SLL) to achieve a more precise estimation of angle of arrival avoiding ambiguities.

- **Antenna design for DVB-S as IoO.** A PR taken advantage of satellite television signals (DVB-S) is characterized by the high propagation losses due to the high distances from transmitters and the high frequency (X/Ku bands). For this reasons surveillance antennas with high gain are required, but with enough beamwidth for being able to track targets during some seconds to discriminate them from false alarms. Different solutions based on reflectarray antennas technology are studied to provide the PR all the advantages of employing geostationary satellite IoOs, such as high availability and robustness against natural and human made disasters.

- **Study of array geometries for DoA estimation in DVB-S based PR.** Commercial elements will be employed for designing an array geometry that provides to the PR an estimation of direction of arrival (DoA) from targets, employing DVB-S signals. The main challenge of array design at these frequencies ($11-12$ GHz) is that commercial elements usually have a size much greater than half wavelength , which produces grating lobes reducing considerably the steering margin and leading to ambiguities in DoA.

## 1.4   Related research projects

This PhD Thesis has been carried out in the frame of different research projects developed by the University of Alcalá research group coordinated by Dr. María Pilar Jarabo Amores.

### 1.4.1   National research projects

- **MASTERSAT: MultichAnnel paSsive radar receiver exploiting TERrestrial and SATellite Illuminators**

  – Funding organization: Spanish Ministry of Economy and Competitiveness (MINECO). TEC2015-71148-R (01/2016-12/2018)

  – Objectives: Follow-on of the IDEPAR project, focusses on the study of satellite IoOs and the impact of the new DVB-T frequency allocation after the first digital dividend; array antennas and digital array signal processing techniques for the improvement of angular coverages and resolutions; BRCS modeling (targets and clutter); improved detectors ad trackers in 2D (range,Doppler) and 3D (range, Doppler, azimuth); optimization of processing algorithms and analysis of their implementation on multicore systems.

– Outcomes: IDEPAR demonstrator, developed in a previous project, was updated for performing digital array signal processing in DVB-T band and for acquiring and processing DVB-S and GPS signals. The use of DVB-T PRs for drone detection was identified as an application of great interest. The research group was invited to deploy IDEPAR during the development of the CONDOR trials promoted by the Spanish Ministry of Defence. In these trials, different antidrone systems were validated. IDEPAR could be deployed thanks to its null radiation that guaranteed the proper performance of the systems to be validated.

- **KRIPTON: A Knowledge based appRoach to passIve radar detection using wideband sPace adapTive prOcessiNg**

    – Funding organization: Spanish Ministry of Science, innovation and Universities. RTI2018-101979-B-I00 (01/2019-12/2021)

    – Objectives: Performance improvement of DVB-T based PR technology through the exploitation of wideband signals to increase range resolution, and the use of adaptive wideband Digital Array Signal Processing techniques to increase angular resolution with angular coverages of interest in radar applications. Design of knowledge based detection and tracking techniques based on statistical characterization of UHF high resolution 3D clutter in multi-static configurations. Proposal, implementation and test of a cognitive PR architecture based on adaptive UHF signal processing of wideband UHF signals.

    – Outcomes: IDEPAR was updated for acquiring simultaneously up to 8 channels with an instantaneous bandwidth of 100MHz. A new antenna array and 3D detection and tracking techniques were designed and implemented in bistatic and multistatic scenarios. Nowadays the project is in progress.

## 1.4.2 European research projects and contracts

- **MAPIS: Multichannel passive ISAR imaging for military applications**

    – Funding organization: Spanish Ministry of Defence/European Defence Agency (EDA). Ad Hoc R & T Project (Category B). 12/2014 -12/2017.

    – Consortium: CNIT, Selex Electronic Syst., MBDA, FHR, UAH, Warsaw University of Technology, MTA-SZTAKI, Budapest University of Technology and Economics, PITRADWAR (Poland).

    – APIS Follow-On, that focused on ISAR images generation for classification purposes in military scenarios defined in collaboration with military experts. APIS (Array Passive ISAR adaptive processing) was funded by EDA, under

the Joint Investment Programme Innovative Concepts and Emerging Technologies (JIP-ICET), A-0900-RT-GC-ICET. 2010-2012. APIS main outcomes: first study about PR suitability in security and defense applications using digital IoOs; development of a PR demonstrator for detection and ISAR images generation.

– UAH role: definition of scenarios and system requirements, statistical studies of clutter, design of improved detectors; design and validation of classifiers.

- **JAMPAR: Jammer-based Passive Radar**

  – Funding organization: Spanish Ministry of Defence/EDA. Ad Hoc R & T Project (Category B). 01/2020 -01/2023.

  – Consortium: PITRADWAR and Warsaw University of Technology (Poland); UAH and INDRA (Spain); Norwegian Defence Research Establishment (Norway); FHR (Germany).

  – JAMPAR focused on the exploration of friendly and hostile jammers as illuminators of Opportunity for the detection, tracking and and ISAR imaging of aerial targets in border areas.

  – UAH role: analysis of radar scenarios, definition of system requirements, statistical studies of clutter for the design of improved radar detectors, detection and tracking in multistatic configurations, design and validation of classifiers, and update of IDEPAR for participating in JAMPAR trials defined to validate proposed solutions for detection, tracking, imaging and classification.

## 1.4.3 Projects funded by the University of Alcalá

- **PARSY3D-D&T (Array signal processing in PAssive Radar SYstems for 3-D Detection and Tracking of terrestrial targets, CCGP2017-EXP/056)**. Objective: Improvement of PR 3D detection and tracking techniques for ground traffic monitoring. Digital beamforming algorithms, 3D detection and tracking schemes combining CFAR and DoA techniques. Study and proposal of solutions based on artificial intelligence approaches.

- **DRONCIP (NRT DRONe detection with DBV-T based passive radar for Critical Infraestructure Protection, CCG19/IA-030)**. Objective: Estimation of DVB-T based PRs coverages for the detection of UAVs. Wideband coherent signal processing techniques for PR detection and tracking. Digital signal processing techniques for defining 3D input spaces for detection and tracking. Definition of a hardware architecture for Near Real Time processing.

## 1.5 Structure of the document

This PhD Thesis is structured in four main parts as followed:

- The first part contains the summary of the thesis.

- The second part, *Introduction and general background* comprises three chapter. This first chapter has introduced the topics of this thesis as well as it has explained the motivation and objectives that guide the research work carried out and the background in which it is frame in, passive radar systems. Chapter 2 explains the basics on antenna theory and array and details the state of art in this field that is the main one of this thesis. Chapter 3 details the characteristics of the PR demonstrator that will be the objective system for the solutions proposed in this PhD thesis, and therefore, it will set important requirements.

- The third part details the main research and results carried out during the development of this PhD thesis.

  - Chapter 4 defines the radar scenarios that will be employed for trials to validate the proposed solutions, and presents the electromagnetically characterization of targets of interest. Targets are characterized through simulation of their bistatic RCS along trajectories which is employed to estimate coverages in the trials scenarios, to define requirements of antenna systems and to analyse its fluctuation with classification purposes. The generation of bistatic ISAR images from the complex bistatic RCS is also considered.

  - Chapter 5 details the design of two single radiating elements for a PR employing DVB-T as IoO, each one with the objective of forming different arrays for horizontal and vertical polarization. A method for designing a NULA by optimizing the inter-element spacing, considering coupling effects, to improve the array performance is also presented. Prototypes of both antennas were manufactured and the results of its characterization in anechoic chamber is shown as well as results achieved in different trials campaigns that validated the designs.

  - Chapter 6 proposes solutions based on reflectarray technology for employing DVB-S signal as IoO. Two different multi-beam approaches are presented, the first one is based on multi-feed while the second employs an optimization process to generate a sectorial beam from multiple contiguous beams created by the same feed. The second method was employed to create a design to be manufactured employing commercial elements. The results of characterization in anechoic chamber measurements and validation in PR trials are presented.

– Chapter 7 present the suitability of employing an antenna array based on commercial single radiating elements for DVB-S as IoO. The size of the element causes the appearance of grating lobes for small steering angles, so a planar geometry is proposed to tackle with this problem.

• The last part summarizes the conclusions of the work developed during the thesis (Chapter 8), defines some future research lines (Chapter 9) and presents the contributions achieved as a consequence of the work carried out in this thesis (Chapter 10).

# Chapter 2

# Antenna Systems

An antenna is *the part of a transmitting or receiving system that is designed to radiate or to receive electromagnetic waves* [99]. The antenna is the element that allows the bi-directional transition between a guided media and the free space (Figure 2.1), which makes them a fundamental structure in wireless communications.
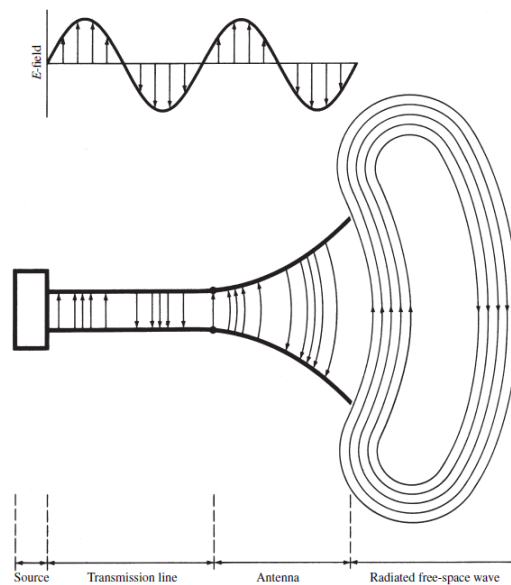


Figure 2.1: Antenna as transition element [100]

.

Transmitting and receiving electromagnetic waves are not the only tasks of the antenna. It is a directional device that reinforces radiation in some directions and mitigates it in others when operating in transmit mode. In reception mode, it has a higher sensitivity in the directions in which the radiation intensity is greater in transmission mode, and it tends to reject signals that come from directions in which the radiation intensity in transmission mode is lower (reciprocity theorem). This feature, that involves that antennas are directional devices, gives rise to some important characteristic parameters usually employed in antenna design.

# 2.1   Antenna Characteristic Parameters

In this section, the parameters that characterize an antenna are presented and defined. These terms will be broadly used along all the document.

Most of the parameters defined in this section regards to the fields surrounding the antenna. The characteristics of those fields vary as a function of the distance from the antenna where they are considered (r) and the maximum electrical size of the antenna. Therefore, antenna fields are classified in three regions from nearest to furthest:

1. Reactive near-field region that extends just from the antenna to $r = 0.62\sqrt{D^3/\lambda}$, being D the maximum physical dimension of the antenna and lambda the wavelength. It is a region dominated by reactive fields: the electric and magnetic fields are out of phase to each other and they store energy instead of radiating it.

2. Radiating near field or Fresnel region, in which radiating fields begin to emerge but the shape of the pattern can still vary with the distance from the antenna, $r$.

3. Far field region also called Fraunhofer region. It is dominated by radiating fields and in it the shape of the pattern does not change with r. The fields in this region behave as locally plane waves. This region extends from $r > 2D^2/\lambda$ and must fulfils two conditions: $r \gg D$ and $r \gg \lambda$.

The main parameters that characterize an antenna are:

A. **Input Impedance and reflection coefficient.** The input impedance or antenna impedance is defined as the ratio of voltage to current at the terminal of the antenna.

   In general, the antenna impedance is complex. The real part can be divided in losses resistance $(R_L)$ and radiation resistance $(R_r)$. The radiation resistance is related with the power that is radiated away if the antenna operates as transmitter or the power absorbed by the antenna if it operates as receiver. The imaginary part $(X_A)$ is related to the portion of energy that is stored in the near field of the antenna. In this way the antenna resistance is divided in losses resistance and radiation resistance with its Thevenin equivalent circuit shown in Figure 2.2.

$$Z_A = R_A + jX_A[\Omega] \tag{2.1}$$

$$R_A = R_L + R_r[\Omega] \tag{2.2}$$

   The reflection coefficient $\Gamma$ is also known as $s_{11}$ parameter when the antenna is modelled as a 1-port device and scattering parameters are calculated with respect to the impedance characteristic of the feeding line. It determines the power reflected from the antenna due to mismatch with respect to the feeding line, and defines the
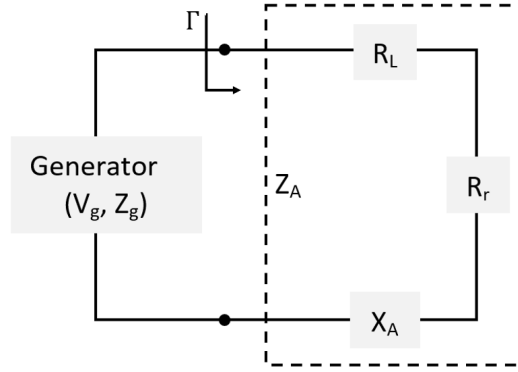
Figure 2.2: Thevenin equivalent circuit of an antenna operating as transmitter.

Return Loss RL (Equation 2.3), which is directly related to the Voltage Standing Wave Ratio measured in the feeding line at the antenna terminals (Equation 2.4).

$$RL = -20 \cdot log_{10}|\Gamma| \ [dB] \tag{2.3}$$

$$VSWR = \frac{1 + |\Gamma|}{1 - |\Gamma|} \tag{2.4}$$

B. The **Antenna Efficiency** $\eta_A$ measures the ratio of the radiated power relative to the power delivered to the antenna. Efficiencies below 100% are due to mismatch losses (or return losses) and conduction and dielectric losses due to the non-ideal behaviour of the materials used for building the antenna. The losses due to conductor and dielectric materials define the radiation efficiency of the antenna $\eta_r$.

C. **Radiation Pattern** (RP) is the graphical representation of the radiation properties of an antenna. It is usually measured in the far-field region which is the region where the antenna radiation characteristics remains independent of distance and electromagnetic waves can be considered locally plane.

3D radiation pattern is conveniently represented in spherical coordinates. However, most of the times, the antenna radiation characteristic can be extracted from two bi-dimensional cuts. These two cuts, that are usually represented in polar charts, are the azimuth and elevation planes or the E and H planes. Azimuth plane is defined for $\theta = 90°$ while elevation one is defined for $\phi = 0°$ (Figure 2.3). E-plane is defined by the polarization of the E-field in the direction of maximum radiation, while H-plane is defined by H-field, being therefore orthogonal to E-plane.

The main antenna properties gathered in the radiation pattern are: polarization, directivity, gain, beam-widths and side lobes ratios.
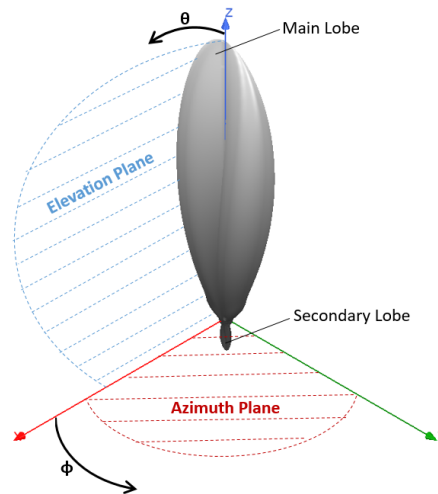
Figure 2.3: Coordinate system definition and 3D radiation pattern example.

The shape of the radiation pattern defines the service that antenna could provide. In this term, antennas are classified as:

(i) **Isotropic.** The power is radiated equally in all the directions of the space. This is an ideal model, physically unrealisable.

(ii) **Omnidirectional.** The radiation pattern shows symmetry of revolution with respect to an axis.

(iii) **Directional or sectoral.** The power is concentrated in an angular cone or fan pointing to some direction of the space.

D. **Polarization.** Antenna polarization refers to the polarization of the E-field waves that the antenna is able to transmit or receive. The polarization of a local plane wave is defined in a given direction and at a point in its far-field region [99]. The direction of maximum radiation is the one usually employed for defining the antenna polarization.

The wave polarization is the property that describes the change of direction of the E-field along the time while the wave is propagating towards a direction perpendicular to E-field and H-field. The polarization can be linear, circular or elliptical as a function of the geometric shape defined by E-field direction change.

The axial ratio (AR) is the parameter employed to discern the type of polarization of an antenna. The AR defines the ratio between the orthogonal components of the E-field. The AR measured in decibels classifies the antenna polarization as:

(i) **Linear:** if $AR \to \infty$

(ii) **Circular:** if $AR \approx 0$ dB

(iii) **Elliptical:** if $AR \approx 1 - 2$ dB

Antennas designed in this thesis will be linearly polarized to optimally match with the signals of opportunity employed by the passive radar. If $\hat{e}_T$ and $\hat{e}_R$ are the unitary polarization vectors of the incident electric field and the receiving antenna, respectively, the polarization loss factor is defined as (Equation 2.5).

$$PLF = |\hat{e}_T \cdot \hat{e}_R|^2 \tag{2.5}$$

E. The **Directivity** of an antenna is defined as the ratio of the radiation intensity in a given direction to the radiation intensity averaged over all directions (Equation 2.6) [99].

The directivity of an antenna represents its capability to increase the radiation transmitted or received from some directions while decreasing it in others.

$$D(\theta, \phi) = \frac{U(\theta, \phi)}{P_{rad}/4\pi} \; [dB] \tag{2.6}$$

F. The **gain** of an antenna is usually one of the most important parameters that define the requirements of an antenna for a telecommunication system because it affects directly the coverage of the system.

The gain or absolute gain of an antenna in a given direction, is defined as the ratio of the radiation intensity in that direction to the one that would be produced if the power accepted by the antenna were isotropically radiated [99]. By this reason, the gain is measured in dBi, which means decibels relative to an isotropic radiator. This definition includes the directional properties of the antenna and its radiation efficiency (Equation 2.7).

$$G(\theta, \phi) = \eta_r \cdot D(\theta, \phi) \; [dBi] \tag{2.7}$$

A variation of this parameter, that is usually more appropriate when it is employed to calculate link budgets or system coverages, is the term realized gain. The realized gain of an antenna is equal to its gain reduced by the losses due to impedance mismatch.

G. **Radiation Pattern Lobes.** A lobe is the region of the pattern where a local maximum of radiation intensity is found (Figure 2.3). In a typical radiation pattern different lobes can be found:

(i) **Main lobe** is the one that contains the direction of maximum radiation.

(ii) **Secondary or Side lobes** are each one of the lobes in a direction different from the maximum radiation. A special side lobe is the back lobe, defined as the one pointing to the opposite direction of the main one.

These concepts define two important parameters of antennas: SLL and FB-ratio.

The **Side-Lobe Level** (SLL) is the difference between the maximum directivity of the highest side lobe and the maximum directivity of the antenna.

The **Front-to-Back ratio** (FBR) is the difference between the maximum directivity of the back lobe and the maximum directivity of the antenna.

H. The **Half-Power Beamwidth** (HPBW) of an antenna, which is usually shorten as the beamwidth of an antenna, is defined as the angle between two points of the main lobe in which the radiation intensity is one-half the maximum value [99]. The beamwidth of an antenna symbolises the angular margin of directions where it can radiate or receive properly. According to the cut employed for measuring the HPBW, the elevation (HPBW$_e$) or azimuth beamwidth (HPBW$_a$) of the antenna is defined.

Directivity and HPWB in antennas are inversely proportional as it is defined in Equation 2.8 for sectoral antennas [101], being $\theta$ the HPBW$_e$ and $\phi$ the HPBW$_a$ measured in degrees and restricted to $\phi \leq 120°$ and $\theta \ll \phi$.

$$D = 10 \cdot \log_{10} \left( \frac{36400}{\theta \cdot \phi} \cdot e^{\frac{\theta \cdot \phi}{36400}} \right) \ [dB] \tag{2.8}$$

I. The **phase center** of an antenna is defined as a point such that, if it is taken as the center of a sphere which radius extends into the far field, the phase of a given field component over the surface of the radiation sphere is essentially constant, at least over that portion of the surface where the radiation is significant [99].

The phase center is really useful in certain antenna measurements and, in the case of reflector antennas, is the point of the feed employed for the design.

J. **Bandwidth** (BW) is the range of frequencies in which the antenna is able to work properly, that means the antenna is able to radiate or receive energy. It is also called impedance matching bandwidth because it corresponds to the frequencies where the antenna input impedance is matched to the transmission line.

The standardised criteria for determining the bandwidth of an antenna is that the return loss must be less than $-10$ dB [100], which means that the reflected power is only 3.16% of the delivered one, or that the $VSWR < 2$.

Even though the bandwidth is measured as the range of frequencies in which the antenna is matched, there must be also fulfilled that the radiation properties remains stable at that frequencies.

## 2.2 Wire and Aperture Antennas

### 2.2.1 Wire Antennas

Wire antennas are the simplest type. They are made up of a single conductor strand that can follow different shapes (linear, circular, rectangular, helix...). The radiation mechanism in this type of antennas is based on the movement of charge carriers inside the conductor, which creates an electric current that is responsible of the electromagnetic radiation.

The main antenna in this group is the Half Wavelength (HW) Dipole. It is formed by two sections or strands of conductor material, both starting at the same point, which is the feeding point, but they are laid out linearly in opposite directions. The total length of the two strands is around the half of the wavelength $\lambda$ at the resonance frequency. In the case of the HW Dipole the current is maximum in the middle of the antenna and, due to its length, minimum or even zero at the endings located at $\lambda/4$ (Figure 2.4(a)). As the radiation is due to current, this antenna produces a radiation pattern with toroidal shape (omnidirectional in the plane normal to the dipole direction and directional in the opposite with zero radiation in the direction of the antenna), as it is shown in Figure 2.4(b). The polarization in this type of antennas is linear and parallel to the wire.



(a) Current density distribution

(b) 3D radiation pattern
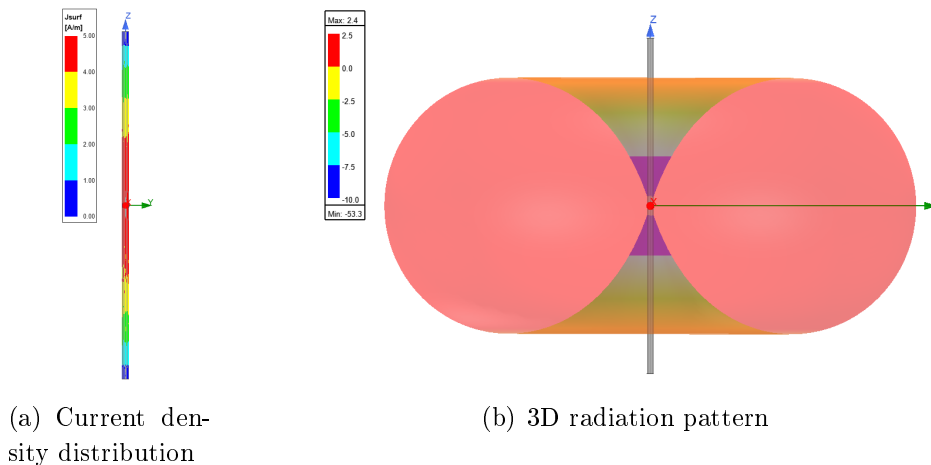
Figure 2.4: HW Dipole antenna modelled in Ansys HFSS and simulated at 275 MHz showing its current density distribution and the toroidal radiation pattern.

### 2.2.2 Aperture Antennas

Aperture antennas are made up of conductor material surrounding vacuum or other dielectric material. The radiation mechanism is based on the fact that the E-field is collimated inside the conductor material and guided through it towards the aperture where it is radiated to the free space.

The simplest antenna in this group is a waveguide with one ending open to the free space. Usually, the aperture in the open ending is increased gradually to avoid an abrupt impedance change between the the waveguide and the free space, giving rise to horn antennas. Figure 2.5(a) shows how the E-field created by $TE_{10}$ mode is guided through the horn from the feeding to the free space, being responsible of the radiation. Horn antennas are characterized by a high directivity pencil beam (Figure 2.5(b)) and wide bandwidth, up to $30\% - 40\%$ in X-band, which make them suitable and widely used in satellite and point-to-point communications. They can be employed alone, forming an array or as the feed of a reflector antenna system.

Polarization in horn antennas is managed by the polarization of the mode excited in the waveguide, being linear in most of the cases.

The most common horn antennas are pyramidal and conical ones. The design of these antennas can be carried out following the expressions compiled in Table 2.1 as function of desired frequency ($f_c$) and gain ($g$ in natural units, or $G$ in dBi).



(a) $TE_{10}$ mode E-field in horn antenna

(b) Horn model and pattern
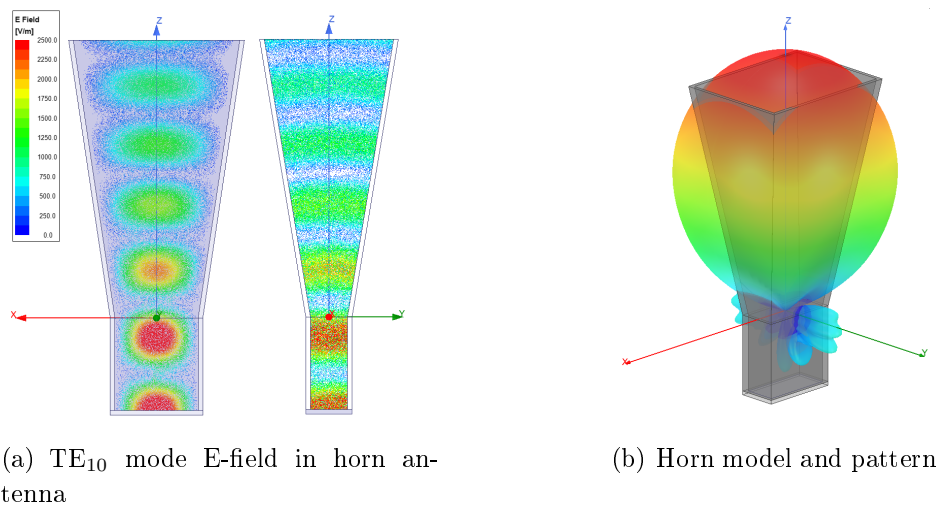
Figure 2.5: WR90 pyramidal horn antenna modelled in Ansys HFSS and simulated at 10 GHz showing the E-field distribution and the pencil-beam radiation pattern.
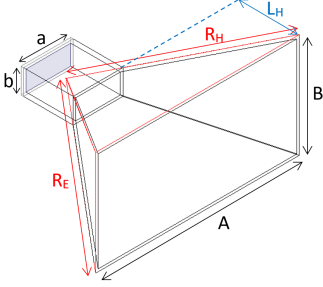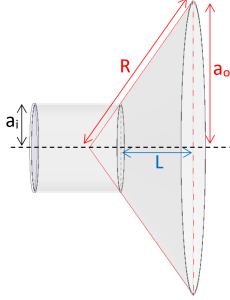
| Pyramidal Horn [102] | Conical Horn [103] |
|---|---|
|  |  |
| $$f_{c,mn}^{TE} = \frac{c}{\sqrt{\mu_r \varepsilon_r}} \sqrt{\left(\frac{m}{2a}\right)^2 + \left(\frac{n}{2b}\right)^2}$$ $$A = 0.096a \cdot g^{0.232} + 0.42\lambda \cdot g^{0.503} - 0.193b$$ $$R_H = A\sqrt{\frac{1}{4} + \left(\frac{A}{3\lambda}\right)^2}$$ $$L_H = (A-a)\sqrt{\left(\frac{R_H}{A}\right)^2 - \frac{1}{4}}$$ $$B = \frac{1}{2}\left(b + \sqrt{b^2 + 8L_H\lambda}\right)$$ $$R_E = \frac{B}{2}\sqrt{1 + \left(\frac{B^2}{\lambda}\right)}$$ | $$a_i = \frac{3\lambda}{2\pi}$$ $$a_o = \frac{\lambda}{2\pi}\sqrt{10^{(G+2.91)/10}}$$ $$R = \frac{4a_o^2}{3\lambda}$$ $$L = \frac{a_o - a_i}{tan\theta}$$ $$\theta = arcsin(\frac{a_o}{R})$$ |

Table 2.1: Pyramidal and conical horn antenna schematics and main design expressions.

## 2.3 Microstrip Antennas
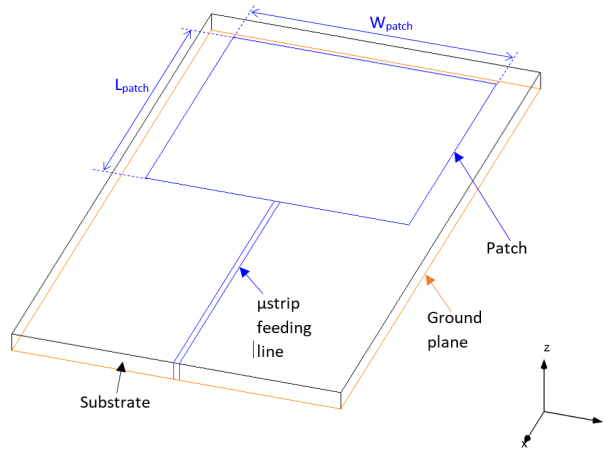


Figure 2.6: Schematic of a microstrip antenna showing its main parameters.

A MicroStrip or $\mu$strip Antenna (MSA), also called a patch antenna, is a radiating element built in a high conductivity metal over a substrate [100]. The main parts of a microstrip antenna are illustrated in Figure 2.6:

1. **Ground plane** is made of a high conductivity metal which is usually located at a different layer than the patch, being both isolated by a dielectric substrate. A peculiar case is the coplanar MSA [104] in which the ground plane is located in the same layer than the patch, reducing the radiation losses.

2. **Substrate** is the dielectric layer that holds the patch. Its thickness has direct influence in the bandwidth of the antenna. Two characteristics of the dielectric material, such as the relative permittivity or relative dielectric constant ($\varepsilon_r$) and the loss tangent ($tan\delta$), define the performance of the antenna. $\varepsilon_r$ defines the slow down of the propagation speed on an electromagnetic wave in the material compared to the vacuum and, therefore, the decrease in wavelength that determines the operation frequency. $tan\delta$ defines the radiation losses due to the substrate so it has influence in the maximum gain of the antenna.

3. **Feeding** or excitation of the patch is important to achieve impedance matching at the desired frequencies, and it can be made through different methods. Direct methods in which the feeding touches directly the patch include coaxial probe feeding and $\mu$strip line feeding. Indirect methods, in which the feeding is made through electromagnetic coupling between the feeding line and the patch, include proximity coupling and aperture coupling. The performance of each feeding method in terms of matching and bandwidth for a rectangular patch antenna at 5.5 GHz is summarized in table 2.2 [105].

|                | Coaxial Probe | $\mu$strip Line | Proximity Coupling | Aperture Coupling |
| -------------- | ------------- | --------------- | ------------------ | ----------------- |
| $|S_{11}|$     | -19.77 dB     | -11.29 dB       | -49.89 dB          | -31.29 dB         |
| Fractional BW  | 4.68%         | 6.68%           | 7.49%              | 10.56%            |

Table 2.2: Comparative study of different feeding methods in a rectangular patch antenna at 5.5 GHz [105].

4. **Patch** is made of a high conductivity metal, usually copper. The basic patch shapes are rectangular and circular, which sizes, length (L) and width (W) for rectangular patches and radius (r) for circular ones, are calculated from Equations 2.9, 2.10 and 2.11, respectively. However, the shape of the patch is usually modified to achieve a better performance in terms of some parameter, so endless different shapes can be found in the literature.

$$L = \frac{\lambda_0}{2\sqrt{\varepsilon_{r_{eff}}}} - 2 \cdot \Delta L \qquad (2.9)$$

$$W = \frac{\lambda_0}{2} \sqrt{\frac{2}{\varepsilon_r + 1}} \tag{2.10}$$

Being $\varepsilon_{r_{eff}} = \frac{\varepsilon_r + 1}{2} + \frac{\varepsilon_r - 1}{2\sqrt{1 + 12 \cdot \frac{h}{W}}}$ and $\Delta L = 0.412h \cdot \frac{\left(\varepsilon_{r_{eff}} + 0.3\right) \cdot \left(\frac{W}{h} + 0.264\right)}{\left(\varepsilon_{r_{eff}} - 0.258\right) \cdot \left(\frac{W}{h} + 0.8\right)}$

$$r = \frac{F}{\sqrt{1 + \frac{2 \cdot h}{\pi \cdot \varepsilon_r \cdot F} \cdot \left[log\left(\frac{\pi \cdot F}{2 \cdot h}\right) + 1.7726\right]}} \tag{2.11}$$

Being $F = \frac{8.791 \times 10^9}{f_0 \cdot \sqrt{\varepsilon_r}}$

This type of antenna presents interesting advantages for modern communications: versatility in radiation pattern and polarization characteristics, reduced size, quasi-planar structure with low height, light weight, easy fabrication and low cost. Basic MSA have important drawbacks in key performance parameters such as narrow bandwidth, low gain and poor efficiency, nevertheless these parameters can be improved through the application of different design techniques, which has stimulated large research work in this field since they were invented a half century ago [106].

### 2.3.1 MSA Radiation Mechanism and pattern

The radiation mechanism of a rectangular patch antenna of dimensions $L \times W$ (Figure 2.6), can be explained through the multimode cavity model. This model states that any microstrip radiator is equivalent to an open cavity bounded by the patch and the ground plane as well as the open edges can be represented by radiating magnetic walls. This kind of cavity supports multiple modes $(mn)$ in the same way than a completely enclosed metallic cavity. The electric field in the cavity is calculated as the sum of the fields associated with each mode (Equation 2.12). This expression assumes that the fields are z-directed, with no variation in the $z$-direction, which is correct for thin substrates but can give rise to inaccurate solutions in case of thick substrates.

$$E_z(x, y) = \sum_m \sum_n C_{mn} \cdot cos\left(\frac{m\pi}{L}\right) x \cdot cos\left(\frac{n\pi}{W}\right) y \tag{2.12}$$

In the fundamental case of a rectangular patch, the E-field magnitude variation along the patch for the dominant mode $TM_{10}$ is represented in Figure 2.7(a). It can be seen how the fields are maximum near the edges in the resonant direction, which are separated approximately $\lambda_g/2$ (L), and null along a line orthogonal to the resonant direction in the middle of the patch. In a MSA the fringing fields between the periphery of the patch and the ground plane are the responsible of the far field radiation. Fringe field present an oscillatory behaviour at left and right sides of the patch, which made them cancel in the far field, so the top and bottom edges fringe fields are the main contributors to the

far field radiation (Figure 2.7(b)). Therefore, in a rectangular patch MSA, the radiation mechanism consist of two radiating slots separated $\lambda_g/2$.



(a) TM$_{10}$ E-field.  Top and right side views.



(b) TM$_{10}$ Fringe fields
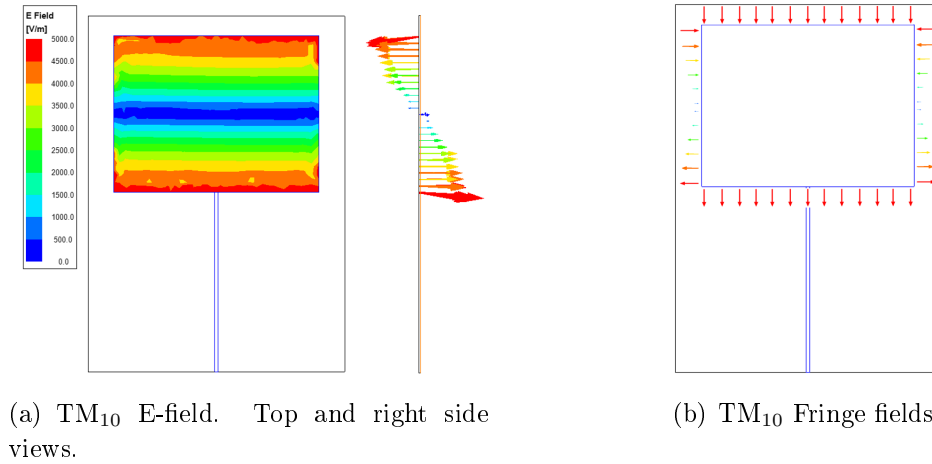
Figure 2.7: E field in a MSA.

According to the Huygens principle and field equivalence principle, each radiating slot can be modeled as a magnetic dipole with magnetic current density $\overrightarrow{M}_S = -2\widehat{n} \times \overrightarrow{E}_a$, being $\overrightarrow{E}_a$ the E-field in the aperture. Densities of both slots have the same magnitude and phase, so the radiated fields add in phase in the broadside direction (z in Figure 2.6).

The radiation pattern of a MSA usually is a broad fan beam pointing towards broadside direction of the patch (Figure 2.8). The beamwidths in both orthogonal planes are broad, the directivity is low and also the efficiency. The radiation pattern of a MSA can be varied: printed monopoles or printed Vivaldi antennas radiate towards endfire direction, with omnidirectional and pencil beam shapes, respectively.
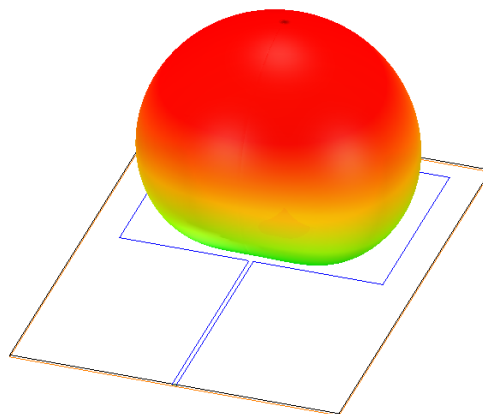


Figure 2.8: 3D directivity radiation pattern of a MSA at 485 MHz.

## 2.3.2   Bandwidth Enhancement Techniques in MSA

MSA present narrow bandwidths, around 1.5% for the prototype shown in Figure 2.6. This parameter can be enhanced up to 10% changing the feeding method (Table 2.2). In literature, different techniques had been studied to improve the bandwidth of MSA, as this is a critical operation parameter in many telecommunications systems, including radar, allowing a better resolution.

- **Employing a thick substrate with low dielectric constant: air.** Bandwidth is inversely related with the quality factor $Q$ of an antenna, which is influenced by the height or thickness of the substrate $h$ and the relative dielectric constant $\varepsilon_r$ (Equation 2.13). Air substrate has the minimum dielectric constant and it provides the advantage of having freedom in the thickness selection by only spacing the patch from the ground plane. In this way, the maximum achievable BW is around 15% with thickness equal to $0.15\lambda$ [107]. If the thickness is increased too much, the field would not cohere efficiently between the patch and the ground plane, causing a degradation in the radiation pattern. A BW up to 25% can be achieved by stacking one or more parasitic patches on top of the main one [108] (Figure 2.9).

$$BW \approx \frac{f}{Q} \approx \frac{4f^2h}{c\sqrt{\varepsilon_r}} \tag{2.13}$$
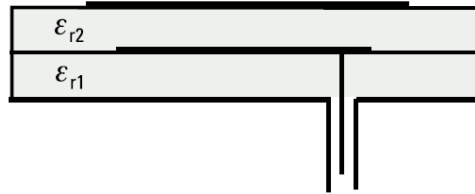


Figure 2.9: Scheme of an electromagnetically coupled stacked MSA, in which the bottom patch is fed and the top one is parasitic [109].

- **Antennas shorted or loaded with a resistor.** Planar Inverted-F Antennas (PIFA) are a well known exponent of this group (Figure 2.10(a)), being broadly employed in mobile phone industry due to its reduced size and multi-band possibilities [110]. In them, the patch is connected to the ground plane through a pin that reduces the resonance frequency of the rectangular patch. If the shorting pin is replaced by a resistor of low resistance (Figure 2.10(b)) the antenna bandwidth can be improved up to 9.3% at 700 MHz, reducing even the size of the PIFA [111].

- **Different patch shapes.** The fundamental patch shapes can be modified for enhancing the BW. An E-shape patch, made by cutting two slots from a rectangular one (Figure 2.11(a)), and employing air substrate can achieve a BW up to 30% at

(a) PIFA



(b) MSA loaded with resistor [111]
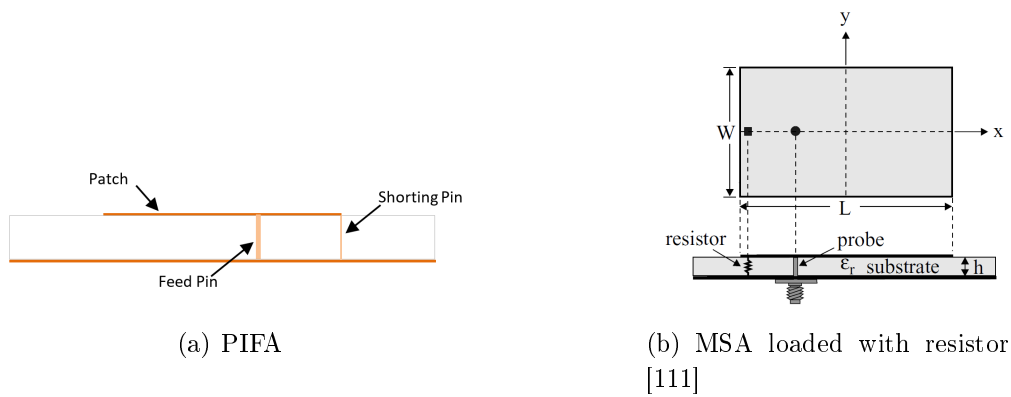
Figure 2.10: Scheme of shorted planar inverted-F antenna; Rectangular patch antenna loaded with resistor for compact and broadband operation.

frequencies in S-band [112]. The addition of a parasitic metallic ring around the patch will excite a second resonance frequency below the main one. The wide of the ring and the distance between it and the patch can be adjusted to double the original bandwidth [109]. Fractal patches are characterized by the repetition of a motif over two or more scale sizes, also known as a self-similar design (Figure 2.11(b)). They are usually designed through mathematical or optimization techniques, and provide BW up to 8% and multiband operation [113]. More recently, some antennas have been designed imitating nature motifs, as flowers or leafs, achieving wide BW. In [114], an antipodal vivaldi antenna inspired in nature fern is designed (Figure 2.11(c)). It achieves an ultrawide BW of 175%, operating between 1.3 and 20 GHz.



(a) E-patch



(b) Sierpinski triangle



(c) Nature fern inspired vivaldi antenna [114]
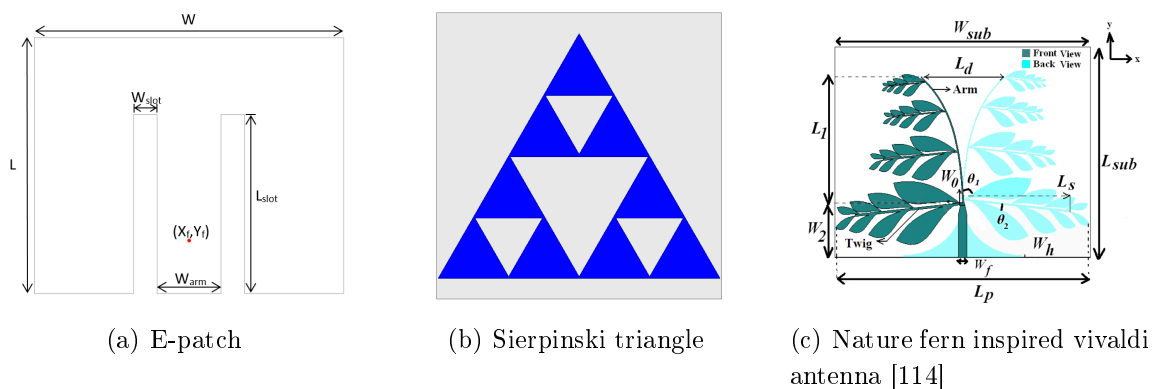
Figure 2.11: Different patch shapes that enhances the matching bandwidth of MSA.

# 2.4   Array Theory

An antenna array, or array antenna, is defined as *an antenna comprised of a number of single radiating elements, usually in a regular arrangement or geometry, and excited to obtain a prescribed radiation pattern* [99].

The electromagnetic field transmitted or received by an array depends on the radiation pattern of each radiating element and others parameters such as geometry of the group, spacing between elements and the excitation magnitude and phase of each element. These parameters allow the synthesis of a wide variety of radiation patterns (Figure 2.12) [115] [116].

Arrays are usually considered as space-time filters providing angular discrimination to transmitted or received signals. Signals that propagate along a given direction can be enhanced by a constructive combination or rejected by destructive interference in a particular time instant.
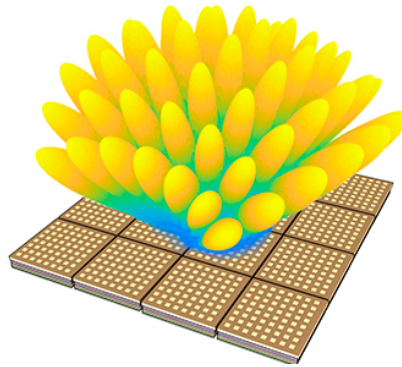


Figure 2.12: Array composed of patch antennas and radiation pattern formed by the superposition of several beams [117]

.

## 2.4.1   Array Parameters

A. **Single element** characteristics have a great importance in the design, because they will define primarily the array performance. Generally, all the elements of an array are identical, which is called homogeneous array, but there is no technical issues that avoid the possibility of employing different elements. However, the radiation pattern of each element could be different, even being identical elements, due to coupling effects between elements.

B. The **Group geometry** is defined by the number of elements N and the position
of each of them in the space. The geometry determines the directions in which the
main radiation beam could be steered. Possible geometries of an array are:

  (i) **Linear.** It is the simplest geometry to analyse. The elements are located in
the same axis (Figure 2.13(a)) and the steering can be made only in the plane
(azimuth or elevation) that contains the axis where the elements are placed in.

 (ii) **Planar.** The elements are located in a plane in different shapes, the most
common are rectangular (Figure 2.13(b)), circular or elliptical. The steering
can be made in both azimuth and elevation planes but it is limited by the
single radiation pattern and the element spacing, defining the scanning range
of the array.

(iii) **Three-dimensional (3D).** The elements are located along all the space fol-
lowing a classic polyhedron: cube, sphere, cylinder, octahedron,etc (Figure
2.13(c)); or an irregular geometry which is usually optimized through algo-
rithms. 3D arrays are usually employed to achieve conformal antennas that
can adjust to the surface of the objective system (Figure 2.13(d)). The de-
sign, analysis and manufacturing of 3D arrays is more complex, but they can
improve array performances and avoid scanning range limitations.



(a) Linear     (b) Rectangular     (c) Octahedron [118]



(d) Conformal [119]
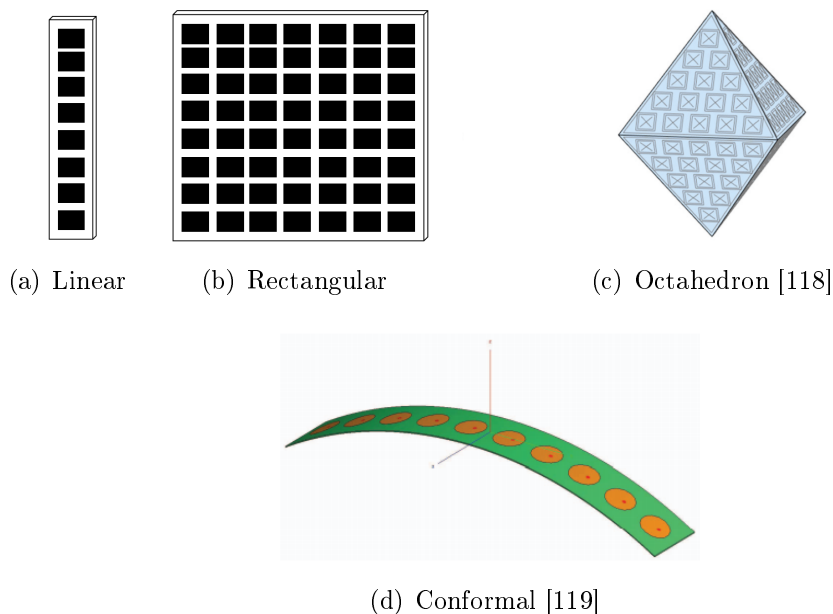
Figure 2.13: Different array geometries.

C. The **Element Spacing** is an important parameter because it has influence in the array radiation pattern response and determines the possible interferences between the elements of the array that affect to the pattern of each element and, therefore, to the total array pattern. The element spacing is defined as the distance between the middle points of two contiguous elements. An array that have all the element spacing the same is called *uniform array* and the one that has different spacing for each element is called *non-uniform*. As a general rule, an increase in inter-element distances will increase the directivity of the main beam, narrowing the beamwidth, because the total antenna aperture will also be increased. However, high inter-element spacing can cause the appearance of copies of the main beam in complementary angles, which are known as grating lobes and are an important source of ambiguities. Non-uniform arrays are usually designed following optimization processes to select the inter-element spacing distribution to maximize the performance of the array [120] [121] [122].

### 2.4.2 Array Factor

The Array Factor (AF) is the radiation pattern of an array antenna when each array element is considered to radiate isotropically [99]. It is a function that depends on the position of the elements and the amplitude and phase coefficients associated to each one (complex weights).

The response of an array is obtained as the vectorial addition of the E-fields generated by each one of the single elements (Equation 2.14).

$$\overrightarrow{\mathbf{E}_T}(\theta, \phi) = \overrightarrow{\mathbf{E}_1}(\theta, \phi) + \overrightarrow{\mathbf{E}_2}(\theta, \phi) + \cdots + \overrightarrow{\mathbf{E}_N}(\theta, \phi) \qquad n = 1, 2, ..., N \qquad (2.14)$$

The AF is an spatial function that describes the response of the array according to its characteristics but avoiding the specificities of the single elements, considering them as isotropic radiators. The AF can be considered a Fourier series and it is calculated following Equation 2.15 [123].

$$\mathbf{AF} = \sum_{i=1}^{N} w_i \cdot e^{jk\overrightarrow{\mathbf{r}_i}\widehat{\mathbf{r}}} \qquad (2.15)$$

Being:

- $w_i$ amplitude ($a_i$) and phase ($\beta_i$) coefficients associated to each one (the complex weights): $w_i = a_i \cdot e^{j\beta_i}$

- $\mathbf{r}_i$ the distance from each element in the group to the point where the array response is being evaluated

- $\widehat{\mathbf{r}}$ the unit vector indicating the direction where the array response is being evaluated

Considering an homogeneous array, the total electric field ($E_T$) is equal to the product of the field of a single element ($E_0$), at a selected reference point (origin), and the array factor calculated with respect to the same reference point (Equation 2.16). This is referred to as pattern multiplication for arrays of identical elements [100].

$$\overrightarrow{\mathbf{E}_T}(\theta, \phi) = \overrightarrow{\mathbf{E}_0}(\theta, \phi) \cdot \mathbf{AF} \tag{2.16}$$

## 2.4.3   Phased Arrays

Phase Arrays are groups of antennas that are fed coherently employing different phase or time-delay control at each element to steer the main beam to a given angle. Variable amplitude control is sometimes also provided for pattern shaping [124].

Phased arrays are sometimes used because they allow a precise control of the radiation pattern: reduction of side lobes or pattern shaping. However, the main reason of employing a phased array instead of a single antenna is its ability of producing directive beams that can be scanned electronically towards different angles.

Considering the simplest case of an N element Uniform Linear Array (ULA) with same amplitude for all elements (Figure 2.14), its AF is defined in Equation 2.17, being $N$ the number of elements, $k$ the wavenumber in the free space ($k = 2\pi/\lambda$), $d$ the ULA inter-element distance, $\theta$ the angle where the radiation is being evaluated and $\beta$ the phase distribution applied to the elements.

$$\mathbf{AF} = \sum_{n=1}^{N} e^{j(n-1)(kd\cos\theta + \beta_n)} \tag{2.17}$$
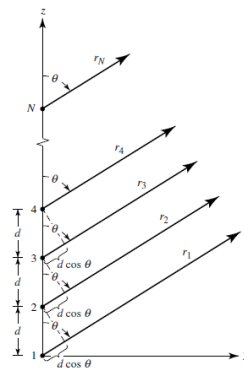


Figure 2.14: Far-field geometry of a uniform linear array of N elements [100].

The AF can be expresed in a compact and closed form more useful in practice (Equation 2.18). As well, a relative phase term is usually defined as $\Psi = kd\cos\theta + \beta$ to achieve a simpler expression.

$$\mathbf{AF} = \left[ \frac{\sin\left(\dfrac{N}{2}\Psi\right)}{\sin\left(\dfrac{1}{2}\Psi\right)} \right] \tag{2.18}$$

The electronic scanning of the maximum radiation of an array is performed applying a progressive phase difference between the elements. The phase excitation $\beta$ between the elements depends on the spacing between them $\mathbf{d} = [0, d, 2d, \ldots, (N-1)d]$, the desired angle of steering $\theta_0$ from the broadside and wavenumber evaluated at the operation frequency ($k$) (Equation 2.19 [100]).

$$\beta = -kd\sin\theta_0 \tag{2.19}$$

The radiation pattern cut of a linear array of N-elements, in its corresponding steering plane, can be calculated knowing the radiation pattern of each element $E_n$, the distance of each element to the reference one ($d_n$ from vector $\mathbf{d}$) and the amplitude and phase excitation of each element $a_n$ and $\beta_n$ [125]. If we consider a linear array located in Y axis, its radiation pattern for all $\theta \in [-180°, 180°]$ in plane $\phi = 90°$ is:

$$E_T\left(\theta, \phi = 90°\right) = \sum_{n=1}^{N} a_n \cdot E_n\left(\theta_{\phi=90°}\right) \cdot e^{j[k_0 d_n \sin(\theta) + \beta_n]} \tag{2.20}$$

### 2.4.3.1 Beamforming

Beamforming comprises the set of signal processing techniques employed with sensor arrays to achieve directional signal transmission or reception. It is a type of spatial filtering based on the combination of the signals received by the different elements of the array, in the way that they interfere constructively or destructively to accept the signals coming from some directions (angles) and reject those coming from other directions. A beamformer is the set formed by a signal processing block and an array of sensors.

The implementation of a digital beamformer lies in the digitalization of the signals acquired by each single elements $\mathbf{x}$ and the processing applying a set of complex weights $\mathbf{w}$ to the elements to modify the total array response (Figure 2.15). The output of the beamformer $\mathbf{y}$, employing matrix nomenclature, is $\mathbf{y} = \mathbf{w}^H \mathbf{x}$.

Beamforming is based on the difference in arrival time between the samples of the same signal acquired by the different elements of the array. In the case of narrowband signals, this temporal delay is equivalent to a phase difference between the samples and, therefore, the weights vector adjusts the phases to achieve the addition in phase of all the signals that come from the interest direction. However, in broadband signals the signal delay cannot be defined by a unique value at the central frequency of the bandwidth, they have different phase in each frequency component. Narrowband signals, in array processing, must fulfil that the Time-BandWidth Product ($TPBW$) is much less than
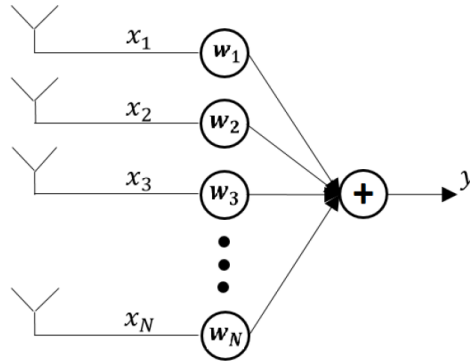
Figure 2.15: Scheme of a digital beamformer: different complex weight are applied to each input before adding them to generate the output array response.

1 [126]. Time is defined as the maximum travel time $\Delta T_{max}$ between any two elements in the array. In a linear array it would be the travel time between the two elements at the ends of the array for a signal arriving from the axis normal to the array direction (Equation 2.21).

$$TPBW = B_s \cdot \Delta T_{max} = \frac{B_s \cdot d_{max}}{c} \ll 1 \tag{2.21}$$

Being $d_{max}$ the maximum physical distance between two elements in the array.

The response of the array is modified as a function of the selected coefficients. Beamformers can be classified in:

- **Data-independent beamformers** do not require information about the signals, the noise or the interferences present in the environment. They are employed in stable environments, when the direction of arrival of the signal is known previously or when an angular scanning of the coverage area is being made, as in radar systems.

- **Optimal beamformers** are designed having into account the statistics properties of the signals to achieve the optimum response. The weight vector is determined in such way that it minimizes a cost function. They are usually employed in changing environments where the objective is to maximize the Signal-to-Interference Ratio (SIR) or when the direction of arrival is unknown. The most commonly used optimally beamforming techniques are the Minimum Mean Square Error (MMSE), Maximum Signal-to-Noise Ratio (MSNR), and Minimum noise Variance (MV) [100]. Determining the second order statistics (variance and covariance) of the signal is usually a difficult task and they can vary with the time.

- **Adaptive Beamformers** can adapt to changes in the environment determining the weights vector in real-time for pattern optimization. These techniques are more frequently used in reception although it is possible to adapt transmit pattern subject

to some noise distribution or as in the case of *retrodirective beams* for automatically transmitting in the direction of a received signal or pilot tone [100].

**2.4.3.2   Grating Lobes**

Grating lobes are the ones that appear in the radiation pattern in supplementary angles
to the steering ones. They are due to the periodicity of the AF so their level is higher
than side lobes, so they can limit seriously the performance of the antenna. It should be
taken into account that the radiation pattern of the single element usually decreases the
level of the grating lobes below the level of the main one. The appearance of grating lobes
depends on the separation between elements $d$ and the steering angle $\theta_0$.

A general way of checking the appearance of grating lobes in a linear array of N
elements, is representing the AF (Equation 2.18 being $\beta$ defined in Equation2.19) as a
function of $Q \cdot d$ (Figure 2.16), being $Q = k \left( \cos \theta - \cos \theta_0 \right) / 2$. If a replica of the main lobe
is found within the visible margin, grating lobes will appear in the radiation pattern of
the array. The visible margin is the range of values of $Q \cdot d$ that can be achieved according
to the domain of cosine function.
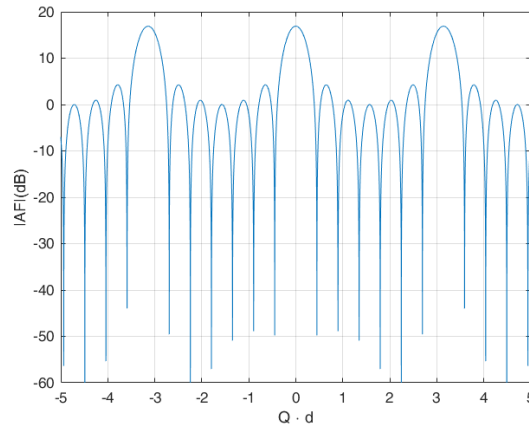


Figure 2.16: Array function of a linear array of $N = 7$ elements as a function of $Q \cdot d$.

**2.4.3.3   Amplitude Taper**

Amplitude taper refers to feeding each element of an array with different amplitude.
Typical amplitude distributions are triangular, binomial, Chebyshev or Taylor polynomial.

This technique is employed to decrease the level of side lobes at the expense of broad-
ening the main beam. In [125], a comparison of the radiation pattern of a 8-element linear
array, with inter element distance $d = \lambda/2$ for avoiding grating lobes, feeds with uniform,
triangular and binomial amplitude tapers is studied, showing the greatest decrease in SLL
for the binomial taper, at the same time that the main beam is the widest of the three
cases (Figure 2.17).
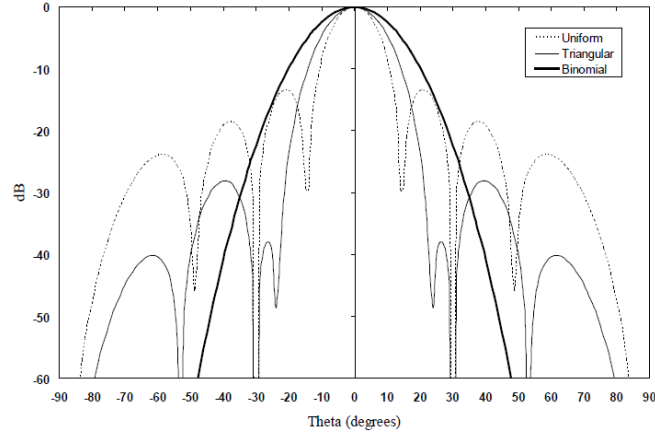
Figure 2.17: Radiation pattern of a 8-element linear array with $d = \lambda/2$ for a uniform, a triangular and a binomial amplitude taper [125].

## 2.5   Reflectarray Antennas

Reflectarray antennas combine the reflector antenna concept with array theory for collimating the radiation towards a defined direction of the space. They are composed of an illuminating feed antenna and a reflecting surface consisting of hundreds or thousands of elements, usually microstrip patches, each of them with a given phase that allows to reflect and collimate the electromagnetic field created by the feed in a given direction [127].

These antennas combine some advantages of reflector ones, as high directivity, with the versatility of arrays in the ability of shaping the radiation pattern, and thanks to the recent progress in printed microstrip technology, they allow an easy and low cost manufacturing process.

In the last years, reflectarray antennas have attracted the interest of scientific community for different applications, such as satellite ground terminal [128], on-board satellite broadcast [129], radar and Synthetic Aperture Radar (SAR) [84] [130], and 5G communications [131].

The design of a reflectarray antenna with a defined radiation pattern is a complex process in which many items should be taken into account: feed characteristics, geometrical parameters, required phase distribution and single elements. It is usually carried out employing optimization techniques.

### 2.5.1   Reflectarray Parameters

A. The **Feed** of a reflectarray is usually a horn antenna which is placed with its phase centre at the focal point of the group $(x_f, y_f, z_f)$.

The aperture illumination is defined as the field produced by the feed in the aperture, that is, in the reflector surface. Therefore, its distribution determines the field in

each element of the reflectarray which, together with the reflection characteristics of each element, defines the radiation characteristics. The aperture illumination depends on the radiation pattern of the feed and the geometry subtended by the feed and the reflector.

In order to achieve a good aperture illumination, the pattern of the feed must fit to the shape of the aperture: if square or circular shape reflector is employed a balanced feed should be employed but if rectangular or elliptical shape reflector is selected a non balanced feed will improve the performance. A balanced feed is defined as the one that has symmetric pattern for both E and H planes, while a non-balanced feed has asymmetric patterns.

To simplify the design process of a reflectarray, it is usual to employ a model that approximates the real pattern of a feed. The most common one is the $\cos^q()$ pattern [132] (Figure 2.18). In case of non-balanced feed $\cos^q_E()$ and $\cos^q_H()$ represent the pattern for E and H planes respectively.
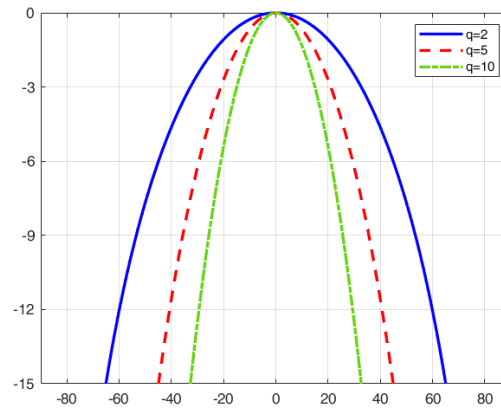


Figure 2.18: Radiation pattern of the $\cos^q()$ feed pattern model.

B. **Geometry.** The main geometrical parameters of a reflectarray are shown in Figure 2.19. The main beam is tilted from the normal of the reflectarray surface with angles $\phi_b$ and $\theta_b$. Each element is located with its centre in position $(x_i, y_i)$. The distance between the feed and the centre of the reflector, called focal distance, is defined by $F$, and the distance between the feed and each element by $d_i$. If the feed is displaced along X axis a distance $x_f$, it should be rotated an angle $\theta_f$ with respect the Z axis (the normal of the reflectarray), in order to cover both edges of the aperture with similar radiation intensity.

The ratio between the focal distance and the diameter of the aperture $F/D$ has direct influence in the aperture efficiency, that is, in the reflectarray efficiency. The aperture efficiency is defined as the product of illumination[1] $\eta_I$ (Equation 2.22) and

---

[1]The illumination efficiency measures the uniformity of the E-field across the aperture.
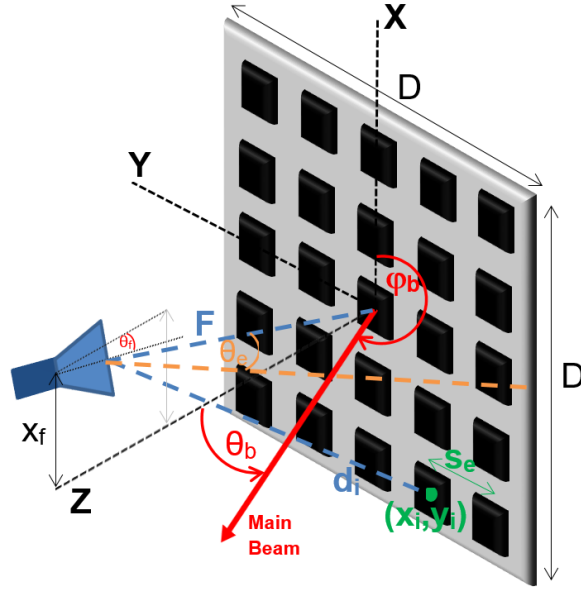
Figure 2.19: Scheme of main geometrical parameters of a reflectarray.

spillover[2] $\eta_s$ (Equation 2.23) efficiencies (Equation 2.24) [133]. As it can be observed, both efficiencies can be calculated, for a center-fed reflectarray, as a function of the exponent of the feed pattern function $q$ and the half of the subtended angle from the feed to the reflectarray aperture $\theta_e$, which is directly related to $f/D$: $\theta_e = atan\,(D/2f)$.

$$\eta_I = \frac{\left(\dfrac{1+\cos^{q+1}\theta_e}{q+1} + \dfrac{1-\cos^q\theta_e}{q}\right)^2}{2\tan^2\theta_e \cdot \dfrac{1-\cos^{2q+1}\theta_e}{2q+1}} \tag{2.22}$$

$$\eta_s = 1 - \cos^{2q+1}\theta_e \tag{2.23}$$

$$\eta_a = \eta_I \cdot \eta_s \tag{2.24}$$

Element spacing is another important parameter to have in mind when designing the geometry of a reflectarray. The minimum element spacing $s_e$ to avoid grating lobe type radiation becomes smaller for the element located toward the edge and, since uniform spacing is usually employed for ease of design, this minimum spacing required at edge elements is set for all elements. The minimum element spacing (Equation 2.25) depends on the operation frequency and the larger angle $\theta$ of the

---

[2]The spillover efficiency measures the amount of radiation from the feed that the aperture reflects, considering that part of the feed radiation loses out of the surface of the aperture.

next two: the main beam tilt from the broadside direction or the maximum incident angle from the feed to one element.

$$s_e \leq \frac{\lambda}{1 + \sin\theta} \tag{2.25}$$

C. **Phase Distribution.** The working principle in reflectarray antennas is defined by array theory: each element of the reflection surface must introduce a certain phase-shift in order to collimate a beam in a given direction. The phase distribution that must be fulfilled by each element $\phi_r(x_i, y_i)$ to produce a beam in the direction $(\theta_b, \varphi_b)$, is obtained considering the phase of the incident field at each element due to propagation and the progressive phase required at each element (Equation 2.26).

$$\phi_r(x_i, y_i) = k_0(d_i - (x_i cos\varphi_b + y_i sin\varphi_b)sin\theta_b) \tag{2.26}$$

Being $k_0$ the propagation constant in vacuum, $d_i$ the distance from the phase center of the feed to element $i$ and $(x_i, y_i)$ the centre position coordinates of the element $i$, as it is sketched in Figure 2.19.

D. **Single Elements.** The element selection is a key step in reflectarray design, because it determines the reflection efficiency and the bandwidth of the antenna. The patch shape of the single element, as well as other parameters as its rotation or size, determine the phase of its reflection coefficient. The change in phase is usually characterized as a function of a change in dimensions or rotation, which is called the *"S" curve* of the element (Figure 2.20). This curve must cover up a phase-shift of $\pm 180°$ with a smooth slope [133]. The *"S" curve* is employed to determine the size or rotation that each of the elements of the reflectarray aperture must have to fulfils the phase distribution.

In order to achieve the full $\pm 180°$ phase-shift, elements of a single type or a combination of different ones can be employed.
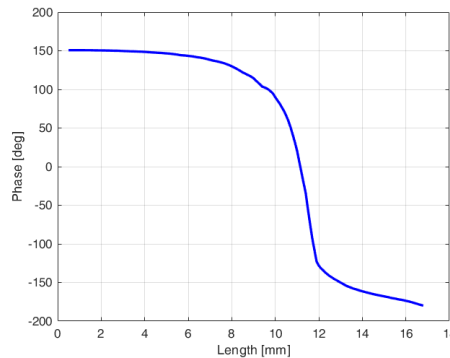


Figure 2.20: *"S" curve* of a rectangular element as a function of its length at 11 GHz.

E. The **Radiation Pattern** of a reflectarray can be estimated through array summation from the feed pattern, the geometry and an accurate characterization of the reflection coefficients of the elements. The calculus of the RP could be more useful in UV coordinates, specially if some optimization techniques are being applied to achieve a required radiation distribution, because they are usually based in the comparison of the pattern with some mask. In this way, the reflectarray radiation pattern can be estimated following Equation 2.27.

$$E_r(u,v) = \sum_{m=1}^{M} \sum_{n=1}^{N} E_{inc_{m,n}} |\Gamma_{m,n}| e^{j\phi_{m,n}} e^{jk_0(ux_{m,n}+vy_{m,n})} \tag{2.27}$$

Being:

- $M \times N$ the total number of elements. Their positions in the aperture are represented by $x_{m,n}$ and $y_{m,n}$.

- $E_{inc_{m,n}}$ the incident field from the feed in each element.

- $\Gamma_{m,n} = |\Gamma_{m,n}| exp(j\phi_{m,n})$ is the reflection coefficient at the patch located at $(x_m, y_m)$.

Some simplifications can be applied to the estimation, as for example a feed pattern model or the assumption that every element has the same reflection coefficient modulus, but they will drive to inaccurate results.

The estimation above does not have into account the coupling effects between elements, so electromagnetic simulation techniques are often employed to calculate the radiation pattern of a reflectarray.

# Chapter 3

# IDEPAR Technological Demonstrator

IDEPAR is a technological demonstrator developed at the Signal Theory and Communications Department, of University of Alcalá. It has been built up and updated under three research projects funded by the Spanish Ministry of Economy and Competitiveness: IDEPAR (Research on Improved Detection techniques for Passive Radars; reference TEC2012-38701), MASTERSAT (MultichAnnel paSsive radar receiver exploiting TERrestrial and SATellite Illuminators; reference TEC2015-71148-R) and and KRIPTON (*A Knowledge based appRoach to passIve radar detection using wideband sPace adapTive prOcessiNg*; RTI2018-101979-B-I00) [33] [134].

The initial deign requirements of IDEPAR demonstrator were:

- Use of COTS components to reduce the whole system cost, and to allow the easy reconfiguration of the system to face the future requirements changes.

- Use of standard interfaces and developing tools to increase the system interoperability.

- Modular system that allows the scalability and simplify the maintenance.

- Off-line data processing to allow the quick development and assessment of new processing schemes without the requirement of new acquisition campaigns. This architecture is making possible the generation of a valuable database of row data.

## 3.1 Review of previous IDEPAR versions

IDEPAR demonstrator has been evolving from an initial version, to improve its performance and tackle new challenges defined by the progress in passive radar technologies and in security and defence applications, in general. During this progress three different versions of the system can be highlighted. This thesis is closely related to the development of the third version of IDEPAR. The main characteristics of the two previous versions are briefly described:

- **IDEPAR v1**: the first version of IDEPAR demonstrator was designed with a configuration of two acquisition channels, one for the reference signal and another for the surveillance one (Figure3.1(a)) [33]. Commercial antennas *Televés DAT HD 75 BOSS* were employed for both channels. This Yagi type antenna is characterised by high gain in the DVB-T band ($\sim$ 17 dBi), high front-to-back ratio due to the rear reflector ($\sim$ 30 dB), narrow beamwidth (30°) in both planes and linear polarization (Figure 3.1(b)). The acquisition chain was completed with a RF cavity band pass filter to select the three DVB-T channels at the high part of the frequency band allocated before the first freqeuncy release (850 MHz), Low Noise Amplifiers (LNA) to improve the targets' echoes level and Software Defined Radio (SDR) acquisition boards (*USRP-N210* from *Ettus*). The USRP provided a maximum continuous acquisition bandwidth of 25 MHz, enough for three consecutive DVB-T channels. An external synchronisation unit was used to provide 10 MHz clock reference and a Pulse Per Second (PPS) signal to synchronise the acquisition systems. All the acquisition system was controlled by a high performance work station in which the acquired signals were stored and processed off-line.



(a) Elements scheme                          (b) Antenna RP at 750 MHz
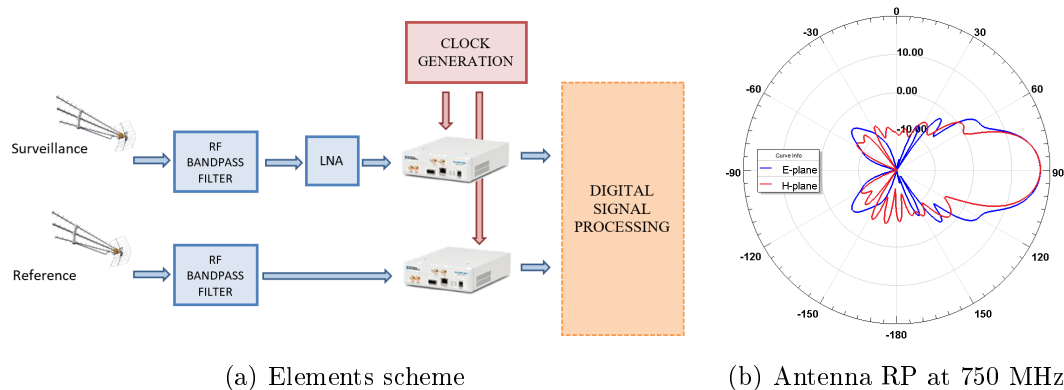
Figure 3.1: Functional block diagram of IDEPAR v1 demonstrator and Televes Dat HD 75 Boss antennas radiation patterns.

- **IDEPAR v2**: the first version of IDEPAR did not provide azimuth discrimination, and the detection and tracking stages were limited to the range-Doppler space. The second version of IDEPAR solved this problem by increasing the number of acquisition channels in the surveillance receiver chain to allow the implementation of digital array processing (Figure 3.2(a)) [135]. 6 N-210 were available so an array of five commercial antennas was considered. The narrow beamwidth and physical dimensions of Televés DAT HD 75 BOSS antenna discouraged its use in the array configuration due to the small angular coverage and the appearance of grating lobes in the array radiation pattern. Due to those drawbacks, a new commercial antenna, the *Televés 4G Nova*, was selected as the single radiating element of the linear array. The Televes 4G-Nova is a log periodic printed antenna built on an FR4 substrate

(Figure 3.2(b)). It was characterized in the anechoic chamber of High Technology and Homologation Centre, CATECHOM, of the University of Alcalá, showing that it is matched within DVB-T frequency band at frequencies from 711 MHz to 787 MHz (Figure 3.2(c)). This antenna provides a wide angular coverage (60° in azimuth plane) that increases the surveillance area while keeping a medium gain (6.8 dBi at 740 MHz) with linear polarization. The antenna size in the dimension parallel to the linear array axis is 315 mm, for capturing the horizontally polarized DVB-T signal, but it can be reduced to 287 mm by removing the radome and to 210 mm detaching the back reflector. It has been proved through simulation that the reflector does not affect at the radiation pattern at DVB-T frequencies. The size without radome nor reflector reduces the ambiguities due to the presence of grating lobes in the array pattern, allowing an steering margin free of grating lobes of ±65° which is greater that the single element beamwidth that limits the steering. A 5-element ULA with minimum inter-element spacing achieves a maximum gain of 12.3 dBi with SLL of 8 dB in the worst case.



(a) *IDEPAR v2*     (b) *Televés 4G Nova*     (c) Measured $|s_{11}|$
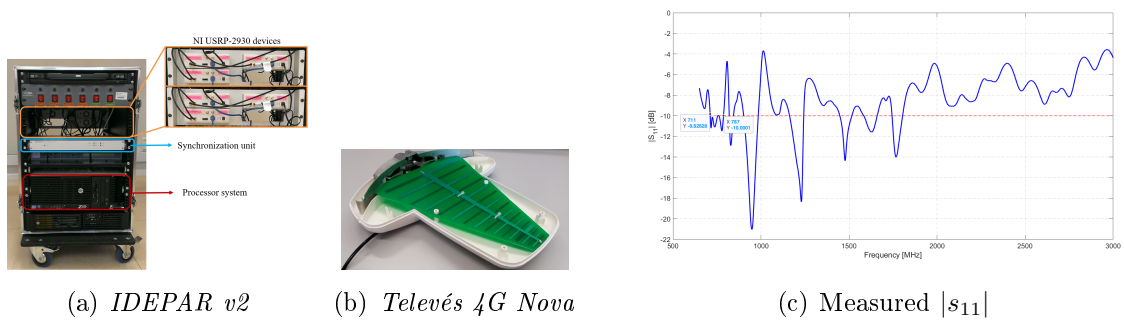
Figure 3.2: Second version of IDEPAR demonstrator, antenna Televes 4G Nova and its measured reflection coefficient.



(a) Antenna radiation pattern     (b) ULA with orthogonal beams
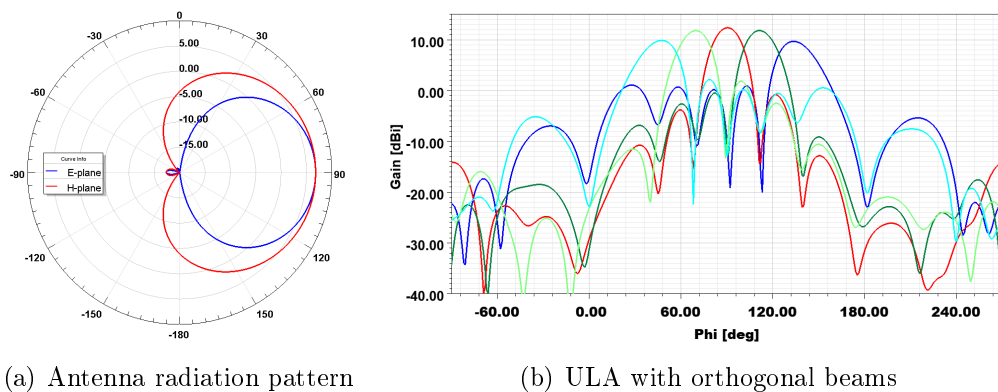
Figure 3.3: Antenna Televes 4G Nova radiation pattern for single element and ULA array of 5 elements with minimum inter-element distance of 210 mm, at 750 MHz.

## 3.2   3$^{rd}$ version of IDEPAR demonstrator

During last years, the frequency distribution of DVB-T channels has been changed to release the 800 MHz band for LTE communication transmission. The channel relocation process gave rise to a disperse distribution of the DVB-T channels, maintaining the variation throughout the whole territory with a small number of channel sets composed of two or three consecutive channels. In this new DVB-T distribution, wider acquisition bandwidths are required to keep the system resolutions with non-consecutive DVB-T channels and to increase system robustness with respect to channel allocation variation in different emplacements. Additionally, the acquisition system of IDEPAR v2 also presents several phase maladjustments due to the independent local oscillators of the RF stage at the Ettus N-210, which caused that the surveillance channel array must be calibrated in each acquisition for beamforming generation.

This 3$^{rd}$ update also incorporated the possibility of acquiring satellite signals, focusing in DVB-S ones. The acquisition bandwidth of the Ettus N-210 (25 MHz) lead to aliasing in many cases (for example in the acquisition of DVB-S channels transmitted by Hispasat 30-W, which bandwidths lie in the range from 27.5 MHz to 35 MHz).

Taking into account the previous ideas, the PR acquisition system was redesigned to improve the demonstrator capabilities. The main change in the acquisition chain was the substitution of the Ettus N-210 by two *NI USRP X310* composed each one of two *TwinRX*. These boards allow the coherent acquisition of up to 8 channels with an instantaneous bandwidth of 100 MHz. The LO sharing between RF front ends improves the acquisition coherency and makes digital array processing easier. The higher acquisition bandwidth allows the use of disperse DVB-T channels to keep the system resolution achieved before the channel relocation process, and the acquisition of more than one DVB-S channels, improving resolution also with these IoOs.

The new acquisition systems encouraged the design of new antenna systems for the surveillance channel of the demonstrator. If DVB-T is employed as IoO, the design of a single element, fulfilling appropriate requirements for radar, will allow to design the best array geometry for improving system capabilities. In DVB-S case, first commercial solutions based on parabolic dish antennas were explored, without achieving the expected detection results, due to the critically small sector coverages associated to the very narrow beams.

The main objectives of this thesis are the design of different antenna systems for the updating of the surveillance channel of this version of the demonstrator with the aim of improving detection, positioning and tracking performances.

# 3.3 Processing Architecture

The main processing stages such as filtering, clutter rejection, beamforming, CAF, detection and tracking are implemented offline after saving to disk the raw data provided by the acquisition chains (Figure 3.4). This is the selected approach for research activities because it allows the generation of databases of raw data that correctly labelled can be used for the design and validation of new signal processing solutions. Alternative data management approaches are being explored for achieving NRT (Near Real -Time) operation.

ECA adaptive filtering is implemented for DPI and main zero-Doppler sources suppression in the surveillance channel. After the pre-processing stage, the CAF is calculated using a direct method based on Fast Fourier Transforms (FFTs).

As it is observed in Figure 3.4, different processing stages are applied depending on the demonstrator's version: the top branch for the $1^{s}t$ version (one surveillance antenna), and the bottom branch for $2^{n}d$ and $3^{r}d$ versions (surveillance array). This thesis employs the $3^{r}d$ version so the branch for array processing is considered.

Digital beamforming techniques are applied in the RDM domain, to take advantage of the coherent integration gain. A two stages approach is applied [135]: the first one generates up to N orthogonal beams, by means of digital beamforming with maximum directivity weights, employed for detection purposes; the second one estimates Direction of Arrival (DoA) of the detected targets through a traditional beam sweeping within a margin of angles inside the single element HPBW. The array processing techniques took advance of the properties of the Non-Linear Array based on commercial components designed as part of this PhD Thesis and that is described in Chapter 5.

The detection stage implements CA-CFAR techniques that assume an uncorrelated Gaussian clutter. Different strategies for the reference cell selection are adapted to the specific conditions of the radar scenario: 1D reference vectors in Range and Doppler, as well as 2D approach combining CA-CFAR detectors in both dimensions and 2D windowing techniques, and 3D techniques in (range, Doppler, azimuth space).

The detector output is analysed by the tracking stage to group together the detections from the same target, and estimate its location and trajectory. Bistatic tracking systems based on Kalman filtering are employed for operation in the range-Doppler plane. Tracking schemes based on the Extended and the Unscented Kalman filters are employed to perform target location in Cartesian coordinates taking advantages of the angle information provided by DoA estimation stage.
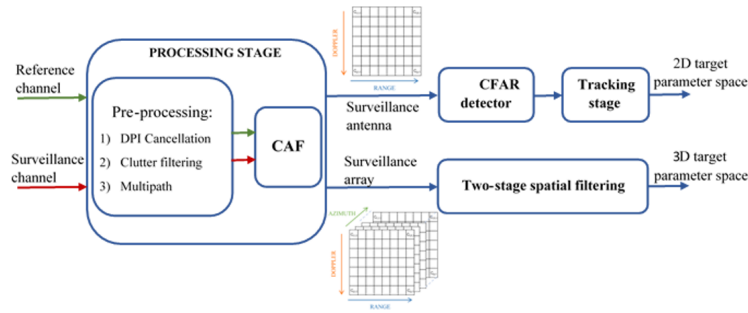
Figure 3.4: IDEPAR v3 processing scheme showing the two possible branches for single element or array processing.

## 3.4 Radar scenarios

The following radar scenarios were used for database generation and IDEPAR updates validation at hardware and software level.

They were selected considering detection applications of interest according to the study of technological and security and defence tendencies, and the limitations defined by access restrictions.

### 3.4.1 Semi urban scenarios

The external campus of the University of Alcalá (EC-UAH) is usually employed for different trials with IDEPAR demonstrator due to the easy and fast deployment in it. It is considered a semi-urban scenario as it contains medium height buildings. Three different emplacements are used for locating the PR depending on what IoO is being exploited: terrestrial or satellite.

#### 3.4.1.1 DVB-T scenario: the rooftop of Superior Polytechnic School

The rooftop of Superior Polytechnic School is the emplacement selected for trials employing DVB-T as opportunity signal. The PR system is deployed at 15 meters from the ground level to mitigate the ground effects and ensure the correct reception of both, the reference and the surveillance signals.

The main transmitter providing DVB-T service in this area is *Torrespaña*. It is employed as IoO because of its radiation characteristics: it transmits an Equivalent Radiated Power (ERP) of 20 kW with omnidirectional pattern. Other potential DVB-T IoOs are *El Viso* and *Algete*. Torrespaña is located at 28.7 km from the PR with an altitude of around 850 m relative to sea level (650 m+200 m terrain altitude plus antennas height), which provides direct Line of Sight (LoS).

The Area of Interest (AoI) or surveillance area is located outside the campus at the North of the PR (Figure 3.5). This scenario is usually employed for ground targets monitoring, as it covers two main roads: R2 Highway, that is located at around 2 km

(a) Scenario top view

(b) View from the PR location
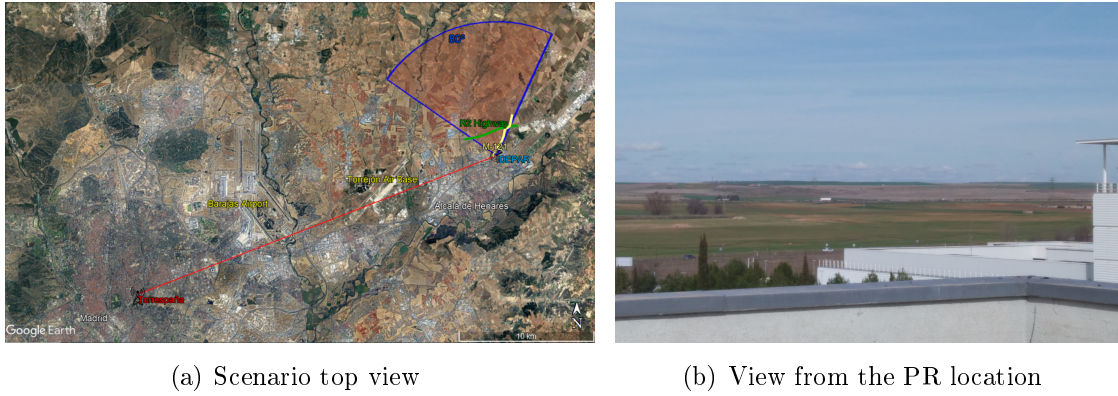
Figure 3.5: Superior Polytechnic School radar scenario with Torrespaña as IoO. AoI for desired 80° antenna covering R2 highway (green) and Meco road (yellow). IMMPA building is appreciated at the right of surveillance area in the image from the PR location.



(a) Scenario sketch

(b) Incidence angle
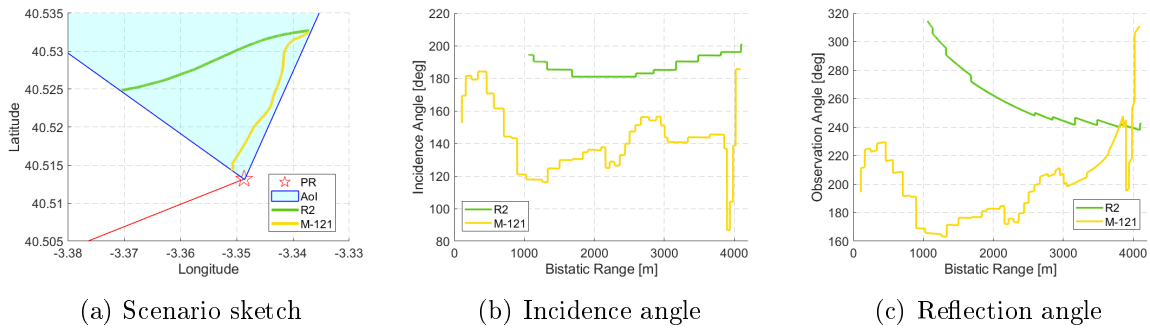
(c) Reflection angle

Figure 3.6: Superior Polytechnic School scenario sketch and the estimated incidence and reflection angles for targets moving away from the PR.

away from the PR receiver, and M-121 (Meco road), that is located at distances ranging from 300 m to more than 1 km away from the PR. Further, at distances further than 4 km away from the PR, the M-116 also crosses the AoI. Occasionally, some aeroplanes fly over the AoI in their approaching movements to a close Airport.

The estimation of the incidence and reflection angles of the targets moving along both roads allows a precise characterization of the power reflected from them through the bistatic radar cross section. Figure 3.6 shows the incidence and reflection angles in terrestrial targets moving away from the PR along both roads. It is assumed that the angle 0° is in the centre of the front of the car and that it is aligned with the road director vector at each point. For approaching trajectories the angles will be the equivalent to substract 180° to these ones.

Figure 3.7: DVB-S scenarios in the external campus of the University of Alcalá. PR-L1 represents the PR deployed next to Nursing School while PR-L2 is the location for monitoring traffic along M-121.

### 3.4.1.2 DVB-S scenarios: vicinity of Nursing School and M-121

For employing DVB-S as opportunity signal, IDEPAR demonstrator is usually deployed at street level for ground target detection. The two most common locations are next to the Nursing School and in the vicinity of M-121 road.

The surveillance area of the deployment next to Nursing School covers a straight street around 350 m long, surrounded by medium-height buildings, some trees and a metallic fence, which surrounds the sports facilities, extending from the half to the end of the street.

In the case that IDEPAR demonstrator is deployed in the vicinity of M-121, the objective is to detect the terrestrial targets moving along that road. In this case, the scenario is mainly surrounded by crops. This road has direct LoS from PR till it has a right turn and a little descent from where the targets hide behind a building and the trees surrounding this, at approximately 600 m away from the receiver.

Both scenarios are shown in Figure 3.7 as well as the view of each surveillance area from the PR location. The area covered by an antenna with an azimuth beamwidth of 10° has been marked in both scenarios, checking that the main AoI (road) is contained within that beamwidth.

The satellite *Hispasat 1E* (30W-5) was chosen as IoO for trials in these scenarios because it transmits more power than others illuminating this area, which translates into higher coverages: an EIRP of 54 dBW is transmitted from *Hispasat 1E* to the area covering Spain while *Astra* satellites (1KR, 1L, 1M and 1N) transmit an EIRP of 50 dBW [136] [137]. *Hispasat 1E* is a geostationary satellite located at at an altitude of

(a) Nursing School deployment      (b) M-121 deployment
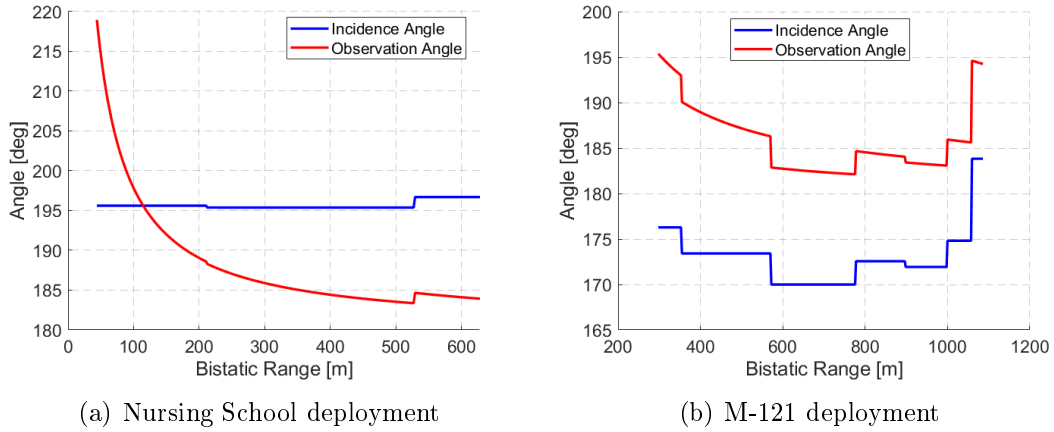
Figure 3.8: Estimated incidence and reflection angles for targets moving away from the PR in the described DVB-S scenarios in the external campus.

35786 km over Latitude $-0.02°$N and Longitude $30.02°$W, so it is seen in this area at an azimuth angle of $217.7°$N and an elevation angle of $35.75°$ over the horizontal plane.

The estimated incidence and reflection angles for targets moving away from PR along the roads of both scenarios are shown in Figure 3.8. For approaching trajectories the angles will be the equivalent to substract $180°$ to these ones.

### 3.4.2 Maritime Scenario

Trials with IDEPAR demonstrator in different scenarios allow to check its performance and find possible problems as well as it is an important source of incoming research lines to improve it. In the particular case of a maritime scenario, the sea clutter is expected to be a challenging threat for passive radar operation. To deal with this interesting issues IDEPAR was deployed at the base of the *Undécima Escuadrilla de Aeronaves de la Armada* ($11^{th}$ Aircraft Squadron of the Spanish Navy) located in the Torregorda Test Centre, in Cádiz (Spain). This military border coastal scenario was selected to study the feasibility of deploying a PR sensor network for maritime surveillance (Figure 3.9).

The main DVB-T transmitter for this area, located close to Jérez de la Frontera, was selected as IoO. It is located at 21.2 km far from the PR and it provides DVB-T broadcasting services to the whole AoI with a transmission power of aproximately 5 kW.

The AoI is set in such a way that it covers from the coastal border, including the area where the ships enter to the port at around10 km far away from the PR, and extends to offshore. The Rota Naval Base which include a runway, is within the AoI, so some aeroplanes could flight over the surveillance area.

In the scenario, inside the illumination area of the transmitter, there are some wind farms that should be taken into account because huge metallic structures such as wind turbines are expected to be detected by the passive radar.

Figure 3.9: Sketch of the maritime scenario in Cádiz.

### 3.4.3   Rural Scenarios

IDEPAR demonstrator was deployed at two rural scenarios to study drone detection and tracking capabilites.

A. **Rural scenario 1** is located at a region where the DVB-T broadcasting is mainly provided by a transmitter, that is located 34.1 km far from the PR location and transmits an EIRP of approximately 8 kW. An overall view of the radar scenario, with the location of the PR and the IoO, and a detailed view of the radar scenario are depicted in Figure 3.10(a).

   The Northwest area of the PR location was selected as the drone's flight area for the trials campaign, so the scenario can be considered rural. Due to the relative position of the transmitter and the flight area, the aerodrome control tower adjacent roof was selected for passive radar deployment. This configuration generates a favourable bistatic geometry and minimizes the direct path interference in the surveillance channel. In the same way, the altitude of the selected site reduced the detrimental effects of the terrain relief and obstacles (buildings and forest) for the acquisition of the reference signal from the IoO, as well as the target echoes in the surveillance channel.

B. **Rural scenario 2** was also employed for testing IDEPAR demonstrator capabilities for detecting and tracking small UAVs. The selected IoO is a local booster, that retransmits Torrespaña DVB-T channels, located at 260 m from the PR. The surveillance area in which cooperative drones will flight is located at the north of the passive radar location (Figure 3.11)

(a) Scenario top view



(b) AoI view from PR location

Figure 3.10: Rural scenario 1 and view of drones' flight area.



Figure 3.11: Sketch of the rural scenario in a residential area in Hontoba.

# Part III

# Research and Results

# Chapter 4

# Target electromagnetic modelling in bistatic scenarios

The objective of this PhD thesis is the design of different antennas system for improving the performance of IDEPAR demonstrator, described in Chapter 3, employing different IoOs and located in different scenarios. The study of those scenarios presented in Chapter 3, as well as the electromagnetic characterization of the usual targets moving around them, are the starting point for defining antenna requirements and to tackle the evaluation of possible solutions.

This chapter is divided in two parts: the first one studies different targets and their Radar Cross Section (RCS), that measures targets electromagnetic reflectivity and therefore has direct implication in the radar coverage and presents a coverage estimation method making use of the estimated RCS; in the second part different targets electromagnetic modelling approaches are proposed according to radar system resolution, to study features and their potential use for target classification at different levels: through the relation between RCS and SIR along a trajectory; through micro-doppler signature typical of some specific and really concerning targets nowadays, as it is the case of Unmanned Aerial Vehicles (UAVs); and by generating simulated bistatic ISAR images from the complex RCS of targets .

## 4.1   Bistatic Radar Cross Section Estimation

The Radar Cross Section (RCS) of a target is a measure of how easy or hard is to detect it with a radar system. It is measured in area units ($m^2$ or dBsm) as it represents the effective area that intercepts a transmitted signal and scatters it to a radar receiver [138].

In this thesis, the targets' RCS estimation is carried out by simulation techniques employing Ansys HFSS (High Frequency Structure Simulator) [139]. Two different approaches are proposed taking in consideration the electric size of the target. If the target size is less than $10\lambda$, its RCS is in Rayleigh or Resonance regime, so full-wave electromag-

netic simulation is employed. On the contrary, if its size is greater than $10\lambda$, the RCS is in optical regime, so a multi-bounce rays approach with physical theory of diffraction (PTD) correction is employed. This method is available in Ansys simulator with the name Shooting Bouncing Rays (SBR+) and it provides really precise results for large structures in which full-wave simulations are not possible due to computational cost.

The Bistatic RCS (BRCS or $\sigma_{bis}$) simulation is carried out by defining an incident wave in a specific point of the target and setting the observation angle (or reflection) forming a bistatic angle ($\beta$) with the incidence one. Employing the different scenarios information, the BRCS can be calculated accurately in each point of a trajectory (e.g. roads), or estimated through some statistics for a set of possible cases in an scenario when the trajectory is unknown or random (e.g. UAV free flight trajectory).

### 4.1.1   Targets BRCS at DVB-T frequencies

Terrestrial, maritime and aerial scenarios have been presented for exploiting DVB-T as IoO, so targets typical of those scenarios have been studied: small and big cars and a truck for ground scenarios, a frigate for maritime one and a drone and a commercial plane for aerial ones. Every target 3D model is configured to be made of aluminium material except for the case of the drone in which glass fibre is employed for the body and blades, lithium for the battery and aluminium for the rotors. Top views of the studied targets with its BRCS at 700 MHz for incidence angle of $\phi_i = 0°$ and $\theta_i = 90°$ (in the front of each one) and all azimuth reflection angles ($\phi_r \in [0° - 360°]$ and $\theta_r = 90°$) are shown in Figure 4.1.

Considering reference scenario described in Section 3.4.1.1 and two ground targets (an small car and a truck) moving along the two main roads in the two possible ways (moving away and approaching to the PR), which fulfil incidence and reflection angles represented in Figure 3.6, their BRCS curves at each point of the trajectory are represented in Figure 4.2. BRCS varies significantly for the same target as a function of its location (point of the trajectory) and its way on the road.

In the case of maritime and aerial scenarios, the targets trajectories are usually unknown in advance, so targets BRCS must be studied as a function of possible bistatic angles $\beta$ for all possible incidence and reflection angles. In case of aerial targets, it is considered that they are very far away from the IoO, so the incidence angle is approximately $\theta_i = 90°$, and reflection one is set to $\theta_r = 100°$, which means a ratio between distance and altitude to respect the PR position of approximately 17/100. Figure 4.3 shows the BRCS of the frigate, plane and drone simulated for all incidence and reflection azimuth angles.

The results of simulated BRCS are summarized in Table 4.1 as a function of bistatic angles at two frequencies. For each bistatic angle, all possible combinations $\phi_i$ and $\phi_r$ that fulfils that $\beta$ are taken, and its geometric mean is calculated. The geometric mean is selected because it is appropriate for estimating the central tendency of a set of logarithmic data.

(a) Small car

(b) Big car

(c) Truck

(d) Frigate

(e) Drone

(f) Plane
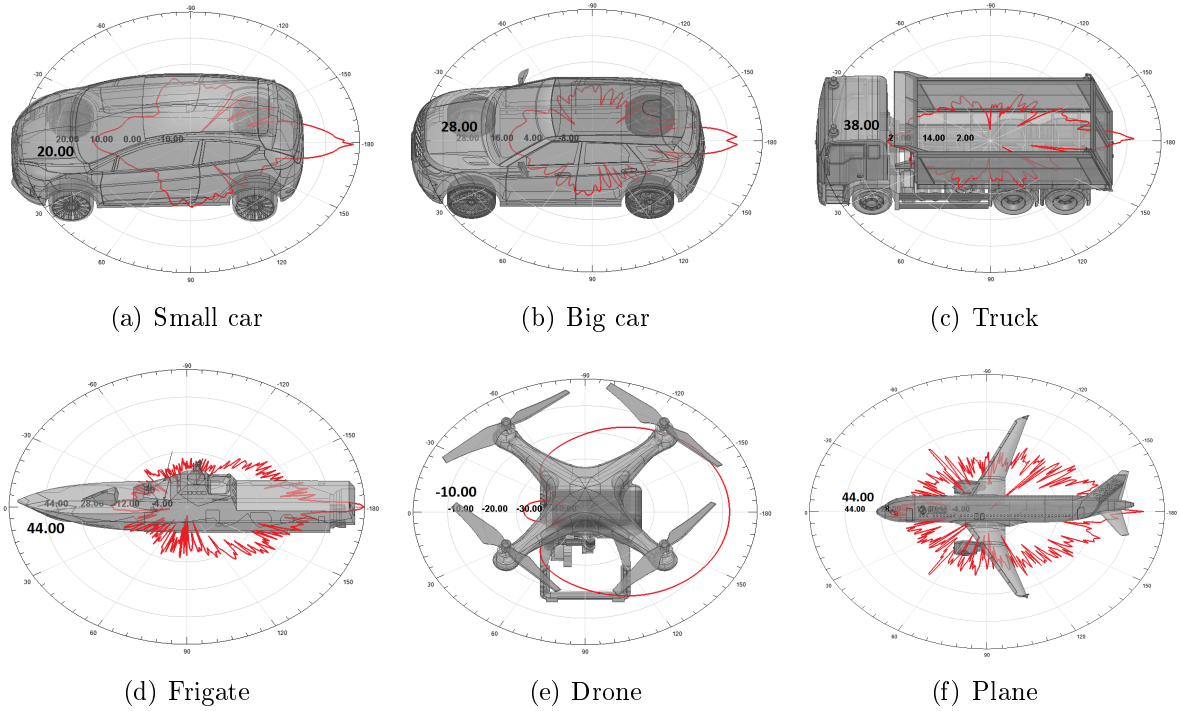
Figure 4.1: Targets' models for BRCS simulation and its BRCS for $\phi_i = 0°$ at 700 MHz.



(a) M-121

(b) R2
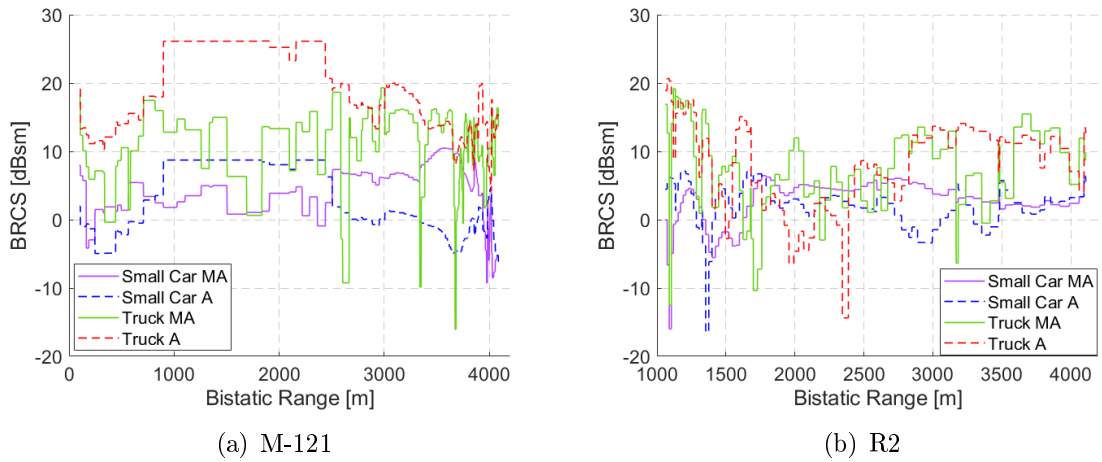
Figure 4.2: Targets' BRCS at 700 MHz associated with their trajectories along M-121 and R2 roads, in both directions moving away to the PR (MA) and approaching to it (A).

## 4.1.2 Targets BRCS for DVB-S IoOs

BRCS of terrestrial targets following the trajectories along the roads described in Section 3.4.1.2 are also studied for the case of employing DVB-S IoOs. The incident wave is configured having in mind the elevation at which the satellite is seen from the selected

(a) Frigate　　　　　　　　　(b) Plane　　　　　　　　　(c) Drone
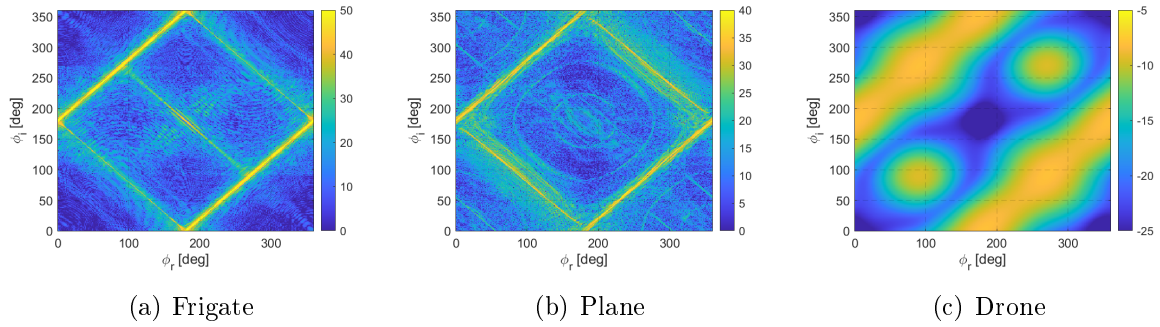
Figure 4.3: Targets' BRCS at 700 MHz for all incidence and reflection azimuth angles.

Table 4.1: Geometric mean of the BRCS (dBsm) at all possible incidence and reflection angles that fulfil a given bistatic angle $\beta$ for maritime and aerial targets at two frequencies within DVB-T band.

| | Frigate | | Plane | | Drone | |
|---|---|---|---|---|---|---|
| $\beta$ | 600 MHz | 700 MHz | 600 MHz | 700 MHz | 600 MHz | 700 MHz |
| 0° | 13.7 | 13.2 | 12.3 | 13 | -12.4 | -18.4 |
| 30° | 11.2 | 11.9 | 12.2 | 12.1 | -12.5 | -18.9 |
| 45° | 10.1 | 9.6 | 12.2 | 11.7 | -12.5 | -19.4 |
| 90° | 9.8 | 9.4 | 11.5 | 11 | -11.5 | -19.4 |
| 135° | 10.4 | 10.4 | 11 | 11.5 | -9.2 | -14.3 |
| 180° | 40 | 40.5 | 23.5 | 22.1 | -8.4 | -12.9 |
| **Total** | **13.5** | **13.1** | **13.2** | **13.1** | **-10.1** | **-15.3** |

AoI ($\theta_i = 55°$) and $\theta_r = 90°$. All azimuth angles $\phi_i$ and $\phi_r$ have been simulated. BRCS estimations of the big car and the truck along both roads are shown in Figure 4.4. It is interesting to check how in this case, due to the fact that the incidence in elevation is different from horizontal, the shape of the incidence surface has a great influence in the BRCS. When a car is approaching, the wave impacts mainly in the bonnet, which is an inclined surface that guide the reflection to the opposite direction of the receiver, decreasing target BRCS. Similarly, when the truck is moving away, the inclined back part of the tank makes the BRCS decrease till a level similar or even smaller than the big car's moving in the same way. This is interesting having in mind that the area in the truck's back part, avoiding the wheels zone, is approximately 1.6 times greater than car's one.

## 4.2　Coverage estimation

Radar Range Equation can be employed to estimate the coverage of the passive radar system once the BRCS of the targets $\sigma_{bis}$ has been calculated and the geometrical parameters of the deployment are known. Particularizing for the bistatic case, the power

(a) Nursing School Street

(b) M-121
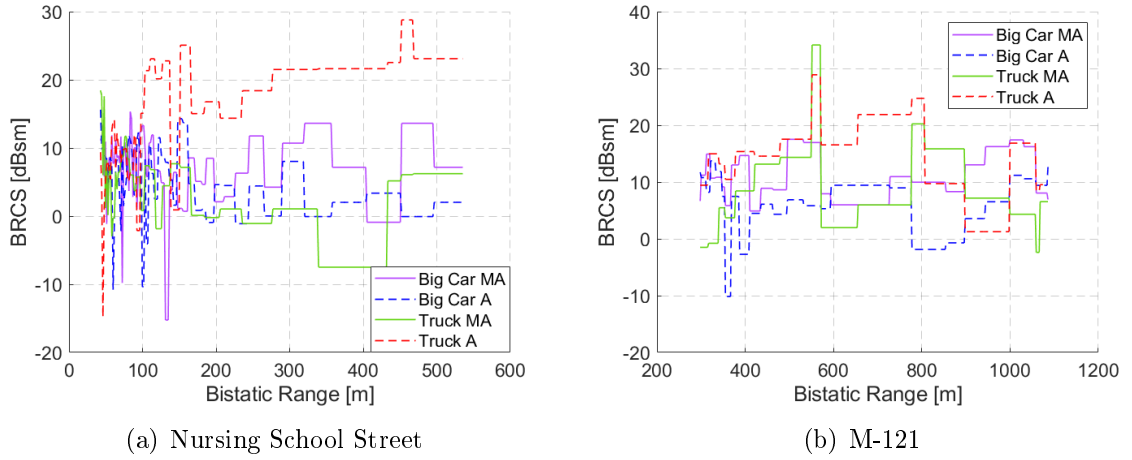
Figure 4.4: Targets' BRCS at 11 GHz associated with its trajectories along the roads described in scenarios of Section 3.4.1.2, in both directions moving away to the PR (MA) and approaching to it (A).

received at the PR from target echo ($p_r$) can be estimated employing Equation 4.1.

$$p_r = \frac{p_t \cdot g_t \cdot \lambda^2 \cdot \sigma_{bis} \cdot g_r \cdot}{(4\pi)^3 \cdot R^2_{IoO-Target} \cdot R^2_{Target-PR} \cdot l_{e_{IoO-Target}} \cdot l_{e_{Target-PR}}} \quad (4.1)$$

The maximum range or coverage from the PR ($R_{Target-PR}$) can be estimated if the minimum required power in the receiver or system sensitivity is known. The passive radar sensitivity varies as a function of the opportunity signal, because different elements are employed in the acquisition chain, and is a function of system and processing parameters:

- For DVB-T as IoO, considering an acquisition bandwidth of 25 MHz containing three DVB-T channels and employing an integration time $T_{int} = 250$ ms, as a compromise solution between to achieve the better Doppler resolution and integration time avoiding targets spreading in Doppler and range, the system sensitivity for $P_D = 80\%$ and $P_{FA} = 10^{-6}$ ($SNR_{det} = 17.5$ dB) is $S_{sys} = -131.2$ dBm. A 5 dB margin for interferences is included. $SNR_{det}$ has been calculated for a square law envelope detector and an observation space characterized by Swerling I targets in AWGN [33].

- For DVB-S as IoO, considering an acquisition bandwidth of 100 MHz with two DVB-S channels of 30 MHz each one, and employing an integration time $T_{int} = 200$ ms, the system sensitivity for $P_D = 80\%$ and $P_{FA} = 10^{-4}$ ($SNR_{det} = 16$ dB, same detector and target model than for DVB-T case) is $S_{sys} = -149.4$ dBm.

The excess losses ($l_e$) to be considered also vary as a function of the IoO and radar scenario. For DVB-T signals, $l_e$ considers the excess losses from free space propagation due to diffraction phenomena [140], that will have greater importance in the case of

ground targets. A software for estimating link budget considering terrain relief effects was employed to calculate diffraction due to $1^{st}$ Fresnel ellipsoid clearance. Isotropic antennas are simulated in each link nodes at the height of real IoO and PR, and in the case of the targets, 1 m height for terrestrial, 2 m height for maritime and 50 m height for aerial ones, considering the worst case for UAV flights. The difference between free space path losses and simulated with terrain influence is computed. In the case of DVB-S, it has been checked that due to the elevation of the transmitter and the higher frequency, which reduces the radios of Fresnel ellipsoids, losses due to diffraction can be left out but as the frequency surpass 10 GHz, losses due to rain and atmospheric gases must be considered [141] [142]. The excess losses considered in each scenario for DVB-T case are summarized in table 4.2. For the study purposes, the excess losses in each scenario have been calculated for two points, always in the centre of the AoI, at difference distances from PR or different flight altitudes over ground level in case of aerial targets. In DVB-S case, the excess losses at 11 GHz are: 2.23 dB in the path from IoO to target; 0.18 dB in the path from target to PR in the worst case (propagation path of 1 km).

Table 4.2: Excess losses considered for coverage estimation in each of the proposed scenarios at 700 MHz.

| Scenario | $R_{Target-PR}$ | $h_{Target}$ | $L_{e_{IoO-Target}}$ | $L_{e_{Target-PR}}$ |
|---|---|---|---|---|
| **Semi-urban** | 0.5 km (M-121) | 1 m | 5.69 dB | 0.02 dB |
| | 1.8 km (R2) | 1 m | 8.74 dB | 6.58 dB |
| **Maritime** | 3.8 km | 3 m | 8.53 dB | 5.55 dB |
| | 12.4 km | 3 m | 5.38 dB | 13.05 dB |
| **Rural 1** | 0.5 km | 50 m | 23.4 dB | 0 dB |
| | 0.5 km | 100 m | 5.33 dB | 0 dB |
| **Rural 2** | 0.4 km | 50 m | 0 dB | 0.01 dB |
| | 0.8 km | 100 m | 0.47 dB | 0 dB |

In figure 4.5 coverage curves as a function of BRCS are shown for references scenarios, considering in each of them the worst case of $l_e$ among those summarized in Table 4.2, except in the case of rural scenario 1, in which an obstacle increases the losses when targets flight at an altitude of 50 m, so also losses for targets flighting at 100 m are included. Antenna systems using single radiating elements with a gain of 6 dBi and an array of 7 elements with a gain of 14.5 dBi are assumed.

In DVB-S case, the excess losses are mainly due to the space-ground segment, so they can be considered constant for any $R_{Target-PR}$ in the range of values that it is being evaluated. This fact, allows to calculate the required antenna gain for being able to detect big cars at a given distance from the PR in each scenario along both ways (Figure 4.6), according to the estimated BRCS (Figure 4.4).

(a) Semi-urban

(b) Maritime

(c) Rural scenario 1

(d) Rural scenario 2
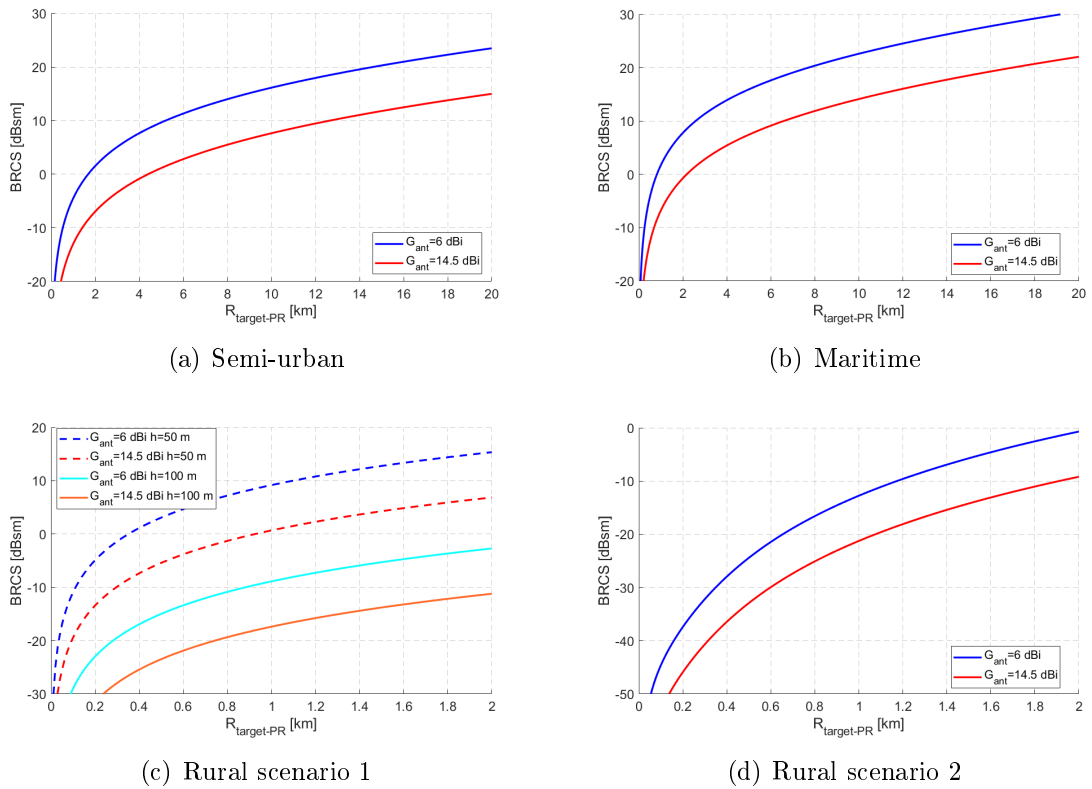
Figure 4.5: Estimated coverages for references scenarios with excess losses from table 4.2.
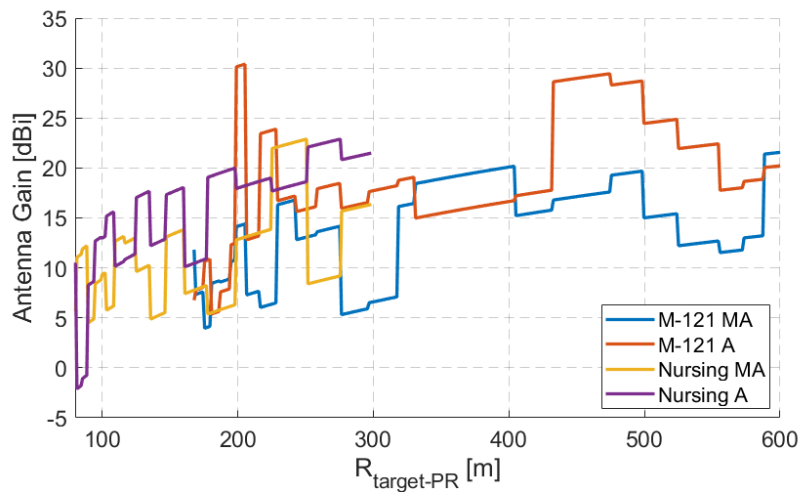


Figure 4.6: Required antenna gain for detecting big cars at an specific distance far from the PR employing DVB-S IoO.

## 4.3    Simulation of BRCS fluctuations along the trajectory

Nowadays, small UAVs are one of the targets that awake more interest. Besides of detection, the capability of classification is a key element for risk analysis and selection of the most appropriate countermeasures.

Classification of small targets such as UAVs through passive radar imaging could be a hard task due to the size of these targets and the resolutions that are normally achieved exploiting terrestrial broadcasting signals. DVB-S is most suitable for radar imaging due to the higher operating frequencies, but the high propagation losses and the low BRCS of these targets make detection really challenging. This section presents and alternative approach based on modeling BRCS fluctuations along different trajectories. Bistatic geometries provide variation in RCS of targets in all possible movements, even if the targets is approaching radially to the receiver, as the bistatic angle $\beta$ changes due to the relative movement with respect to the transmitter.

Two trajectories generated by the GPS data of real UAV flights were employed for studying the BRCS fluctuation of different targets: one linear and one spinning (Figure 4.7(b)).



(a) Trajectories

(b) Range bins from GPS data

(c) Angles for trajectory 1

(d) Angles for trajectory 2
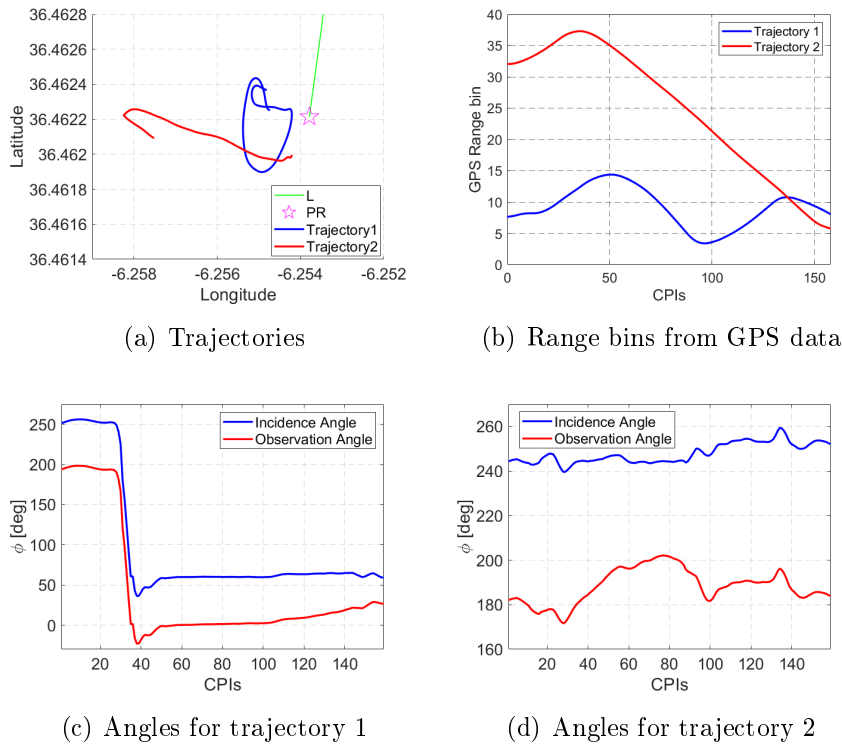
Figure 4.7: Trajectories employed for studying the variation of BRCS and the associated incidence and reflection angles.

Incidence and observation angles in both planes were calculated using the transmitter's and receiver's positions (Figures 4.7(c) and 4.7(d)). Drone attitude parameters (yaw, pitch, and roll) were also available. Azimuth incidence and observation angles were first calculated with respect to the North and corrected with yaw parameter to keep the model fixed in the simulator pointing towards + X-axis, and setting up the incidence waves and observation angles in the precise points of the model. Real pitch and roll data were also included in the simulation.

Three different UAV models were employed for the study: a commercial DJI Phantom III, and two scaled versions of military ones: the MQ-1 Predator of General Atomics and a helicopter. The military models were scaled to study the influence of drone geometry and avoid the impact of different sizes. The materials assigned to the 3D models of the different drones were selected according to the available data about manufacturing characteristics (Figure 4.8).



Figure 4.8: Targets' models employed for BRCS fluctuation study.

An electromagnetic simulation for each point of the trajectory was set up with the incident plane wave, which is horizontally polarized, impinging on the centre of the model with the incidence and observation angles calculated previously, and the model imitating the real attitude parameters. The simulated BRCS of each target along the sample trajectories (Figure 4.9) shows how as a function of the movement the variation in BRCS of each target differs from the others, encouraging a further study for evaluating their potential use for feature extraction and classification.

(a) DJI Phantom III        (b) Scaled MQ-1 Predator        (c) Scaled helicopter



(d) Trajectory 1               (e) Trajectory 2
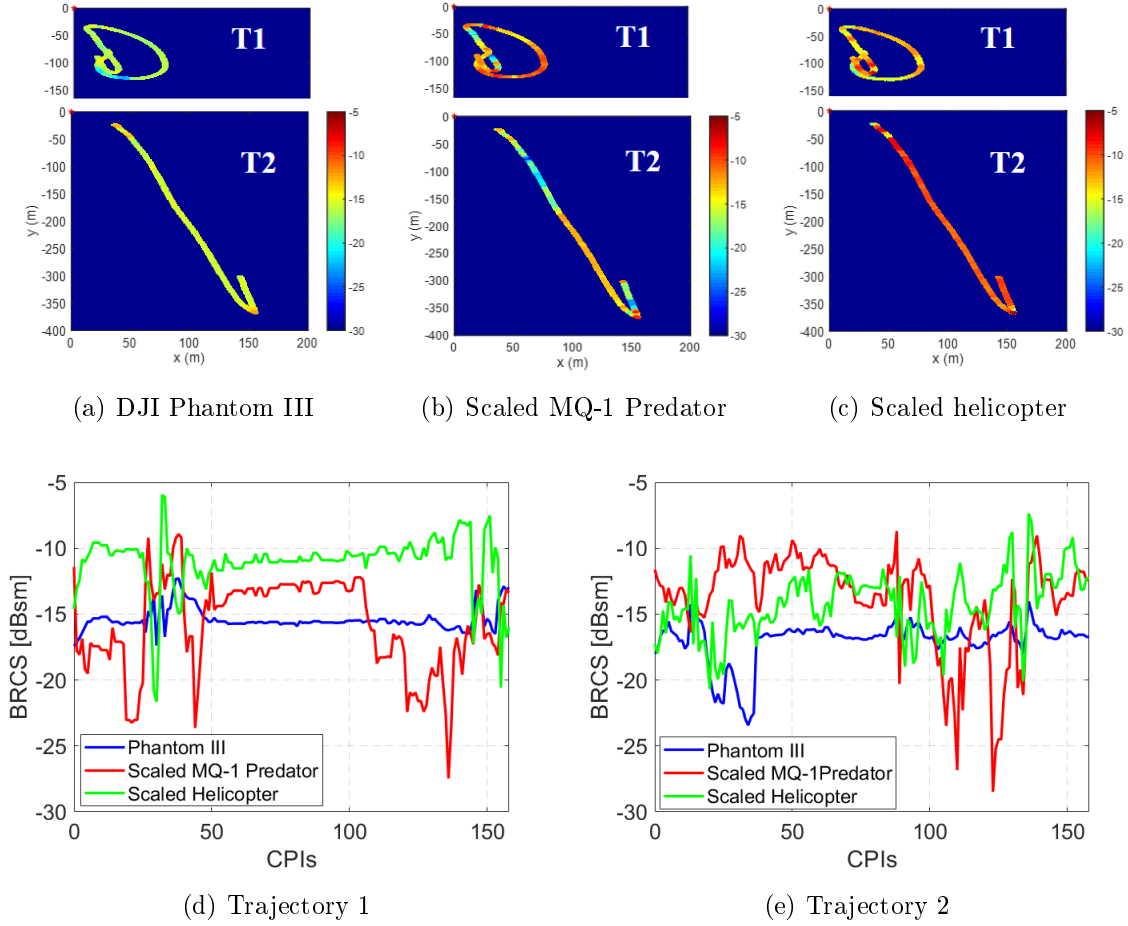
Figure 4.9: Variation of simulated BRCS of each target for each of the trajectories.

These results were presented in the NMSG-SET[1] 183 Specialists' Meeting on *Drone Detectability: modelling the relevant signature* [143]. For validating the proposed simulation approach, a methodology was also presented for estimating the BRCS from the CAF generated using real row data. The most relevant result is presented in (Equation 4.2).

$$\sigma_{bis}(m_{tg}, p_{tg}) = |s^{CAF}(m_{tg}, p_{tg})|^2 \frac{R_{tg-PR}^2 \cdot R_{IoO-tg}^2}{C_{PR\_scenario}} \tag{4.2}$$

$\sigma_{bis}(m_{tg}, p_{tg})$ is the equivalent simulated BRCS and $s^{CAF}(m_{tg}, p_{tg})$ is CAF value, being $m_{tg}$ and $p_{tg}$ the time and Doppler shift bins where the maximum of the CAF output due to the target echo contribution is located. $C_{PR\_scenario}$ is a constant that depends on scenario characteristics such as the transmitted power, the gain of Tx and Rx antennas and the distance from IoO to PR ($R_{IoO-PR}$). $C_{PR\_scenario}$ allows to normalize the BRCS to avoid the dependence with the scenario parameters.

---

[1]NMSG: NATO Modelling & Simulation Group; SET: Sensors & Electronics Technology panel

Figure 4.10 compares the CAF values of the trajectories of a DJI Phantom III obtained from real data in the maritime scenario described in Section 3.4.2 with the corrected simulated data (Equation 4.3). Some data obtained from the real flight of the Phantom III were discarded due to the high levels of interference present in CAF regions close to the zero Doppler line and close to the PR location. Interference level was also estimated to verify the assumed low SIR values at the discarded trajectory points.

$$|\widehat{s^{CAF}}|^2 = \sigma_{bis_{sim}} \frac{C_{PR\_scenario}}{R_{tg-PR}^2 \cdot R_{IoO-tg}^2} \tag{4.3}$$



(a) Trajectory 1        (b) Trajectory 2
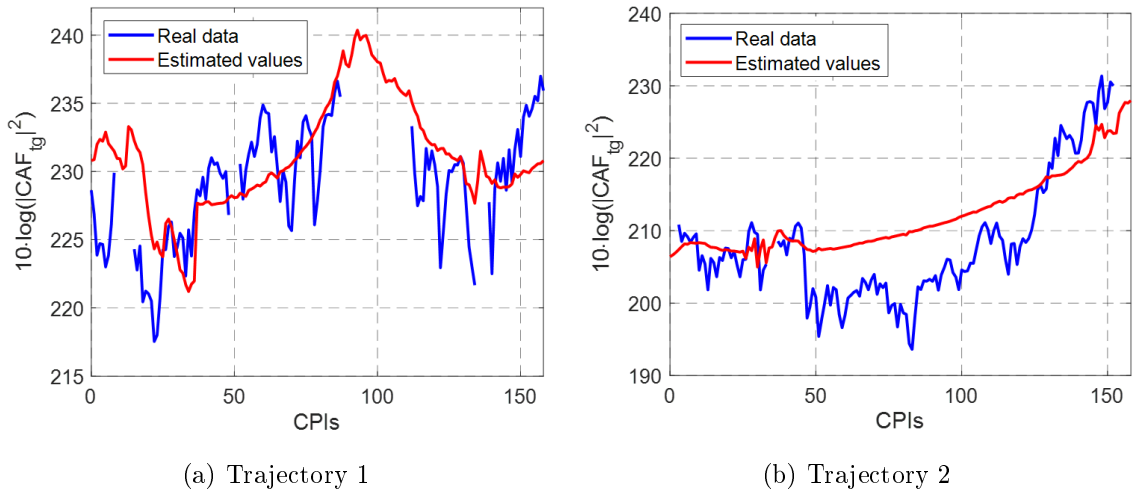
Figure 4.10: Comparison of CAF values for both trajectories.

## 4.4 Air-screws micro-Doppler Signature Characterization

Micro-Doppler signatures refer to Doppler components around the main Doppler shift contribution, that are produced by movements of target's components such as the drone air-screws or helicopter propellers. They have been investigated in literature for target detection and classification in radar surveillance applications [144, 145]. Once the capability of passive radar small UAVs detection has been proved, [146], the next research stage is the study of the potentials of air-screws micro-doppler signatures for targets classification.

The signature of a target will vary depending on its speed, the number of blades and their size, the rotating speeds, and/or the roll/pitch angles in the target movement. The analysis of micro-Doppler data and the extraction of their features could be useful to discriminate targets from other clutter sources, improving detection when target's main Doppler components are near zero, and for classification.

Ansys HFSS electromagnetic simulator was employed to characterize the radar signature of the drone air-screws. First, the simple case of a monostatic scenario with targets with null roll, yaw and pitch angles was studied. In this case, the air-screws Doppler velocity will approximate to its tangential velocity at the edges (Equation 4.4), being $f_{rot}$ the rotation frequency in turns per second and $R$ the radius of the air-screws. Two different quad-copter models were studied, with air-screws' radius of $R_1 = 210$ mm and $R_2 = 122$ mm and two rotating velocities, $f_{rot_l} = 60$ rps and $f_{rot_h} = 100$ rps. Figure 4.11 shows the simulation results: the UAV body is observed with high power at zero Doppler in range 100 m while the air-screws signature extends to positive and negative Doppler velocities around the main body contribution, being those velocities directly related to the size of the blades ($R$) and the turn speed ($f_{rot}$).

$$v_t = \omega \cdot R = 2\pi \cdot f_{rot} \cdot R \qquad (4.4)$$



(a) Model 1 $f_{rot_l} = 60$ rps  (b) Model 2 $f_{rot_l} = 60$ rps  (c) Model 2 $f_{rot_h} = 100$ rps
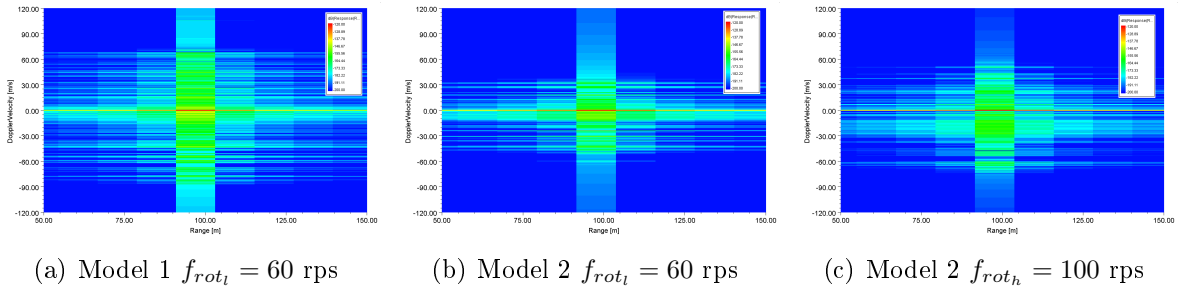
Figure 4.11: Simulated air-screws micro-doppler signature for two drone models: model 1 with $R_1 = 210$ mm and $f_{rot_l} = 60$ rps and model 2 with $R_2 = 122$ mm and both rotation speeds $f_{rot_l} = 60$ rps and $f_{rot_h} = 100$ rps.

Designing a good classification technique requires a big training database that could be generated through simulation. In order to check the similarity between simulated Doppler signatures and real ones, the bistatic geometry of scenario in Section 3.4.3 was replicated, while *model 2* characteristics are the same of one of the controlled targets employed in that scenario (Table 4.3). The model was located in the middle of the real path, 500 m away from the PR, and fixing $\beta = 58.3°$. The height of the drone was fixed at 0 m, the height of the transmitter to 7.46 m, and PR's one to $-100$ m. In Figure 4.12, the simulated scenario is shown, where R1 and R2 are the left and right back rotors, respectively, and R3 and R4 are the right and left front rotors, respectively.

Null speed was assigned to the drone to appreciate the real effects of airscrews movement. The maximum angular speeds of the airscrews were extracted from the .DAT file of the GPS device, which are summarized in Table 4.3. As the drone in its real movement tended to slant towards the front, a pitch angle of 18° was set up (greatest observed value in .DAT file).

Table 4.3: Main DJI Matrice 200 flying parameters

| **Type:** quadcopter | | **Size (mm):** 883 x 886 x 398 | |
|---|---|---|---|
| **Speed:** 7m/s | | **Initial distance:** 500m | |
| **Bistatic angle:** 58.3° | | **Tilt angle:** 18.6° | |
| **Rotors airscrew speed (rps)** **(Maximum values)** | Back | | Front | |
| | Left | Right | Left | Right |
| | 66 | 55 | 56 | 47 |
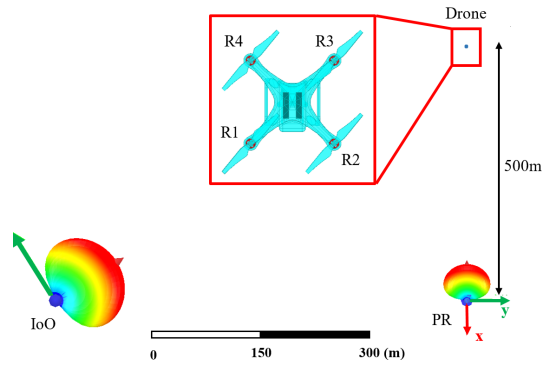


Figure 4.12: Simulated radar scenario

Theoretically, the maximum tangential speed at the edges of the airscrews is 83 m/s. This maximum speed is expected to be decreased in CAF output due to the bistatic geometry, differences in heights of IoO, PR and drone, and the pitch of the drone in its movement. Simulation results in Figure 4.13(a) try to approach the real Doppler airscrew signature for the maximum speed case. It is shown that maximum Doppler velocity due to airscrews, in this simulation case, is approximately $\pm 50$ m/s, which corresponds to Doppler shifts of around $\pm 260$Hz for the operating frequency of 770MHz.

In Figure 4.13(b), the superimposition of the detector outputs in the 160 CPIs of real data acquired with IDEPAR demonstrator is presented. A group of detections corresponding to the cooperative drone (marked in green) are identified using the GPS data. Groups of detections (marked in red) appearing in different Doppler shifts at the same range bin of the drone are associated with the airscrews signature of the target. In [147] it was demonstrated that a tracker stage can differentiate and associate groups of detections to the main body of the target, if their range movement and Doppler shift information have a direct correspondence. A track with 160 detected points was obtained, giving rise to a $P_D = 100\%$ for the drone. Also, the track validation process produced 11 valid replica tracks related to the drone's one in different Doppler shifts, due to the air-screws movement (Figure 4.13(c)).

(a) Simulation    (b) Cumulative detections from    (c) Tracker system output
                  real data
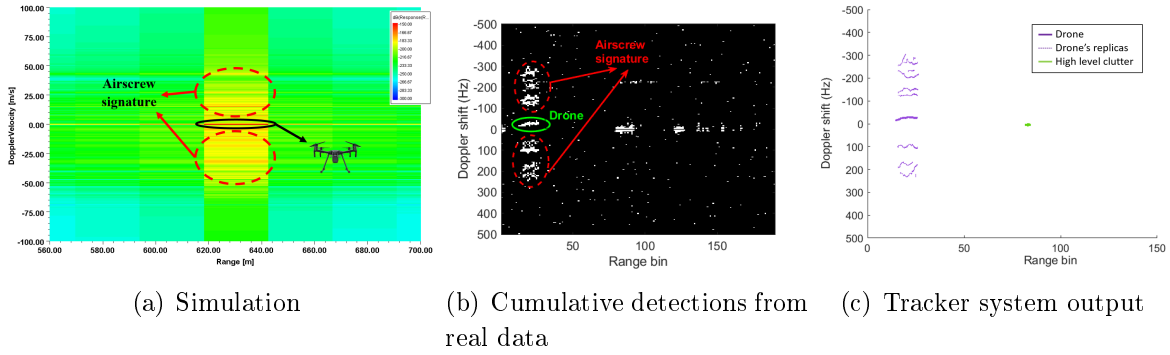
Figure 4.13: Simulation and real data results for the study of micro-doppler air-screws signature.

The Doppler shifts of the replicas with respect the main one, in both the positive and negative sides, were estimated to extract information of the drone's signature. An average value of 234.41 Hz for the positive Doppler and $-247.47$ Hz for the negative one was obtained, being the maximum Doppler shift difference between the airscrews and the drone body of 277.47 Hz. Results agree with the simulation process in which a Doppler shift around $\pm 260$ Hz was estimated.

## 4.5    Bistatic ISAR imaging for targets classification

Inverse Synthetic Aperture Radar (ISAR) techniques take advantage of the targets' movement to generate images from their backscattered energy that can be employed for classification purposes.

ISAR is based on the fact that when an electromagnetic wave impinges on a target, different points of this target called scattering centres (SC), generate different scattered fields which amplitude and phase contain the distance information of the SC.

ISAR image can be regarded as the display of range and cross-range profiles of the target in the 2D (range/cross-range) plane. The range profile of a target is the returned waveform shape when it is illuminated with sufficient frequency bandwidth (BW). The cross-range profile is generated from the echoes of the target at different look angles [148]. Therefore, ISAR exploits frequency and angular diversity.

The look angles $\Omega_i$ are defined as the observation angles seen by an equivalent Synthetic Aperture Radar (SAR) when moving around a target (Figure 4.14). The aspect width of look angles $\Delta\Omega$ defines the cross-range resolution of an ISAR image. Finally, the Aspect Angle $\alpha$ is defined as the angle forming the central look angle ($\Omega_{M/2}$) with a reference, for example the front of the target. In the scheme of Figure 4.14 if the plane nose is set as the reference, $\alpha = 0°$.
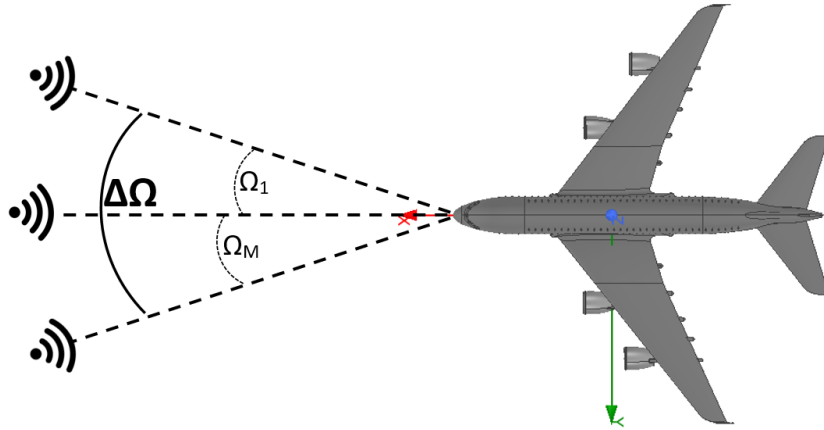
Figure 4.14: Scheme of parameters for ISAR images.

If the target is illuminated with a stepped frequency continuous wave (SFCW), the IFT of the received signal characterizes the target's range profile. If the frequency bandwidth is small, around one tenth of the central frequency, and also it is the width of look angles, an ISAR image can be formed by generating a range profile for each look angle $\Omega_i$ and integrating the information of the M range profiles through the IFT along cross-range dimension. The required frequency and angle information of a target can be obtained by simulating its complex RCS at different frequency points, and for a set of incidence-observation angles fulfilling every look angle $\Omega_i$. An example of a monostatic range profile and ISAR image of a commercial *Airbus A380* simulated in ANSYS HFSS through its complex RCS is shown in Figure 4.15. The main reflector surfaces seen from the aspect angle are mainly the nose and engines and produce hot spots in the ISAR image. Those hot spots can be employed to extract characteristics from the target, such as distance between different scatterers or shape.



(a) Range Profile
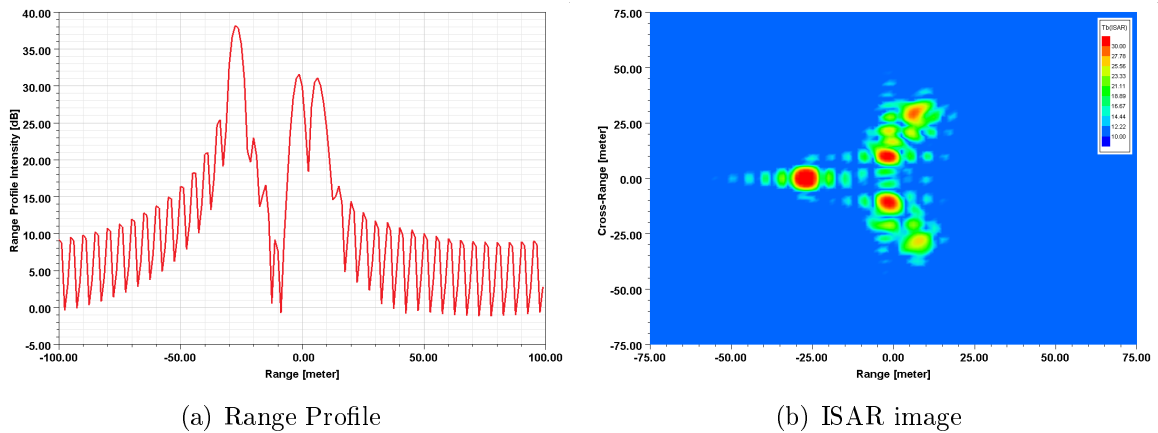


(b) ISAR image

Figure 4.15: Monostatic range profile and ISAR image of a A380 with $f_c = 10$ GHz, $BW = 150$ MHz, $\alpha = 0°$ and $\Delta\Omega = 0.18°$.

For bistatic ISAR (BISAR) generation, the same procedure can be followed adjusting the parameters to bistatic geometry. Each angular point for simulating BRCS is now defined by a pair incidence-reflection angle ($\phi_i^{inc} - \phi_i^{ref}$) forming the bistatic angle $\beta_i$. Following the Bistatic Equivalent Monostatic (BEM) ISAR geometry [37], that proposes to substitute bistatic Tx and Rx by an BEM element in the bisector of $\beta$, the aspect angle is defined as the angle sustained from the reference to that BEM element. The aspect width $\Delta\Omega$ can be calculated as the range of aspect angles in the BEM case for the set of pairs $\phi_i^{inc} - \phi_i^{ref}$. The bistatic range and cross-range resolutions are defined by Equations 4.5 and 4.6.

$$\Delta r_{bis} = \frac{c}{2 \cdot BW \cdot \cos(\beta/2)} \tag{4.5}$$

$$\Delta cr_{bis} = \frac{\lambda}{2 \cdot \sin(\Omega) \cdot \cos(\beta/2)} \tag{4.6}$$

Bistatic ISAR provides some advantages with respect monostatic ones. The first one is due to the fact that a good ISAR image requires a significantly change in target aspect angle. For this reason, in monostatic case, when the target moves radially to the radar the ISAR image cannot be produced. In bistatic geometry, this problem is avoided. Another important advantage appears when considering stealthy targets. These kind of targets are specifically designed to avoid radar detection, by absorbing and/or cattering the radar signal to directions other than the incidence one. This characteristic concerns monostatic radars but not bistatic ones, in which the detection and ISAR generation capabilities of those targets are less affected by their stealthy nature.

### 4.5.1    BISAR images simulation

A trajectory for aerial targets has been defined to estimate the ISAR parameters for image simulations. The locations of transmitter and receiver have been fixed and ISAR images have been simulated for three different points along the trajectory (Figure 4.16).

For defining the range of angles covered by the targets at each location (point) to generate an image, the velocity of the target was set to 100 m/s. The illumination time $T_i$ s was defined for each point in such way that the cross-range resolution remained below 5 m. In this way, the central incidence and reflection angles and their range of angles covered during $T_i$ were estimated, and the aspect angle and $\Delta\Omega$ for the BEM approximation were calculated. The signal frequency was 3 GHz and the bandwidth 100 MHz. Table 4.4 summarizes the main bistatic ISAR simulation parameters for the three points. If the bistatic angles $\beta$ change between the pairs ($\phi_i^{inc} - \phi_i^{ref}$) a phase correction must be applied to each range profile to avoid distortion caused by a non-constant bistatic angle in the angular points of the same image.
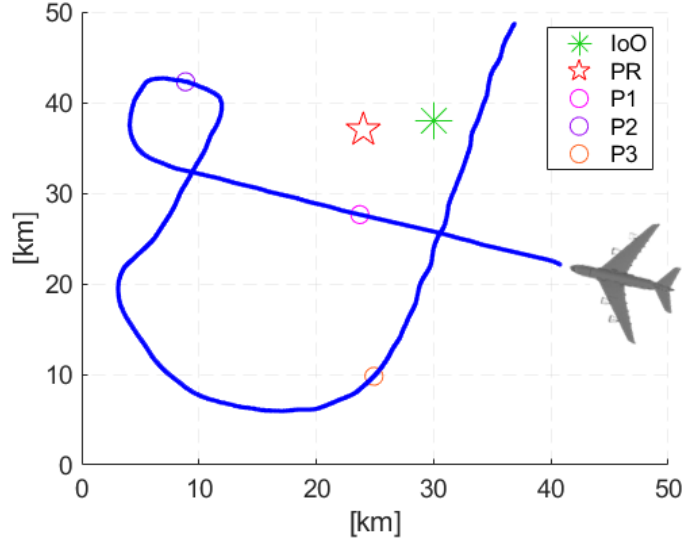
Figure 4.16: Trajectory of an aerial target for ISAR simulation with the positions of the IoO and PR and three points of the target along the trajectory (P1, P2, P3).

| Parameters | P1 (752) | P2 (2173) | P3 (4724) |
|:---:|:---:|:---:|:---:|
| $T_i$ | 5 s | 15 s | 10 s |
| $\alpha$ | 270° | 5° | 30° |
| $\Delta\Omega$ | 2.64° | 0.72° | 1.04° |
| $\beta$ | 29.5° | 7.8° | 12.1° |
| $\Delta r_{bis}$ | 1.55 m | 1.50 m | 1.51 m |
| $\Delta x r_{bis}$ | 1.12 m | 3.97 m | 2.76 m |

Table 4.4: Simulation parameters for BISAR images in the selected points of the trajectory.

The simulation of BRCS were carried out in ANSYS HFSS for a design of four simple scatterers and 3 aerial targets, one commercial and two military ones. The parameters shown in Table 4.4 were employed to configure the frequency and angle points for BRCS simulation. The method employed is shooting and bouncing rays (SBR+) with physical theory of diffraction (PTD) correction, which is configured for a maximum of 5 bounces and 2 rays per wavelength. Simulation results are shown in table 4.5.

The results presented in Table 4.5 shows that having in mind the aspect angle in each case, which can be seen as a rotation of the target in the image, the size and shape of each target can be extracted from the images' hot spots. Selecting one of the images, for example for A380 target, because it is bigger so the hot spots can be easily differentiated, and point 3, which aspect angle is 30°, a detailed analysis of the results achieved is carried out (Figure 4.17):

- Applying BEM approach, $\alpha = 30°$ represents that the monostatic radar will illumi-

| 4-Scatters | Airbus A380 (Commercial) | Eurofighter Typhoon (Fighter) | Xian H-6K (Bomber) |
|---|---|---|---|
|  34m / 24m |  73m / 81m |  16m / 11m |  34m / 31m |
| P1  | P1  | P1  | P1  |
| P2  | P2  | P2  | P2  |
| P3  | P3  | P3  | P3  |
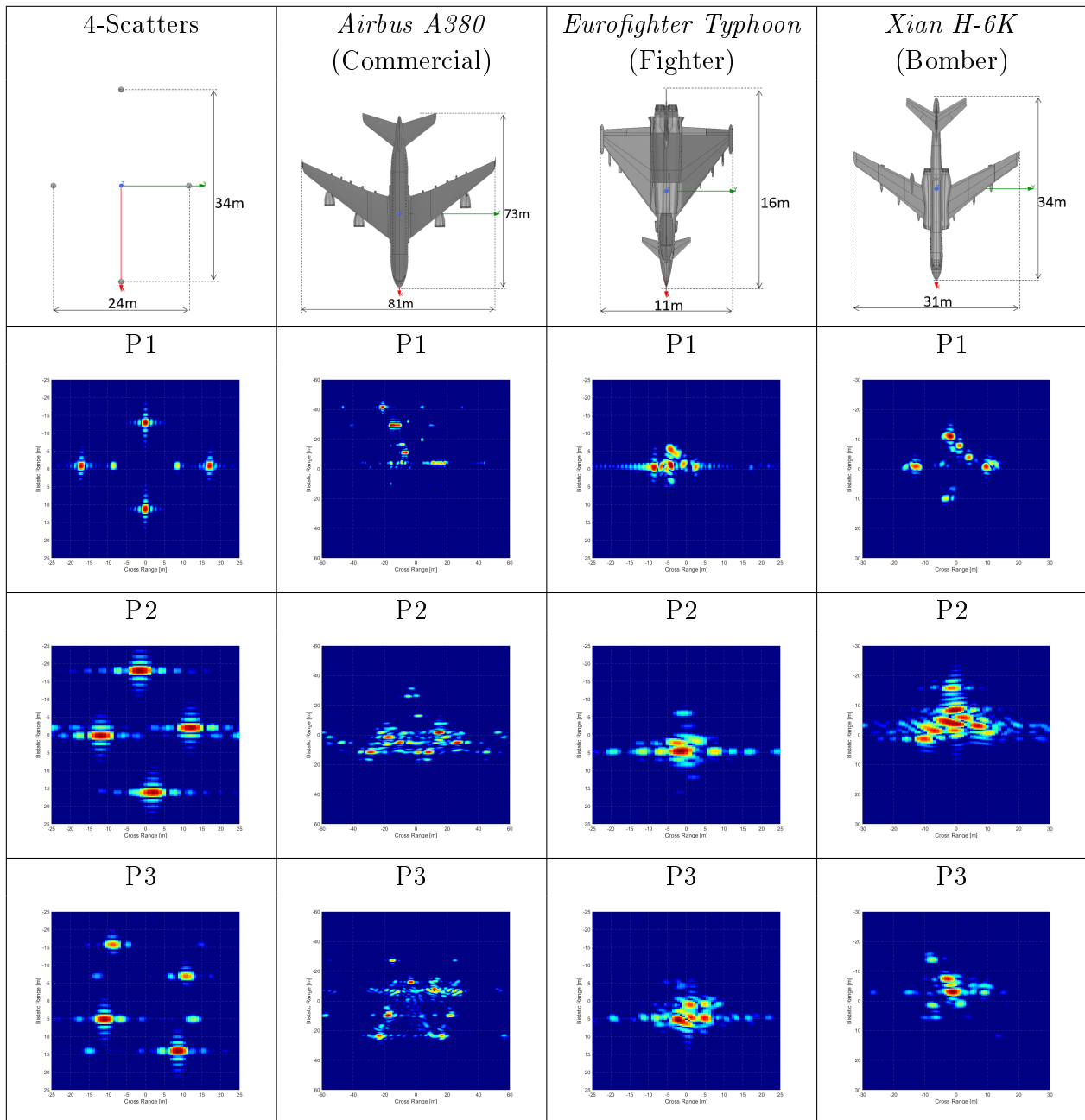
Table 4.5: Simulated BISAR images.

nate the target at that angle from the nose in anti-clockwise sense if it is seen from top.

- The cockpit will be the nearest scatterer in range dimension and, as it will be seen at the left of the incidence wave, it appears in negative cross-range.

- The scatters produced by engines allow to sketch the wings shape and to predict the separation between engines. As examples, separation between engines are around

(a) Target analysis



(b) BISAR image with marked hot spots
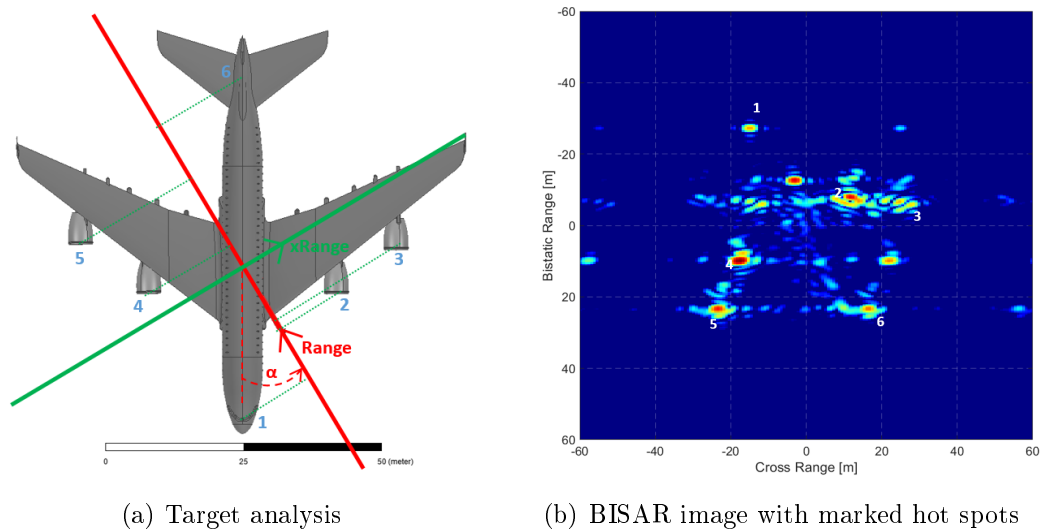
Figure 4.17: Bistatic ISAR image analysis of *Airbus A380* in study point 3 (P3).

$15-16$ m and a similar separation is observed between hot spots 2 and 3, or between 4 and 5, in the BISAR image.

- The scatterer associated to the tail stabilizer is marked as hot spot number 6. The distance in the model from the cockpit to the vertical stabilizer is around 60 m, while the distance in image between hot spots 1 and 6 is around 58 m ($HP1 = (-15, -27)$ and $HP6 = (16, 23)$), so it is proved that this simulated image can be employed to estimate target dimensions.

These simulation results are expected to be more similar to real images generated from PR acquisition than typical simulations through multiple scatterers with a single bounce ray, and therefore could help to design a classification technique for identifying targets.

# Chapter 5

# DVB-T Array

In Chapter 1, it was studied the suitability of employing DVB-T signals in passive radars, which provides good capabilities for detecting and tracking targets. Chapter 3 detailed the technological passive radar demonstrator developed in the University of Alcalá in its version previous to this thesis. The acquisition chain is composed of 8 channels for the digitalization of external signals, one of which is reserved for the reference channel. This chapter presents the progress in one of the objectives of this thesis: the design and development of a linear array of 7 antennas for the surveillance channel of IDEPAR for exploiting DVB-T IoOs. The array system will provide a good solution of compromise between angular coverage, range coverage and angular resolution for 2D (range, azimuth) target localization and discrimination.

Results presented in this Chapter have been included in the paper entitled *Broadband modified-circle-shape patch antenna with H-aperture feeding for a passive radar array* published in Aerospace Science and Technology of Elsevier [149].

## 5.1 Array Geometry Study with commercial antennas

As preliminary work, the design and study of a commercial UHF antennas array have been carried out. The main characteristics for a linear array implementation of the considered single element, the *Televes 4G Nova* antenna (described in detail in Chapter 3), are summarized in Table 5.1.

| Antenna Size | Reduced Size | Bandwidth | Azimuth HPBW | Elevation HPBW |
|---|---|---|---|---|
| 315 mm | 210 mm | $[711 - 787]$ MHz | 60° | 90° |

Table 5.1: *Televes 4G Nova* main parameters for a linear array implementation: full size and reduced size (taking off radome and reflector) in the elements placing direction, operation bandwidth within DVB-T band and azimuth and elevation HPBW at 770 MHz.

A linear array allows azimuth discrimination, but a Uniform Linear Array (ULA) can

not fulfil the angular and range coverage requirements of the passive radar system with a big area of surveillance for monitoring low back-scattering targets. In this Chapter, a Non-Uniform Linear Array (NULA) solution is proposed to improve the radiation characteristics (directivity, SLL and grating lobes) against an ULA, by changing the separation between single elements.

This section presents an optimization method for designing a NULA and the corresponding study for checking the performance of ULA and NULA arrays of commercial antennas.

### 5.1.1   NULA Design Method

In order to study what is the best inter-element spacing for a NULA used in the proposed application, a first approach was proposed in [135]. This method employed a genetic algorithm [150] to optimize the SLL and array directivity of beams generated by a NULA of 5 single elements. Usually, a decrease in SLL is achieved by reducing the inter-element distances $d_i$ but it decreases the directivity, and, therefore the resolution of the system. The proposed method minimize the cost function defined in Equation 5.1 yielding to the best compromise solution for optimizing both, SLL and directivity, which are the keys for the PR performance, for different steering angles ($\mathbf{\Phi}_{sa}$) within the Area of Interest (AoI). The cost function is composed mainly by two terms: the first one controls the SLL by calculating the difference ($\ell_1$ norm) between the normalized radiation pattern and a specific value of side-lobe level ($SLL_{max}$) outside the main beam width ($\phi \notin BW_{3dB}$); the second controls the directivity across the HPBW ($BW_{3dB}$) multiplied by a $k$ factor.

$$\overline{C}_{SLL_{max},\mathbf{\Phi}_{sa}}(\mathbf{d}) = \frac{1}{N_{\Phi_{sa}}} \sum_{i=1}^{N_{\Phi_{sa}}} \left( \sum_{\substack{\phi \notin BW_{3dB_{\Phi_{sa,i}}} \\ |\bar{\mathbf{E}}_{\Phi_{sa,i}}(\phi,\mathbf{d})| > SLL_{max}}} \left| |\bar{\mathbf{E}}_{\Phi_{sa,i}}(\phi,\mathbf{d})| - SLL_{max} \right| + k \cdot BW_{3dB_{\Phi_{sa,i}}} \right)$$

$$(5.1)$$

- $\mathbf{d} = [d_1, d_2, \cdots d_{N-1}]$ is the inter-element distances vector ($\mathbf{d} \in \mathbb{R}^{N-1}$, for an array with N elements), optimized using a genetic algorithm;

- The cost function is averaged for N different steering angles ($N_{\Phi_{sa}}$) within the range of possible azimuth directions defined by single radiation element pattern: $\mathbf{\Phi}_{sa} = [\Phi_{sa,1}, \Phi_{sa,2}, ..., \Phi_{sa,N_{\Phi_{sa}}}]; \phi_{sa,i} \in [-\phi_{max}, \phi_{max}], i = 1, ...N_{\Phi_{sa}}$

- $|\bar{\mathbf{E}}_{\Phi_{sa,i}}(\phi,\mathbf{d})| = 20 \cdot \log_{10} \frac{|\mathbf{E}_{\Phi_{sa,i}}(\phi,\mathbf{d})|}{|\mathbf{E}_{\Phi_{sa,i}}(\phi,\mathbf{d})|_{max}}$ is the magnitude of the normalized radiation pattern of the array for steering angle $\Phi_{sa,i}$ expressed in decibels, particularized in the azimuth plane ($\theta = 90°$), for the considered distances vector $\mathbf{d}$. The radiation pattern of the array is calculated through array theory [125] including the radiation

pattern of the single element (Equation 2.20). Note that for the cost evaluation, only azimuth values outside the main beam, and with an associated radiation pattern magnitude higher than $SLL_{max}$ are considered in the summation, so secondary lobes and grating lobes inside the angular coverage are controlled to reduce their levels.

- $SLL_{max}$ is the specified maximum value of the Side Lobe Level in decibels. It is defined as the difference between the main beam level and the highest side lobe level

- $k$ is parameter that allows us to control the main beam width, $BW_{3dB}$. It has been adjusted experimentally.

- $BW_{3dB_{\Phi_{sa,i}}}(\mathbf{d})$ is the array HPBW in azimuth plane for the considered distances vector $\mathbf{d}$ for steering angle $\Phi_{sa,i}$.

A NULA of 5 *Televes 4G Nova* is designed at 770 MHz employing the proposed method. The maximum SLL value were defined to $SLL_{max} = 14$ dB, and the considered pointing directions $\mathbf{\Phi}_{sa} = \{-30°, -15°, 0°, 15°, 30°\}$. A constraint was applied to limit the minimum inter-element spacing to the size of the antenna $d_{min} = 210$ mm (without the radome and the reflector). A study in $k$ values were carried out, achieving the best results for $k = 1$. The final design was characterized by the following inter-element distances: $d_1 = 243$ mm, $d_2 = 210$ mm, $d_3 = 210$ mm and $d_4 = 243$ mm. Although $d_1 = d_4$, $d_2 = d_3$, this symmetry was not imposed in the optimization algorithm.

## 5.1.2   Linear Arrays Performance

The designed NULA was modelled and simulated in ANSYS HFSS to compare with ULA-based solutions. In [151], the performance of the NULA versus two ULAs, one with the minimum inter-element spacing $d_{ULA1} = 210$ mm (ULA$_{210}$) and one with the same total aperture than NULA $d_{ULA2} = \sum d_i / (N - 1) = 226.5$ mm (ULA$_{226.5}$), were compared. Figure 5.1 shows the comparison between the ULA$_{210}$ and the designed NULA, while the main parameters for the 3 designs are summarize in Table 5.2. It is proved how the NULA overcomes the performance in terms of SLL with respect to both ULAs while its directivity is equal than the ULA of same aperture length. In the maximum steering angles $\pm\Phi_{sa_{max}} = \pm30°$, the NULA design present grating lobes but their are not critical because its level (GLL) is less than SLL.

The study was extended to ULAs and NULAs with different number of elements $N = \{8, 11, 14\}$ probing the validity of the design method for other cases. The optimized inter-element distances for the optimized NULAs are:

- $\mathbf{d_8} = [297, 242, 210, 210, 210, 210, 254, 242]$

- $\mathbf{d_1}1 = [349, 259, 223, 210, 210210, 214, 235, 262, 231]$

- $\mathbf{d_1}4 = [373, 306, 258, 226, 210, 210, 210, 210, 210, 240, 250, 284, 214]$

(a) $\Phi_{sa} = 0°$                                    (b) $\Phi_{sa} = 30°$
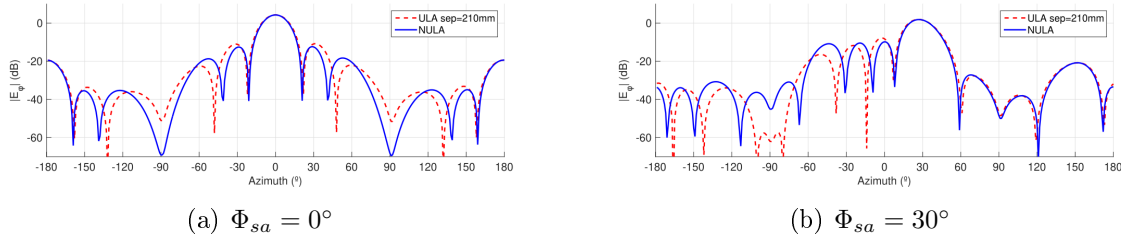
Figure 5.1: Comparison of designed NULA and ULA$_{210}$ azimuth radiation patterns for two steering directions: 0° (broadside) and 30° (limit of coverage).

Table 5.2: Main characteristics of designed NULA, ULA$_{210}$ and ULA$_{226.5}$ (HPBW, SLL, GLL and directivity).

| Angle | Array | HPBW | SLL(dB) | GLL(dB) | D(dBi) |
|-------|-------|------|---------|---------|--------|
| | ULA$_{210}$ | 20° | 9.43 | x | 12.73 |
| −30° | ULA$_{226.5}$ | 19° | 9.44 | x | 12.97 |
| | NULA | 19° | 12.01 | 12.18 | 12.90 |
| | ULA$_{210}$ | 19° | 12.12 | x | 12.86 |
| −15° | ULA$_{226.5}$ | 18° | 11.93 | x | 13.14 |
| | NULA | 18° | 13.94 | x | 13.13 |
| | ULA$_{210}$ | 18° | 15.06 | x | 12.93 |
| 0° | ULA$_{226.5}$ | 17° | 14.62 | x | 13.21 |
| | NULA | 17° | 16.62 | x | 13.20 |
| | ULA$_{210}$ | 19° | 12.29 | x | 12.88 |
| 15° | ULA$_{226.5}$ | 19° | 12.08 | x | 13.16 |
| | NULA | 18° | 14.09 | x | 13.15 |
| | ULA$_{210}$ | 20° | 9.68 | x | 12.72 |
| 30° | ULA$_{226.5}$ | 19° | 9.62 | x | 12.97 |
| | NULA | 19° | 11.66 | 12.67 | 12.90 |

Table 5.3 summarizes the main parameters of the radiation patterns for a pointing direction equal to $\Phi_{sa_{max}} = 30°$. As the number of elements increases, the improvement in SLL of the NULA with respect to the ULA-based solutions increases significantly. Only the NULA of 8 elements presents grating lobes, but, again, the GLL is less important than the SLL.

A further study was carried out to demonstrate how the size of the single element influences on array performance. A smaller antenna implies that inter-element spacing could be reduced. Following the design theory for log periodic antennas [152], the replacement of the *FR4* ($\varepsilon_r = 4.4$) substrate by *Rodgers 3010* ($\varepsilon_r = 10.2$), will allow reducing the antenna width up to 25%, being the new minimum inter-element spacing $d_{min} = 160$ mm. Using this value as a new lower limit for boundary conditions of genetic algorithm, new

Table 5.3: Main characteristics of NULA-based and ULA-based systems azimuth radiation patterns steering at $\phi_{sa} = 30°$ (HPBW, SLL, GLL and directivity) for $N = \{8, 11, 14\}$ elements.

| N | Array | HPBW | SLL(dB) | GLL(dB) | D(dBi) |
|---|-------|------|---------|---------|--------|
| | $ULA_{210}$ | 14° | 10.56 | x | 14.59 |
| 8 | $ULA_{237.9}$ | 12° | 10.67 | x | 15.05 |
| | NULA | 12° | 14.00 | 15.17 | 14.85 |
| | $ULA_{210}$ | 9° | 11.09 | x | 15.92 |
| 11 | $ULA_{240.3}$ | 9° | 11.27 | x | 16.42 |
| | NULA | 9° | 15.16 | x | 16.13 |
| | $ULA_{210}$ | 7° | 11.43 | x | 16.91 |
| 14 | $ULA_{246.2}$ | 6° | 11.70 | x | 17.54 |
| | NULA | 7° | 16.53 | x | 17.13 |

NULAs were designed. The results for NULA of commercial *4G Nova* ($NULA_{210}$) and the one modified with Rodgers substrate ($NULA_{160}$) are compared in Table 5.4.

It is demonstrated that in a NULA architecture, reducing single element size, SLL can be improved as far as 2.5 dB with respect to another NULA with minimum inter-element spacing 25% higher. It is also proved that the improvement becomes bigger as the number of elements increases till $N = 11$ elements, when it reaches an improvement of about 2.5 dB. For $N = 14$, SLL improvement is lower. On the other side, employing smaller elements implies that total array length decreases and it leads to a lower directivity.

Table 5.4: Main characteristics of $NULA_{210}$ nad $NULA_{160}$ azimuth radiation patterns for steering angle at $\phi_{sa} = 30°$ (HPBS, SLL, GLL and directivity) for $N = \{5, 8, 11, 14\}$ elements.

| N | Array | BW | SLL(dB) | GLL(dB) | D(dBi) |
|---|-------|-----|---------|---------|--------|
| 5 | $NULA_{210}$ | 19° | 11.66 | 12.67 | 12.90 |
| | $NULA_{160}$ | 23° | 13.17 | x | 12.27 |
| 8 | $NULA_{210}$ | 12° | 14.00 | 15.17 | 14.85 |
| | $NULA_{160}$ | 14° | 15.69 | x | 14.27 |
| 11 | $NULA_{210}$ | 9° | 15.16 | x | 16.13 |
| | $NULA_{160}$ | 11° | 17.62 | x | 15.49 |
| 14 | $NULA_{210}$ | 7° | 16.53 | x | 17.13 |
| | $NULA_{160}$ | 9° | 18.44 | x | 16.49 |

## 5.2   Single radiating element requirements

The first step before carrying out an antenna system design is studying and setting the requirements it must fulfil for the objective system or application. In this case, the requirements of the single radiating element are imposed by the passive radar application and by the fact that it is going to form part of an array.

The main requirements that the single radiating element must fulfil are the following:

- **Bandwidth**. The higher sub-band of DVB-T frequencies after the first digital dividend was selected. The acquisition bandwidth of the system is 100 MHz, so the antenna bandwidth should be at least the same, but it would be desirable to achieve impedance matching from 600 to 790 MHz, to allow more flexibility in any scenario for the selection of the best acquisition frequency sub-band: more number of DVB-T channels (MUX) or channels with better SNR. This is a demanding requirement as it will suppose 27% of relative bandwidth.

- **Beamwidth**. The single radiating element azimuth beamwidth defines the angular coverage of the radar system. In a general case, considering any possible scenario, it is desired to cover a surveillance area broad enough for being able to track targets during some seconds. For this reason, an azimuth beamwidth of at least 80° is required. In elevation case, terrestrial or maritime targets are usually located at a few degrees from the horizontal plane to the PR, but aerial ones can have big elevation angles: aeroplanes flight at high altitudes even they are expected to be far away from PR, and UAVs, that do not reach altitudes so high, are expected to be detected at less distance from the PR, so elevation angle could be also great. Currently, there is a growing interest in drone detection for security reasons [146]. According to current regulations, recreational drones could fly up to a maximum height of 120 $m$ for which an elevation beamwidth of 60° (+30° over the horizontal of the antennas) will allow the detection of drones at the highest altitude and 200 $m$ far from the PBR.

- **Size**. The array must not present limiting grating lobes within the desired pointing range. Representing the Array Factor (AF - Equation 5.2) versus the distance between elements (in ULA approximation), it is found that grating lobes appear, for the minimum and maximum frequency of the band, for $N = 7$ elements and the angular coverage ($\theta_d = \{-40°, +40°\}$), at distances $d_{600MHz} = 0.691\lambda$ and $d_{790MHz} = 0.525\lambda$ (figure 5.2). It is considered that a grating lobe appears when it limits the performance of the array, and this happens when its level is greater than the SLL, so this points is taken for estimating the maximum distance between elements. Therefore, the maximum size of each single radiating element in the direction of the linear array, in the worst case (higher frequency) is 200 mm.

$$|AF| = \frac{sin\left[kNd\left(cos\theta_d - cos\theta\right)/2\right]}{sin\left[kd\left(cos\theta_d - cos\theta\right)/2\right]} \tag{5.2}$$

(a) 600 MHz

(b) 790 MHz
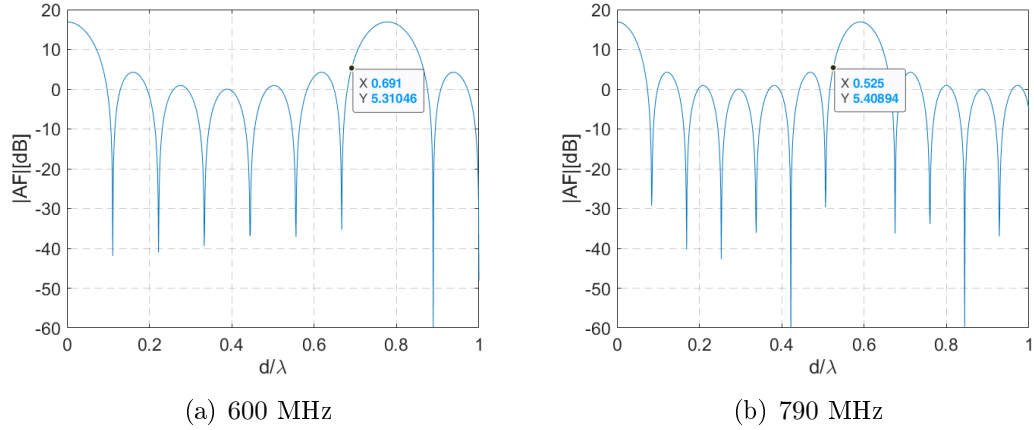
Figure 5.2: Array Factor for $N = 7$ elements and steering direction $\theta_d = 40°$ for the lowest and highest frequencies of the band. The first grating lobe appears at $d = 0.691\lambda$ and $d = 0.525\lambda$ respectively.

- **Polarization**. In Europe, DVB-T signal can be even horizontally or vertically polarized. In Spain, it is only horizontally polarized, so more emphasis will be done on the design of an array for this polarization, even a design of an antenna suitable for an array in vertical polarization will also be considered.

- **Gain**. In Section 4.2, it was proved that with an antenna system of 14.5 dBi, that is the equivalent of a 7 elements ULA of antennas of 6 dBi gain, large coverages can be achieved: around 4 km for small terrestrial targets in the scenario of the external campus of the University of Alcalá; at least 8 km for medium size maritime targets in Cádiz; and about 1 to 1.5 km in the proposed aerial scenarios for small UAVs (Figure 4.5). As a result, the minimum single radiating element gain is fixed to 6 dBi.

- **Front-to-Back Ratio (FB)**. This parameter measures the ratio (in natural units) between the level of the front-side lobe and the back-side lobe of the antenna. Usually, bistatic geometry is selected in such a way that the DPI arrives through the back of the surveillance antennas, so a high FB could improve performance. As radar scenario can vary from one emplacement to another, this requirement is considered less restrictive, and it will be maximized after fulfilling the previous ones.

# 5.3   Design of an antenna for vertical polarized array

This section presents the design of an E-shape patch antenna suitable for inclusion in array with vertical polarization that will be useful for PR trials in different countries of Europe. The prototype was measured in an anechoic chamber and it was validated as a single antenna for the surveillance channel of IDEPAR demonstrator.

## 5.3.1   E-patch Antenna Design

The design of an antenna that fulfils the demanding requirements such as the defined in Section 5.2 implies a wide study of literature, for merging techniques that improve different parameters and even the proposal of new techniques. The methodology that was carried out to design the antenna is the following:

1. Selection of the patch geometry and feeding method.

2. Study and application of different techniques for bandwidth enhancement to fulfil requirements.

3. Optimization of main parameters.

4. Radiation pattern improvement techniques.

5. Requirements assessment.

The proposed antenna [153] employs an E-shaped patch, which presents greater bandwidth than a simple rectangular one, fed with coaxial probe technique at position $(X_f, Y_f)$. The E-patch was built in an $FR4$ board employing inverted patch technique to improve antenna gain and also to protect the patch from the external environment, as the antenna will work outsides. Besides E-patch, for achieving the required bandwidth, a thick air substrate between the patch and the ground plane was employed. A scheme of the antenna and its main parameters are shown in Figure 5.3, where the different layers that compound it are from bottom to top: ground plane, air substrate, patch and $FR4$ inverted substrate. The main parameters of the antenna were optimized to achieve the best performance in terms of bandwidth and gain, being the final values the ones showed in Table 5.5.

Finally, a study of different reflectors (Figure 5.4) were done to improve Front-to-Back ratio without success, so a novel technique based on wrapping the air substrate with a copper extension of the ground plane was proposed (Figure 5.5(d)). It was called *boxed ground* and it improves the FB ratio in 3 dB: front gain is enhanced in 0.7 dB and back radiation is decreased in 2.4 dB (Figure 5.5). The final antenna size is $30 \times 20 \times 4.16$ mm, being suitable for inclusion in an vertical polarization array (antenna polarization follows the direction of Y axis).
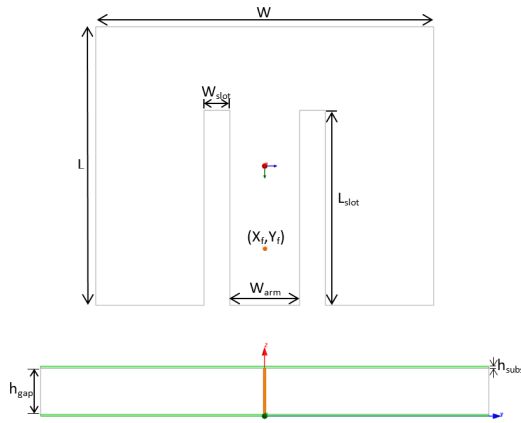
Figure 5.3: E-shaped antenna schematic: top and sideways view.

Table 5.5: Optimized parameters of E-shape antenna.

| Parameter | Value [mm] |
|:---:|:---:|
| W | 170 |
| L | 140 |
| $W_{slot}$ | 13 |
| $L_{slot}$ | 98 |
| $W_{arm}$ | 35 |
| $(X_f, Y_f)$ | (41,0) |
| $h_{gap}$ | 40 |
| $h_{subs}$ | 1.5748 |

(a) Plane          (b) Pyramidal

(c) Parabolic          (d) Boxed gnd
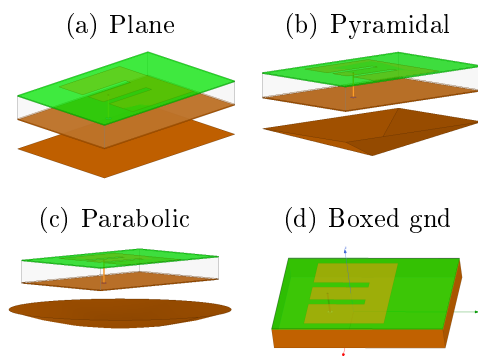


Figure 5.4: Different reflectors and boxed ground antenna design.
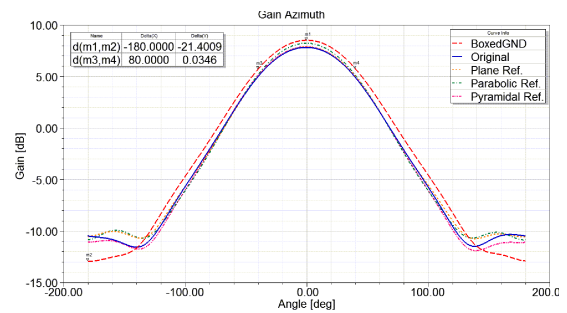


Figure 5.5: Azimuth gain pattern comparison between different reflectors and boxed ground technique at 740 MHz.

### 5.3.2   Prototype characterization

A prototype of the designed antenna was manufactured and measured in the semi-anechoic chamber, with the floor covered with absorbent, of High Technology and Homologation Centre, CATECHOM, of the University of Alcalá (Figure 5.6).

Results show good agreement between simulations and measurements, with some differences in reflection coefficient, probably due to imperfections during the manufacturing process of the prototype. The antenna is matched ($|S_{11}| \leq -10$ dB) between 650 MHz and 800 MHz. The maximum gain at 740 MHz is 6.7 dBi while the beam-widths in azimuth and elevation are 84° and 56° respectively.



(a) Prototype                        (b) $S_{11}$                        (c) Radiation patterns
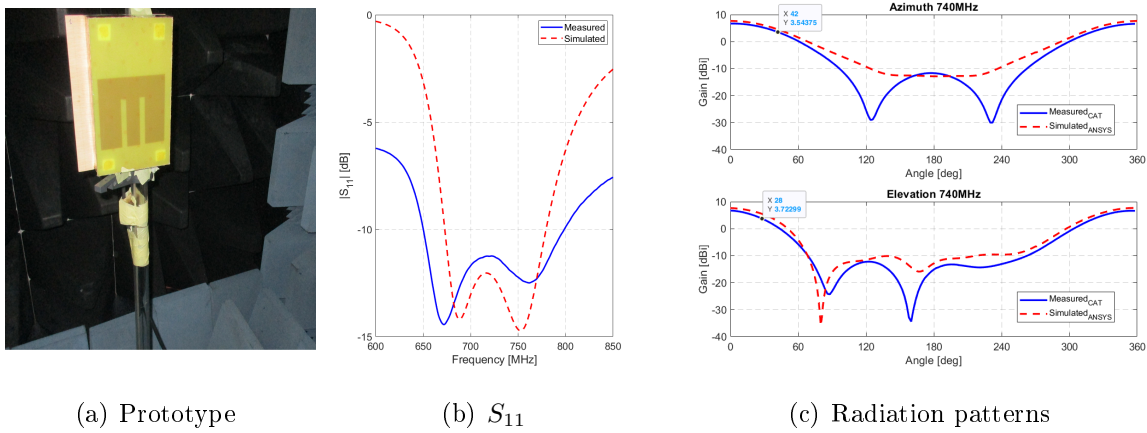
Figure 5.6: Prototype positioned inside semi-anechoic chamber for measurements and results comparing measured and simulated $S_{11}$ and azimuth and elevation radiation patterns at 740 MHz.

### 5.3.3   Validation in PR trials

To validate the prototype, PR trials were carried out the $15^{th}$ of February 2017 at the roof of Superior Polytechnic School of University of Alcalá. The prototype was rotated 90° for achieving horizontal polarization to correctly acquire DVB-T signals (Figure 5.7(a)). Antenna in this orientation could not be included in an array because its size would limit the minimum inter-element spacing causing the appearance of grating lobes.

Each acquisition of 20 s with IDEPAR demonstrator is processed calculating CAF with ECA filtering to intervals of $CPI = 250$ ms, achieving 80 RD maps. A CA-CFAR detector in range dimension ($N_r = 32$, $N_g = 5$) for $P_{fa} = 10^{-5}$ is applied to each of the RD maps, and after this, a tracker based on Kalman filtering is employed to associate the set of detections in tracks of the same target. Figure 5.7(b) shows the RD map at the output of the CAF for one of the CPIs and Figure 5.7(c) the cumulative of detections and the tracks associated with them.

(a) Prototype
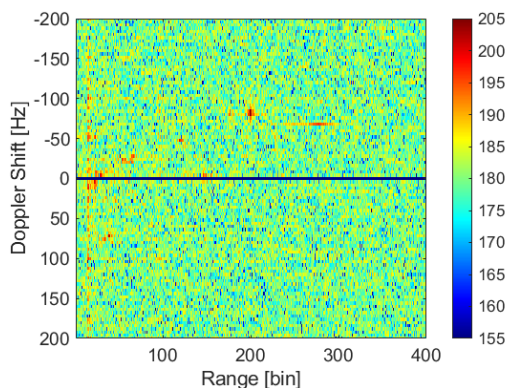


(b) RD map CPI$_{30}$
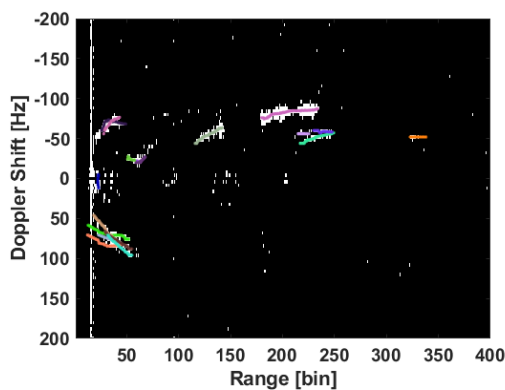


(c) Cumulative detections and tracks

Figure 5.7: Prototype rotated 90° for trials, RD map of CPI 30 and cumulative detections with the 13 tracks provided by the tracker.

## 5.4 Design of an antenna for horizontal polarized array

A similar methodology, based on merging different MSA design techniques, and the same design steps explained in Section 5.3, was applied to design an antenna suitable for array in horizontal polarization. The array composed of single radiating elements designed in this section will be the most employed surveillance antenna system of IDEPAR demonstrator, because trials campaigns will mainly take place in Spain, so more effort was put into achieving a greater bandwidth. In this way, a first prototype was manufactured on which minor changes were applied to improve performance before the array was built up.

(a) Plane Reflector        (b) Pyramidal Reflector        (c) Boxed Reflector
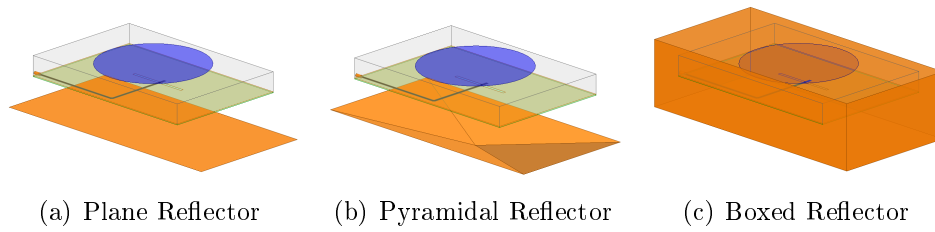
Figure 5.8: Different shapes reflectors studied for FB ratio and azimuth beamwidth improvement.

## 5.4.1   Circular Patch Antenna Design

This antenna presents some similarities with the E-patch one: a thick air substrate, that is a key point for achieving a wide bandwidth, and a boxed reflector similar to the proposed boxed ground for achieving radiation requirements. The main differences are the patch shape and feeding technique. The selected patch shape is circular, as it presents a more efficient ratio between operation frequency and size [154]. Feeding is applied through aperture coupling which is a more appropriate technique for thick substrates and boosts the bandwidth.

A study of different shape reflectors was carried out (Figure 5.8) probing that, with respect to a circle patch antenna with thick air substrate and aperture feeding, a plane or a pyramidal reflector improves the FB ratio up to 22 dB but, in both cases, the azimuth beamwidth is below the required 80° (Figure 5.9). Having in mind the good performance of *boxed ground*, a reflector based on it was also studied: it provides less FBR than the previous one (16 dB) but it fulfils beam-widths requirements, and besides that, it achieves a flatter main beam pattern with less SLL which is expected to benefit the array performance [149], so this reflector is selected. The size of the antenna was limited to 20 cm in the dimension along azimuth (Section 5.2). The size along the elevation plane is not limited and it must be higher than along the azimuth one to achieve a greater beamwidth in azimuth, so the reflectors sizes are defined to be $40 \times 20$ cm$^2$. For achieving horizontal polarization, the feeding line must enter into the patch along the azimuth axis, the same one where linear array elements will be located, so an L-shape microstrip line is proposed in order not to obstruct the connector with the rest of array elements.

The antenna with boxed reflector shows potential for great wide bandwidth but it is not well matched. If the basic aperture slot is replaced by an H-shape slot, impedance matching is improved achieving a relative bandwidth of 30%, extending over a frequency band of more than 200 MHz (Figure 5.11(a)). The physical parameters of the H-shape slot were selected through gradient optimization to minimize $|S_{11}|$ in the desired DVB-T frequency band (Figure 5.10(a)). Finally, a substrate was added on top of the patch to provide protection against environmental elements and simplify the manufacture of the antenna. This technique, called inverse substrate, in combination with a slot in oneside of the patch ($W_{slot} = 40$ mm; $L_{slot} = 45$ mm), allowed to improve matching, dropping $|S_{11}|$

(a) Azimuth
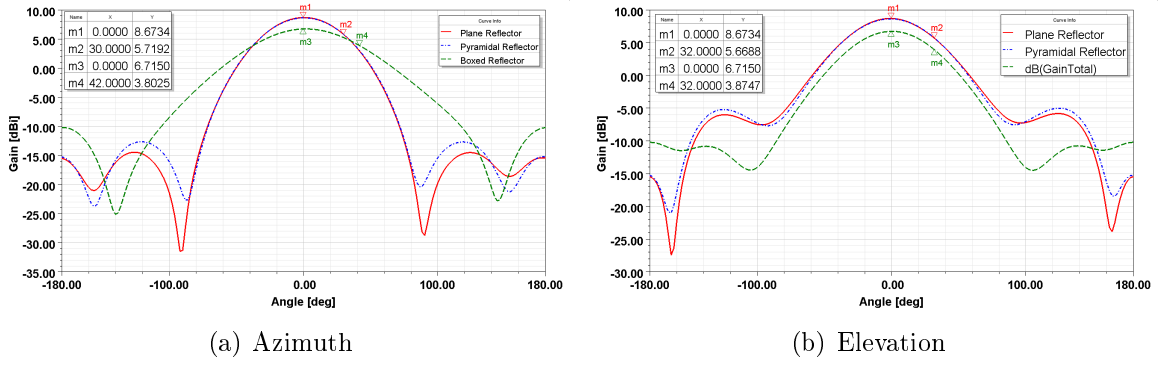
(b) Elevation

Figure 5.9: Gain pattern in azimuth and elevation planes of the antenna with different shape reflectors at 790 MHz.



(a) H-aperture scheme

(b) Final design
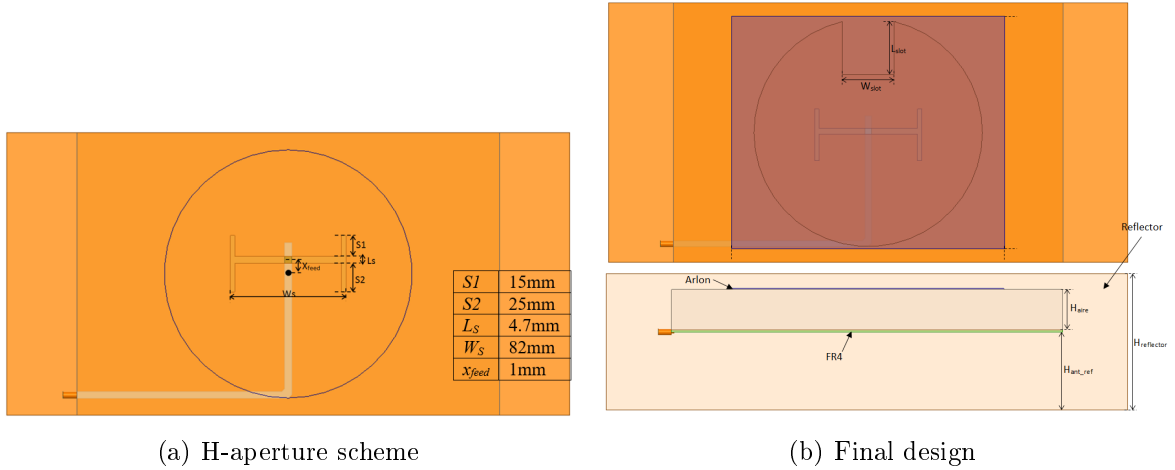
Figure 5.10: H-aperture scheme with the optimized values of its parameters and final antenna top and sideways schemes.

below $-14$ dB from 589 MHz to 795 MHz ([562 − 806] at $|S_{11}| = -10$ dB, 35.6% of relative bandwidth, Figure 5.11(a)), leaving a 4 dB margin for manufacturing deterioration. The substrate employed was Arlon CuClad 250GT of 0.9 mm of thickness, because it has a low dielectric constant ($\varepsilon_r = 2.5$). With these last retouches the final design of the antenna, shown in Figure 5.10(b), fulfils all requirements. From here on, this antenna will be referred as C-H$_a$, from its **C**ircular patch with **H**-shape **a**perture. As the bandwidth was higher, spreading towards lower frequencies where more DVB-T Muxs were expected, C-H$_a$ antenna provides more robustness with respect to the availability of DVB-T channels. The radiation pattern shows that azimuth and elevation beamwidths fulfil the required values (82° and 64°), with a gain and FB ratio of 7.45 dBi and 16.8 dB, respectively, (Figure 5.11(b)).
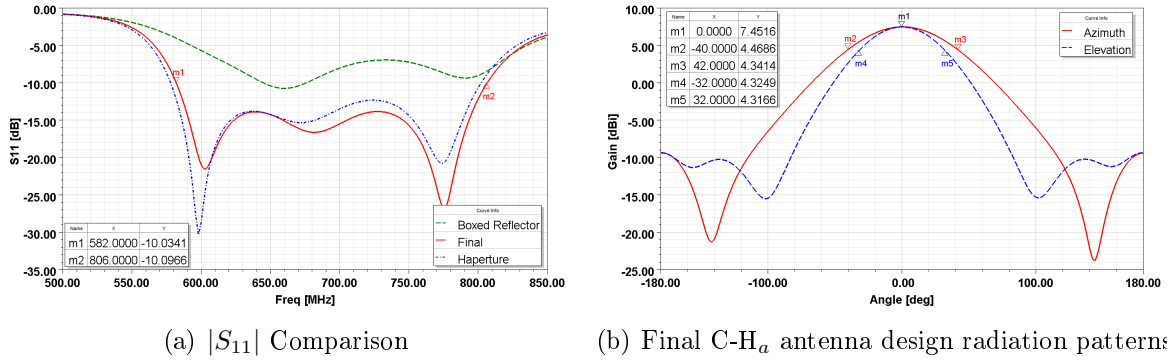
(a) $|S_{11}|$ Comparison



(b) Final C-H$_a$ antenna design radiation patterns

Figure 5.11: Reflection coefficient of antenna with boxed reflector, after applying H-aperture slot and final version. Azimuth and elevation radiation patterns of final antenna design at 790 MHz.

### 5.4.2 Prototype characterization

A prototype of the designed antenna was manufactured and measured in the anechoic chamber of the CATECHOM, of the University of Alcalá (Figure 5.12(a)).

Measured $|S_{11}|$ is shown in figure 5.12(b) verifying that the relative bandwidth is 31.8%, for $|S_{11}| < -10$ dB, which surpassed the requirements providing to the PR system the possibility of selection of the frequency band that contains more DVB-T channels in each placement, improving system capabilities.

The radiation pattern was measured in the front hemisphere, because of the positioning system blocking effect. Azimuth and elevation beamwidths were a bit wider than simulated ones (90° in azimuth and 70° in elevation), and gain was slightly reduced to a maximum of 6.5 dBi (Figure 5.12(c)). The maximum gain as a function of operation frequency, for simulated and measured case, is shown in Figure 5.12(d)

## 5.5 C-H$_a$ antenna NULA design

This section presents the design of a 7-element NULA using the single radiating elements designed in Section 5.4 (Figure 5.13). The optimization algorithm described in Section 5.1.1 was revisited and completed including coupling effects between elements.

### 5.5.1 Coupling effects modelling and inclusion in the optimization process

Due to the wide variety of possible architectures, real radiation patterns of the elements in the array were approximated through simulations using ANSYS HFSS. Two ULAs were generated with inter-element distances $d_{ULA_1} = 201$ mm and $d_{ULA_2} = 240$ mm ($\sim 0.5\lambda$

(a) Prototype assembled into anechoic chamber
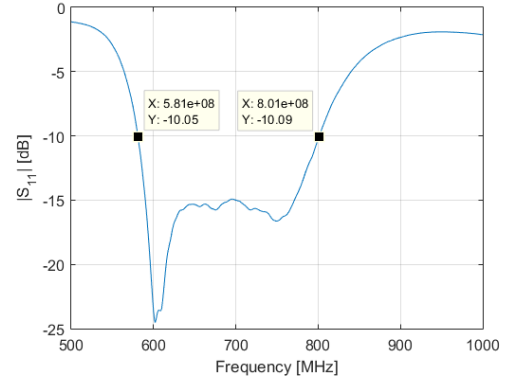


(b) Measured $|S_{11}|$
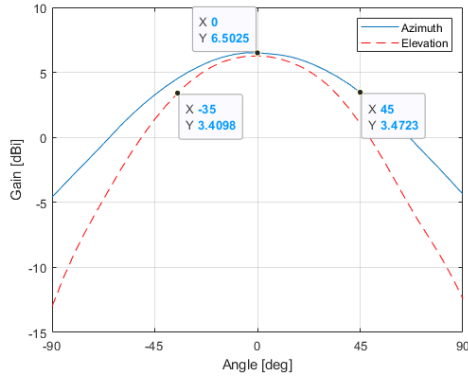


(c) Azimuth and elevation patterns
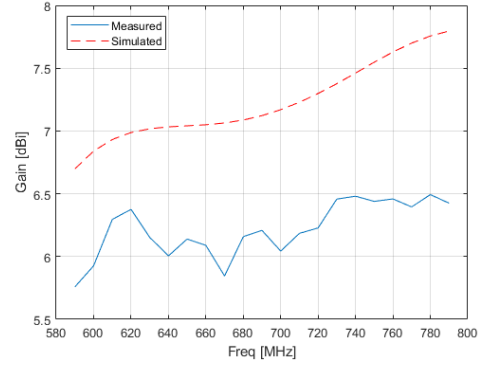


(d) Maximum gain

Figure 5.12: Results of prototype measurements in anechoic chamber of CATECHOM.
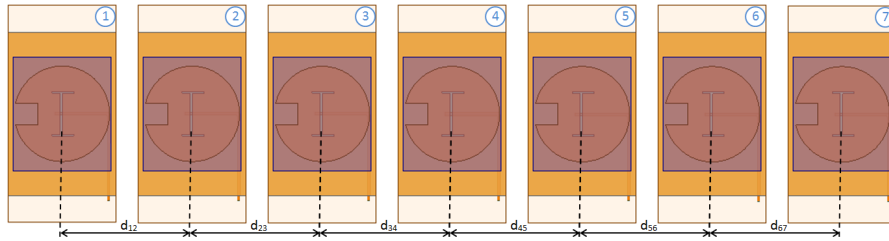


Figure 5.13: 7-elements NULA with inter-element spacing $\mathbf{d} = \{d_{12}, d_{23}, d_{34}, d_{45}, d_{56}, d_{67}\}$.

and $\sim 0.6\lambda$, respectively, at 740 MHz). In both cases, non-ending elements had very similar radiation patterns, but different from the ending ones (Figure 5.14).

These results were used for reducing computation complexity in the optimization of inter-element distances. The simulated central element $E_{sim_C}$ radiation pattern was used for the rest of non-ending elements, considering the distances to their neighbours; simulated radiation patterns of the ending elements $E_{sim_E}$ were preserved, taking into consideration the different distances to their neighbours.

(a) ULA $d = 201$ mm                              (b) ULA $d = 240$ mm
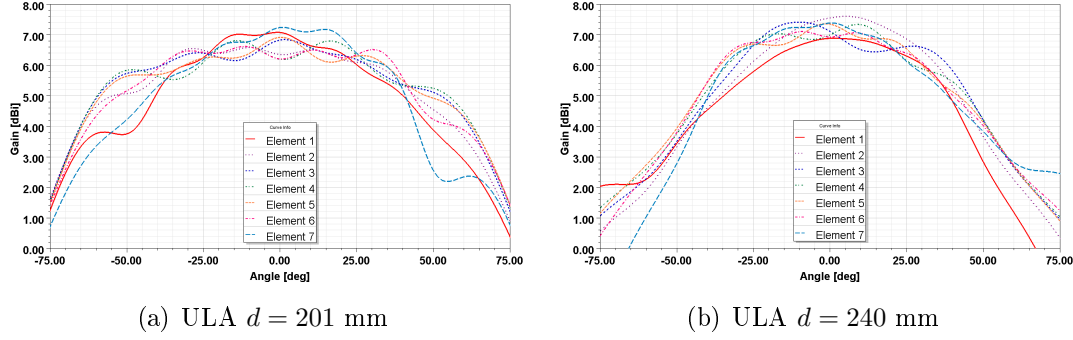
Figure 5.14: Comparison of single elements azimuth patterns for an ULA, including electromagnetic coupling effects.

An optimization method based on the one presented in Section 5.1.1 was employed. The algorithm employed to minimize the cost function is a direct search method called *General Pattern Search* (Equation 5.3). The distances search space $\mathbf{d}_{search}$ is defined by the interval $[d_{min}, d_{max}]$. The optimization algorithm sets off from an initial point (initial solution), takes different points surrounding the actual one, and evaluates the associated cost function values. The point with the lowest associated cost is selected as the starting one for the next iteration. The algorithm will stop when no cost reduction is achieved [155].

$$\min \bar{C}_{\mathbf{\Phi}_{sa}}(\mathbf{d})$$
$$\mathbf{d} \in \mathbf{d}_{search} \tag{5.3}$$

For a NULA design, the maximum distance between elements $d_{max}$ could be greater than the one studied for a ULA to avoid grating lobes, because the design optimization process will allow to avoid them. The minimum distance $d_{min} = 201$ mm is defined by the size of single element and $d_{max}$ is fixed to 279 mm ($\approx 0.69\lambda$).

In order to include the coupling effects between elements in the NULA design process, a set of $N_d$ distances in the interval $[d_{min}, d_{max}]$, with a uniform separation of $\Delta_d$, was used to define the simulation grid, $\mathbf{d}_{simulation}$. The radiation pattern of each element with its neighbours located at the distances within $\mathbf{d}_{simulation}$ must be carried out. As the optimization process employs a search space while simulated patterns are only available in a grid, in each iteration of the optimization process and for each element, the simulated radiation pattern for neighbours' distances nearest to the optimized one is employed (Equation 5.4).

$$E_m = E_{sim_C}\left(d_{sim_{Left}} \simeq d_{search_{m-1,m}}, d_{sim_{Right}} \simeq d_{search_{m,m+1}}\right) \quad m = 2, 3, ..., M-1$$
$$E_m = E_{sim_{EL}}\left(d_{sim_{Right}} \simeq d_{search_{m,m+1}}\right) \quad m = 1$$
$$E_m = E_{sim_{ER}}\left(d_{sim_{Left}} \simeq d_{search_{m-1,m}}\right) \quad m = M \tag{5.4}$$

Table 5.6 summarizes the number of simulations required for generating the single elements' radiation patterns to be used by the direct search method. Results reveal a significant reduction in computational burden associated with the simplified approach based on the use of the central element radiation pattern for the rest of non-ending elements of the array, and preserving the simulated radiation fields generated for the edge elements.

Table 5.6: Number of simulations needed as a function of the number of possible distances between elements ($N_d$) for complete and simplified methods.

| Method | $N_d = 3$ $\Delta d \approx 0.08\lambda$ | $N_d = 5$ $\Delta d \approx 0.04\lambda$ | $N_d = 7$ $\Delta d \approx 0.025\lambda$ | $N_d = 9$ $\Delta d \approx 0.021\lambda$ |
|---|---|---|---|---|
| Complete | $3^6 = 729$ | $5^6 = 15625$ | $7^6 = 117649$ | $9^6 = 531441$ |
| Simplified | $3^2 + 2 \cdot 3 = 15$ | $5^2 + 2 \cdot 5 = 35$ | $7^2 + 2 \cdot 7 = 63$ | $9^2 + 2 \cdot 9 = 99$ |

### 5.5.2 Design results

Four different designs were performed at same frequency (740 MHz) to analyse the improvements associated with the proposed C-H$_a$ single radiating element (Section 5.4) and the modification of the NULA design method including coupling effects controlling the associated computational cost (Section 5.5.1):

- $NULA_{4G}$: composed of 7 commercial antennas *Televes 4G Nova* [156]. The method described in Section 5.1.1 was applied to estimate the inter-element spacing that optimize performance resulting in
  $\mathbf{d} = [250.1, 215.2, 210, 210, 215.2, 250.1]$ mm. Figure 5.15(a) shows the array radiation pattern for the set of steering angles $\Phi_{sa}$ and the first column of Table 5.7 summarizes its main parameters.

- $NULA_{w/oCE}$: composed of 7 *C-H$_a$ Antennas* (Section 5.4) with inter-element distance calculated following the method described in Section 5.1.1, that is, without including coupling effects between elements in the optimization process. The radiation pattern employed for every single radiating element of the NULA, is the one simulated for the central element of an ULA with minimum inter-element distance $d_{min} = 201$ mm. The optimized inter-element spacings are: $\mathbf{d} = [241, 210.9, 201, 201, 232, 208.3]$ mm. Its simulation results are shown in Figure 5.15(b) and summarized in the second column of Table 5.7.

- $NULA_{wCE}$: composed of 7 *C-H$_a$ Antennas* with inter-element distance calculated following the improved method including coupling effects between elements in the

(a) $NULA_{4G}$



(b) $NULA_{w/oCE}$



(c) $NULA_{wCE}$



(d) $ULA_{\overline{\mathbf{d}}}$
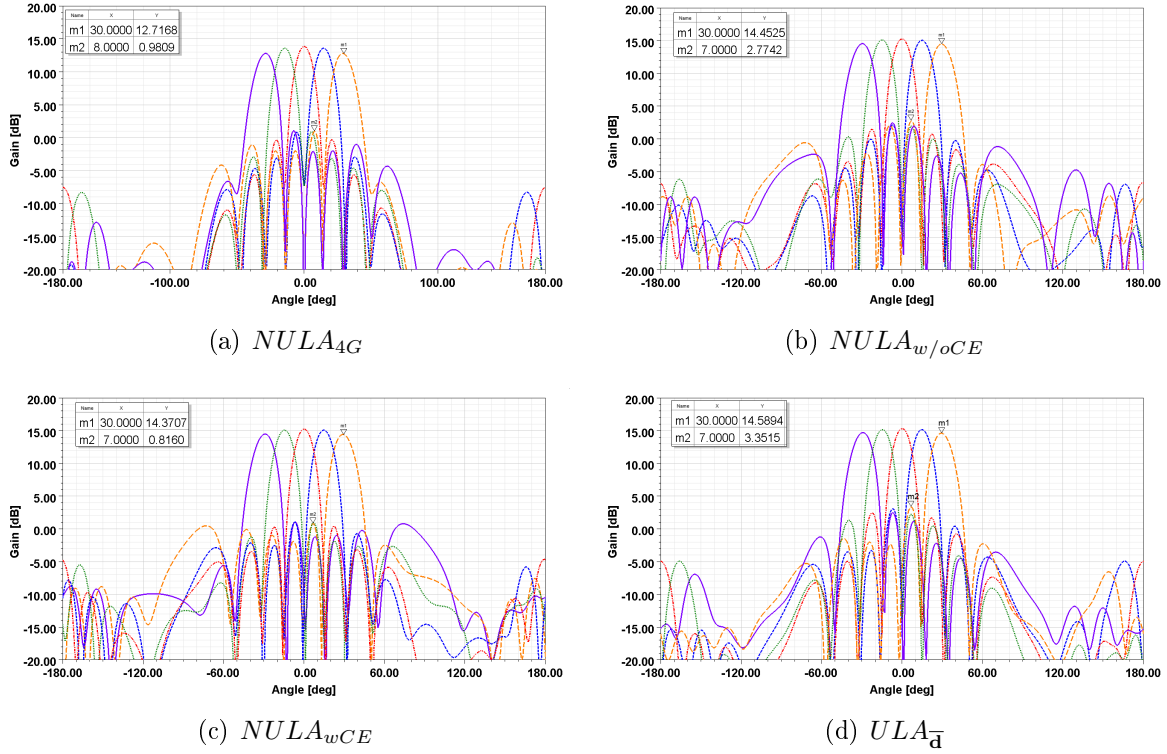
Figure 5.15: Simulated azimuth radiation pattern of the different arrays designed for results analysis.

optimization process employing the simplification to reduce computational cost (Section 5.5.1). Optimized inter-element distances are $\mathbf{d} = [229.4, 219.6, 201, 201, 201, 255]$ mm. The array radiation pattern is shown in Figure 5.15(c) and its main parameters are sumamrized in the third column of Table 5.7.

- $ULA_{\overline{\mathbf{d}}}$: An ULA with proposed C-$H_a$ antennas, of the same aperture length than $NULA_{wCE}$, that is, with the uniform inter-element distance equals to the mean of distances of $NULA_{wCE}$, was analyzed for comparison purposes. Results are showed in Figure 5.15(d) and in the last column of Table 5.7).

These results proved the importance of designing a radiating element appropriate for array and including the coupling effects between elements in the NULA design process. The main conclusions of this study are the following:

- Comparing the NULAs without coupling effects of *4G Nova antennas* and *C-$H_a$ antennas* it is proved that the proposed antenna improves the array gain in 1.5 dB achieving the same level of SLL in the worst case.

- If the radiation pattern employed for each element during the optimization process, to estimate the array pattern, has into account coupling effects with the rest of

Table 5.7: Main parameters of the different arrays at $f = 740$ MHz.

| Parameter | $NULA_{4G}$ | $NULA_{w/oCE}$ | $NULA_{wCE}$ | $ULA_{\overline{\mathbf{d}}}$ |
|---|---|---|---|---|
| $G_{\Phi_{sa}=0°}$ | 13.8 dBi | 15.2 dBi | 15.2 dBi | 15.3 dBi |
| $BW_{3dB\_\Phi_{sa}=0°}$ | 12.7° | 13.6° | 13.6° | 13.3° |
| $SLL_{\Phi_{sa}=0°}$ | 14.1 dB | 13.8 dB | 14.9 dB | 12.9 dB |
| $G_{\Phi_{sa}=\pm30°}$ | 12.7 dBi | 14.4 dBi | 14.4 dBi | 14.6 dBi |
| $BW_{3dB\_\Phi_{sa}=\pm30°}$ | 14.9° | 15.5° | 15.5° | 15.5° |
| $SLL_{\Phi_{sa}=\pm30°}$ | 11.7 dB | 11.7 dB | 13.6 dB | 11.2 dB |



(a) Semi-urban

(b) Maritime

(c) Rural 1

(d) Rural 2
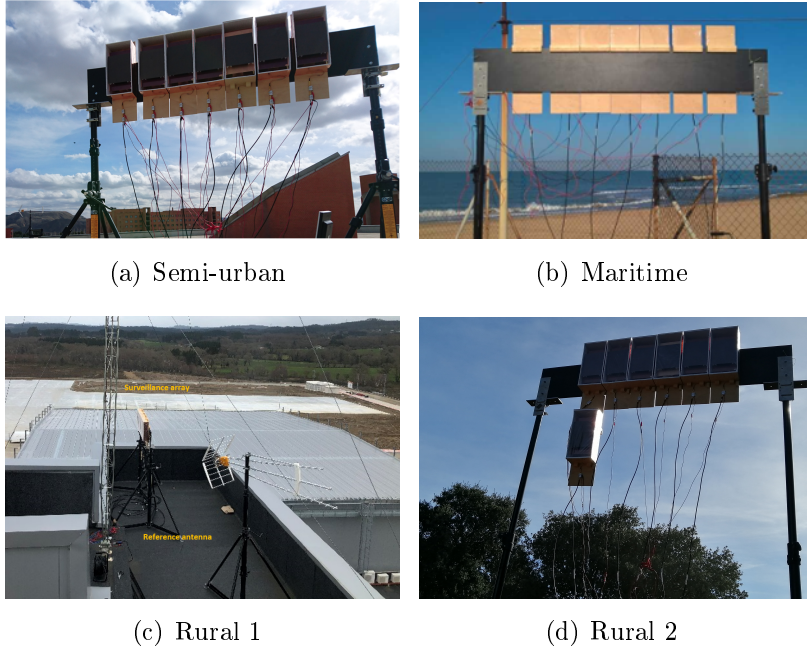
Figure 5.16: Images of the array deployment in the trials scenarios.

elements the designed NULA improves the performance in terms of SLL in almost 2 dB in the worst case ($\Phi_{sa} = \pm30°$).

- As it was proved in Section 5.1.2 NULA designs outperform the ULA in terms of SLL. If total aperture length of the array is the same (the case of $NULA_{wCE}$ and $ULA_{\overline{\mathbf{d}}}$), the gain and beamwidth are similar for uniform and non-uniform cases with the same elements.

### 5.5.3 Validation in PR trials

The designed antennas array has been employed for passive radar trials in the scenarios described in Section 3.4 (Figure 5.16).

**Trials in semi-urban scenario**

The scenario in the top roof of Superior Polytechnic School is the main scenario for trials with IDEPAR demonstrator, so many trials campaigns has been done in it. Some of the most representatives are the following:

- During the trials carried out the $7^{th}$ of March of 2019, the one acquired at 12:38:42 at 770 MHz is of special interest because, besides various terrestrial targets were moving along the roads, a plane flew over the surveillance area in its approaching to Torrejón Air Base. It seemed to be a *Falcon 900* or a similar size plane. The acquired 20 s were processed into 80 coherent processing intervals of $T_{int} = 250$ ms each one, following the two-stage method described in [135]. Cumulative detections after a CA-CFAR along range dimension was applied, as well as their associated tracks after tracker stage are shown in Figure 5.17(a). The output of the second stage, in which a DoA is applied to valid tracks is represented over Google Earth (GE) in Figure 5.17(b). Terrestrial targets were detected in both roads and the plane at around 6 km from the PR. The array performance was validated with the correct angle estimation of terrestrial targets, which allows to position them correctly in the roads.



(a) Cumulative detections and tracks



(b) GE tracks representation after DoA stage
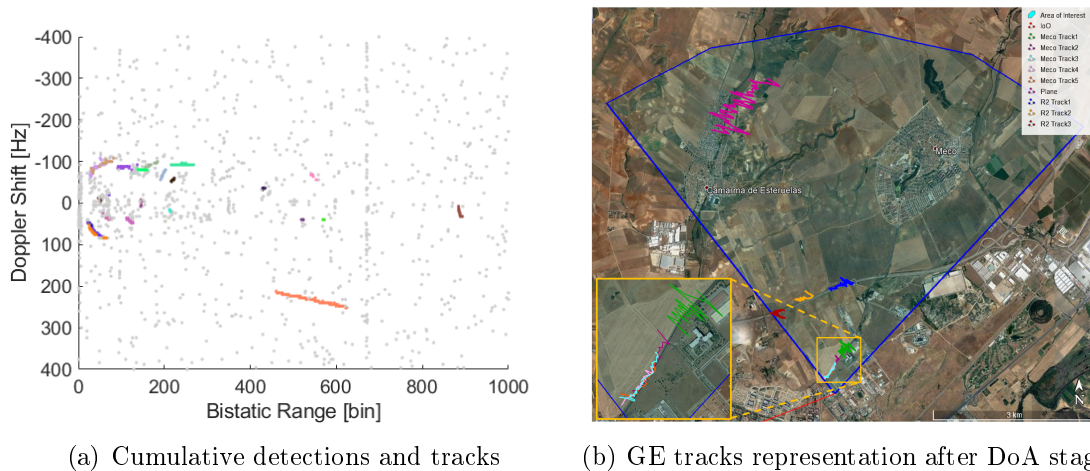
Figure 5.17: Results of trials in semi-urban scenario.

- The $29^{th}$ of October of 2020 some trials were made changing the area of interest to detect targets moving along A-2 highway. The main problem of this scenario is that all the buildings from the campus are between the passive radar and the targets. 20 s were acquired at 570 MHz and processed into 80 coherent processing intervals of $T_{int} = 250$ ms each one. Results prove that the designed NULA of $C\text{-}H_a$ *antennas* allows the detection and tracking of terrestrial targets at almost 5 km away from the PR (Figure 5.18). In this case, as there are several targets in the scenario, a

filtering stage has been applied to resulting angles of arrival providing a smoother trajectories image.



(a) Cumulative detections and tracks



(b) GE tracks after DoA stage
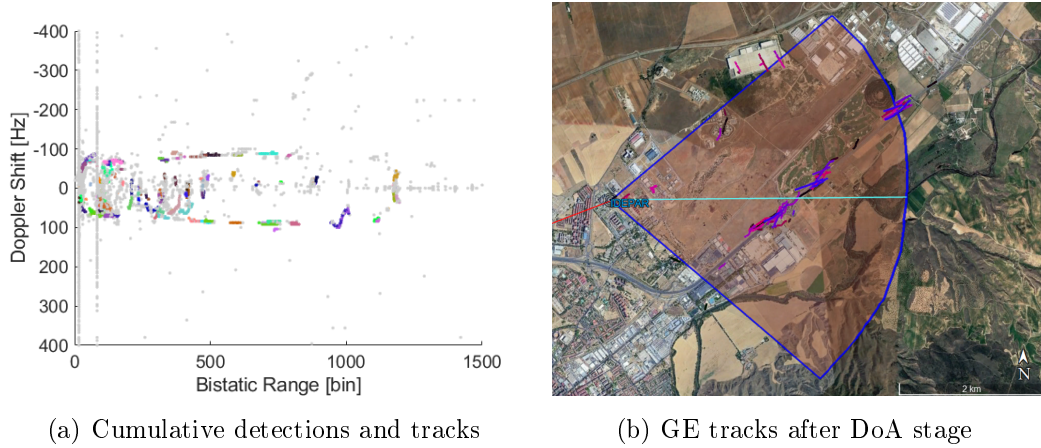
Figure 5.18: Results of trials in semi-urban scenario.

- The $3^{rd}$ of December of 2020 a military A400M flew over the surveillance area, and its ADSB data (ID:AME3152) was acquired at the same time as radar measurement at 570 MHz was carried out. Figure 5.19 shows the results proving that the aerial targets, as well as the replicas due to the turboprop engines, are detected at ranges around 1200, coinciding their tracks (magenta and pink) with the ground truth ADSB (white) at more than 9km far from the PR. It can be appreciated that one of the replicas due to propellers is not associated as a valid track, because it does not fulfil target kinematics conditions, that is, its change in range does not match with its Doppler velocity. That day, the position of the PR was in the other corner of the roof, so the own Superior Polytechnic School building covers part of the AoI, making that some tracks are received from multipath in it, giving as angle of arrival the one of the border of the building as it can be seen in the GE results (green line).

**Trials in Maritime scenario**

A trials campaign was carried out in the base of the $11^{th}$ Aircraft Squadron of the Spanish Navy in Cádiz during March of 2019. It was a great test for validating the designed array in a maritime scenario, which clutter could limit the system performance.

The acquisition presented here was realized to prove the array angle estimation performance with a controlled small drone (Phantom 3) flying over sea clutter, that is over the waves breaking on the seashore. During the acquisition time, a ship was also aproaching to Cádiz port and a plane to Rota airport. Figure 5.20(a) shows the cumulative detections during the 40s of the acquisition at 774 MHz, processed with $T_{int} = 500$ ms but generating a new CAF each 250 ms, with overlapping. In the same figure, the GPS data of the controlled drone is represented in red trace and the output of the tracer for ship

(a) Cumulative detections and tracks



(b) GE tracks after DoA stage
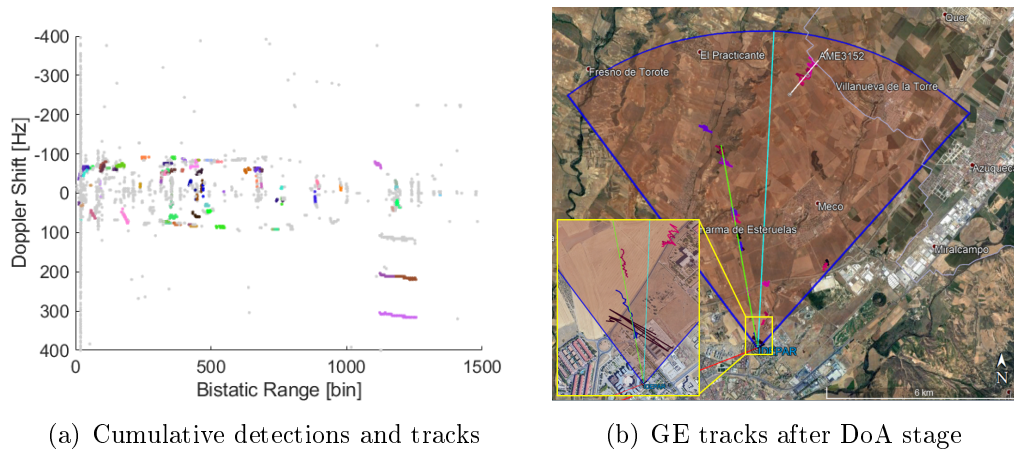
Figure 5.19: Results of trials in semi-urban scenario.

and plane detections in purple and green, respectively. The ship is at a distance of around 11 km from the PR and the plane is located 27 km far from the system. It can also be observed three areas of several detections coinciding in bistatic ranges of the three wind farm areas (marked in yellow). In Figure 5.20(b), the three targets tracks after angle estimation are represented: pink for the drone with its GPS ground truth in cyan, purple for the ship and green for the plane.



(a) Cumulative detections, controlled GPS and target tracks



(b) GE tracks after DoA stage
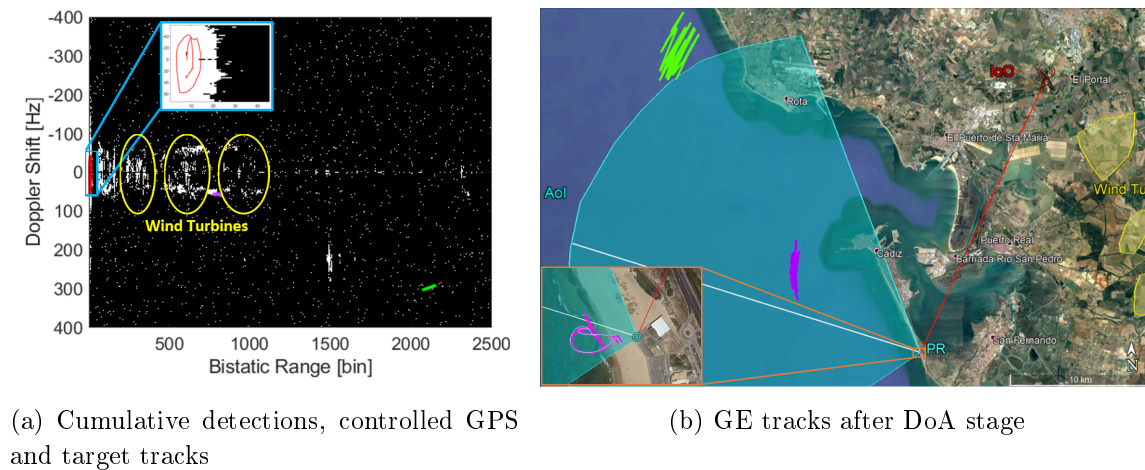
Figure 5.20: Results of trials in a maritime scenario.

## Trials in rural scenario

- In January 2020, a trials campaign in the rural scenario 1 was carried out with the objective of demonstrating the capabilities of IDEPAR for detecting and tracking small UAVs in the vicinities of an airport, which is actually of great awareness for avoiding possible collisions. Two different controlled drones were employed: a

M200 quadcopter with carbon fibre blades and a Phantom 4 which blades are made of plastic. One acquisition with controlled M200 was presented in Section 4.4 to prove the effect of non-null conductivity air-screws. Here, a measurement with Phantom 4 as controlled target is presented. The cumulative detections during the 40 s acquisition at 770 MHz employing the detection scheme proposed in [157] is shown in Figure 5.21(a), achieving a $P_D = 67\%$. Figure 5.21(b) shows the difference between estimated angle of arrival and the real one (ground truth GPS data).



(a) Cumulative detections      (b) DoA comparison
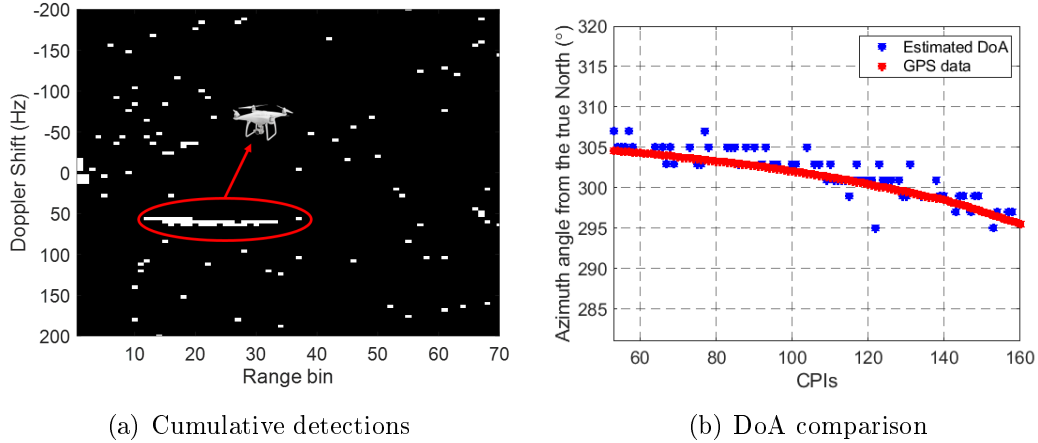
Figure 5.21: Results of trials in rural scenario 1.

- In December 2020, IDEPAR was deployed in the rural scenario 2 for radar trials with the objective of estimating the altitude or elevation angle of small aerial targets (drones). This estimation at the same time that azimuth one will provide 4D information about the target: X, Y, Z position in the space by means of the range and angles, and velocity through Doppler.

  For this task, the array geometry changed to an L-shape array formed by a ULA of 6 elements ($d_{ULA} = 201$ mm), for azimuth angle estimation, and an extra element located below the first one of the array, for estimating elevation angle through phase-interferometry technique (Figure 5.16). The separation between the two elements located vertically for elevation estimation is $d_v = 612$ mm, which, at the measurements central frequency of 534 MHz, avoids ambiguities for $|\theta| \leqslant 27.3°$.

  Two small UAVs were employed as controlled targets, a Phantom 3 and a Mavic Mini, whose main characteristics are summarized in table 5.8.

  The two-dimension angular estimation results for acquisition with each of the drones is shown in Figure 5.22. To check performance, estimated angles are compared with ground truth real GPS data, showing better precision in the case of Phantom, probably due to its greater size that implies a greater SIR and better accuracy. Figure 5.22 also shows the tracks obtained from range and azimuth angle (and PR geometries knowledge) represented over GoogleEarth for both cases.

Table 5.8: Controlled targets characteristics in rural scenario 2.

| Model | Size | Blades Radius | Material | Maximum Range | Maximum Speed |
|---|---|---|---|---|---|
| Phantom 3 | 250×250×190 mm | 120 mm | Plastic | 3.5 km | 16 m/s |
| Mavic Mini | 159×202×55 mm | 43 mm | Plastic | 4 km | 13 m/s |



(a) Azimuth Mavic



(b) Elevation Mavic



(c) GE track Mavic



(d) Azimuth Phantom



(e) Elevation Phantom



(f) GE track Phantom
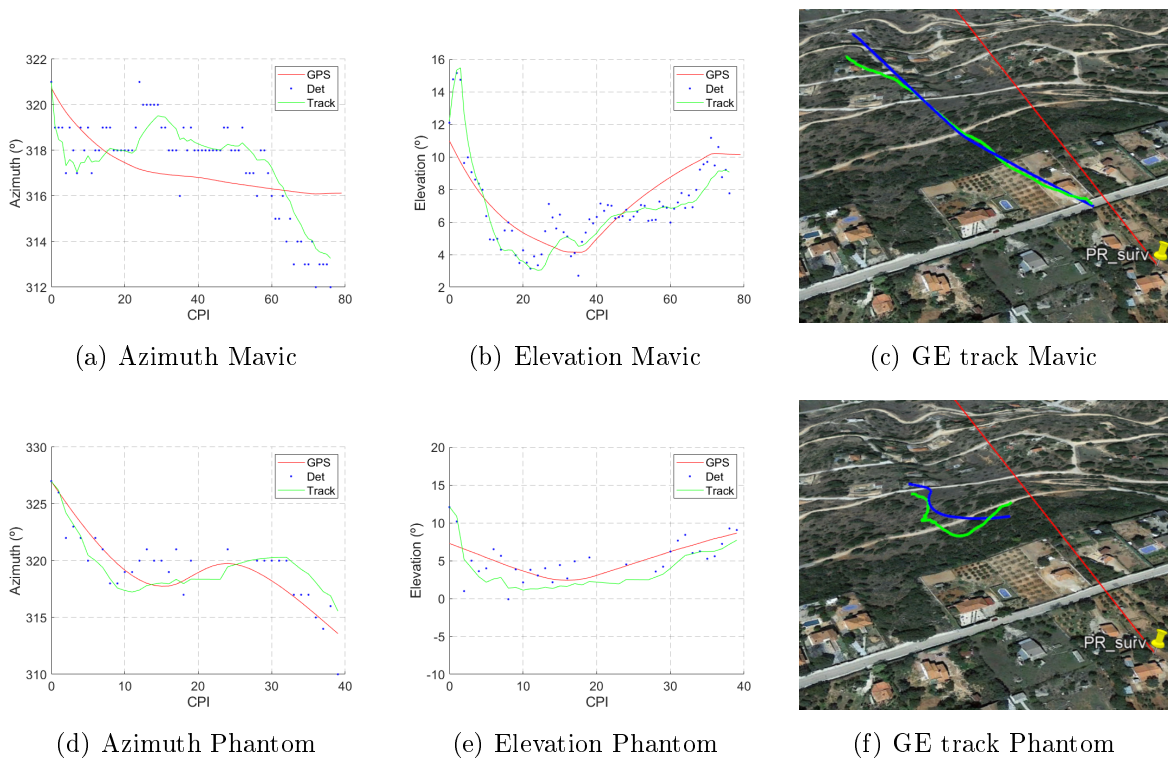
Figure 5.22: Results of trials for small aerial targets elevation estimation in rural scenario 2.

# Chapter 6

# Reflectarray Design Method for DVB-S based Passive Radar

Satellite broadcasting or positioning systems provides nearby global availability, allowing a passive radar to operate even in remote areas isolated from civilization or in conflict scenarios. The satellite IoO geometry also reduces shadow zones in which the corresponding signal is not received, and therefore neither the PR could not be located there nor targets would be detected. Besides the advantages of satellite IoOs, the employment of Digital Video Broadcasting-Satellite (DVB-S) signals provides others as an appropriate ambiguity function, high range resolution due to broad bandwidth, and interesting potential for Inverse Synthetic Aperture Radar image generation due to the higher operation frequency (from 10.7 GHz to 12.75 GHz). Besides of that DVB-S employs geostationary satellites simplifying the geometry and processing.

The main drawback of geostationary satellite IoOs is the high propagation losses due to the transmitter location at thousands of kilometres away from the system, together with the high operation frequency. The power scattered from the targets is very low, so high gain surveillance antennas are required to allow detecting small targets, as the ground ones, considered in scenarios presented in Section 3.4.1.2. The relation between the antenna gain and the radiation pattern defines a complex design problem: the generation of wide enough radiation beams capable of covering the area of interest, providing the required gain to fulfil sensitivity requirements.

Main requirements of the DVB-S surveillance antenna can be extracted from the study carried out in Chapter 3 and 4. Employing coverage estimation represented for both trials scenarios in Figure 4.6, it can be defined an antenna gain of around 20 dBi to assure a detection probability $P_D = 80\%$ for big cars. Analysing trials scenarios (Section 3.4.1.2) it can be defined a minimum azimuth beamwidth of 8° to cover a wide enough section of the roads that allows the system to track targets during at least some seconds, which will give important information to validate the detections; the elevation beamwidth could be narrower than azimuth to allow a higher directivity. If an elevation beamwidth of 4° is fixed, the gain requirement could be achieved with an antenna radiation efficiency of at

least 67% (Equation 2.8 and 2.7).

Common solutions for DVB-S reception are based on commercial parabolic dish antennas, which provides high efficiency and gain but a narrow pencil beam. Those antennas, can fulfil coverage requirements for communications applications, but they are not well suited for radar applications because the pencil beam radiation pattern limits the surveillance area. For example, the commercial parabolic dish antenna *AMP78* employed up to this moment in IDEPAR demonstrator [17] provides a maximum directivity of 32 dBi ($G_{max} \simeq 30$ dBi) with a HPBW of only 4°. An alternative to commercial parabolic antennas, specially for these kind of applications, are reflectarray antennas [127] (Section 2.5).

This chapter presents two different solutions based on reflectarray antennas to tackle the challenging requirement of a passive radar surveillance antenna with high gain and a beamwidth that ensures enough angular coverage.

## 6.1 Multi-Feed Multi-Beam Reflectarray

Reflectarray antennas generating multiple beams from multiple feed has been studied in literature [158] [159]. The objective in this section is to design a method that will locate two beams generated by two feeds in angular positions such that its sum-pattern provides a sectorial beam fulfilling the required azimuth beamwidth [160].

### 6.1.1 Design process

Rectangular patches were selected as the elements of the reflectarray. Their change in phase reflection coefficient was characterized, as a function of the variations in the length and width of the patch, by employing the electromagnetic simulation software ANSYS HFSS through unit cell analysis with Finite Element Method (FEM). The cell size was fixed at 16.9 mm ($0.6\lambda$, Equation 2.25) and the employed substrate was Rohacell HF31 that has a relative permittivity close to air ($\varepsilon_r = 1.05$) with a height of 1 mm. The patch layout and cell configuration for finite element simulation technique are shown in Figure 6.1(a). The simulation was carried out for length and width in steps of 0.1 mm, in order to fit it to fabrication tolerance. Figure 6.1(b) shows the results of simulated "S" curve of the element.

A $32 \times 32$ elements reflectarray was designed, which means $54 \times 54$ $cm^2$ to operate around 11 GHz. The feed was selected to be an E-Plane WR90 horn with around 30° beamwidths in both azimuth and elevation planes, and a maximum gain of 16 dBi (Figure 6.2). Feed characteristics imply that the aperture efficiency of the reflectarray is maximized for an $f/D = 1.04$, being this efficiency $\eta_a = 72.6\%$ (Equations 2.22, 2.23).

The reflectarray design proposed in this section achieves sectorial beam requirement, wider in azimuth plane than elevation, by combining two consecutive beams created by two different feeds illuminating the same aperture. This combination of beams is called

(a) Element

(b) Element "S" curve
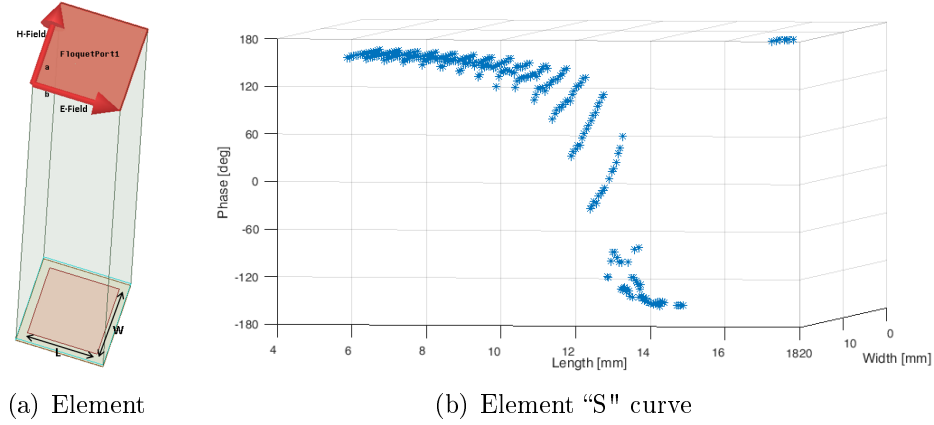
Figure 6.1: Elements characterization.



(a) Feed Horn

(b) Horn radiation pattern cuts
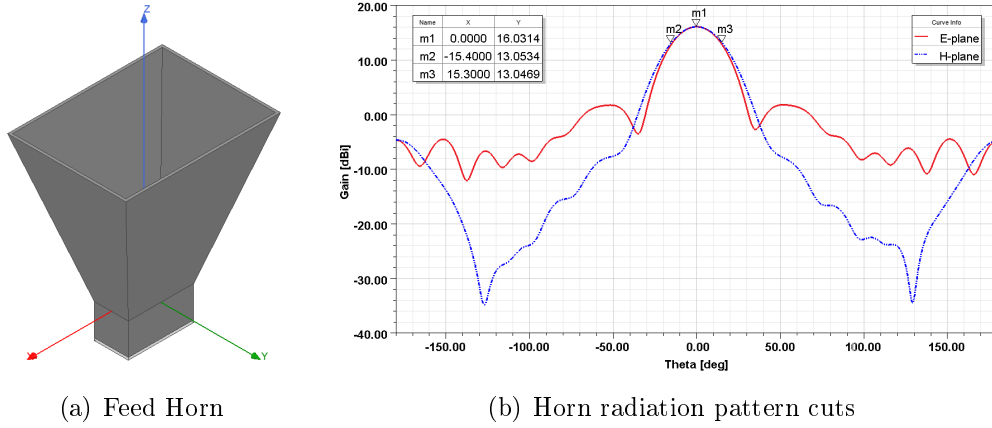
Figure 6.2: Feed model and radiation pattern cuts.

the sum-pattern. For this purpose, the two feeds must be located slightly shifted from origin a distance $\pm\mathbf{x}_f$ being both of them in symmetrical positions with respect to the centre of the reflector. For desired steering of both beams towards direction $(\theta_{b1}, \varphi_{b1})$ and $(\theta_{b2}, \varphi_{b2})$, the $\mathbf{x}_f$ distance must be adjusted to produce identical phase distribution maps for both feeds (Equation 2.26). This is made through an optimization algorithm based on gradient to minimize the difference between the required phase of each element for achieving each of the beams with its associated feed (Equation 6.1). The final phase distribution is shown in Figure 6.3(a), and the resultant reflectarray is shown in figure 6.3(b). Patch sizes vary from $5 \times 5 \ cm^2$ to $16.9 \times 16.9 \ cm^2$.

$$\min \left( \phi_{\mathbf{r}}(\theta_{\mathbf{b1}}, \varphi_{\mathbf{b1}}, -\mathbf{x_f}) - \phi_{\mathbf{r}}(\theta_{\mathbf{b2}}, \varphi_{\mathbf{b2}}, +\mathbf{x_f}) \right) \tag{6.1}$$

(a) Phase distribution map



(b) Simulated reflectarray
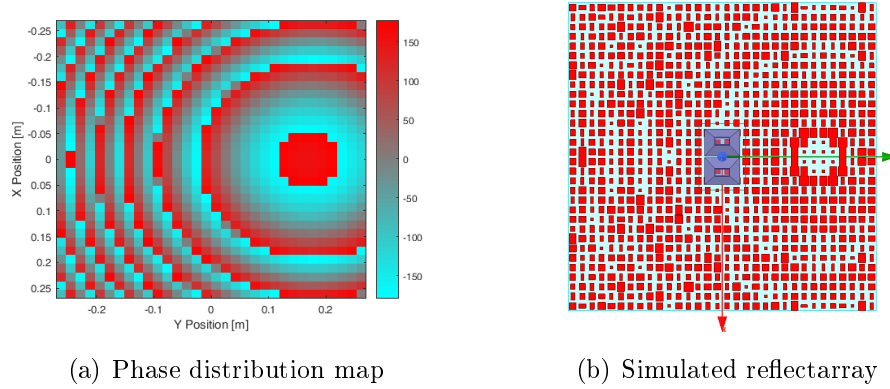
Figure 6.3: Reflectarray design for $[\theta_{b1}, \varphi_{b1}] = [16°, 82°]$ and $[\theta_{b2}, \varphi_{b2}] = [16°, 98°]$. Both feeds are shifted a distance $|x_f| = 25$ mm from origin. The focal distance is $F = 596.2$ mm.

## 6.1.2   Simulation Results

The designed reflectarray was modelled and simulated in ANSYS HFSS (Figure 6.3(b)). Representing the cut of all $\phi$ for $\theta = 16°$, it can be checked how both beams steer to the design ones $\varphi_{b1} = 82°$ and $\varphi_{b2} = 98°$ (Figure 6.4(a)). For correctly measuring the beamwidths of the resulting sum-pattern, an auxiliar coordinate system must be created with its Z-axis pointing to the same direction that the main beam ($\theta = 16°$,$\phi = 90°$) being the radiation results represented over this auxiliary system. Figure 6.4(b) shows the azimuth plane radiation pattern of both beams and the resulting of combining both through sum-pattern, achieving a total beamwidth of 8.2°. The sum-pattern elevation cut and 3D representation are shown in Figure 6.4(c) and 6.4(d), respectively. The elevation HPBW at 11 GHz is 3.6° and the maximum gain 25.8 dBi.

A study at different frequencies was carried out to prove the radiation pattern sensitivity. Results shows that the gain is reduced less than 3 dB at 11.5 GHz maintaining the angular coverage. From this frequency forward, gain is reduced considerably (Figure 6.5). So, the working bandwidth of the antenna extends within the frequencies from 10.75 GHz to 11.5 GHz, which allow to acquire numerous DVB-S channels, which will have a positive impact in the system resolution.

The two consecutive beams of the reflectarray antenna allow the implementation of amplitude-comparison monopulse technique for direction finding of the echoes of the targets. The achievement of angular discrimination in the PR will improve significantly the tracker performance. This technique is based on the calculation of the ratio between sum and difference patterns of the two beams [161] [162].

(a) Cut at $\theta = 16°$



(b) Azimuth plane cuts



(c) Sum-pattern elevation
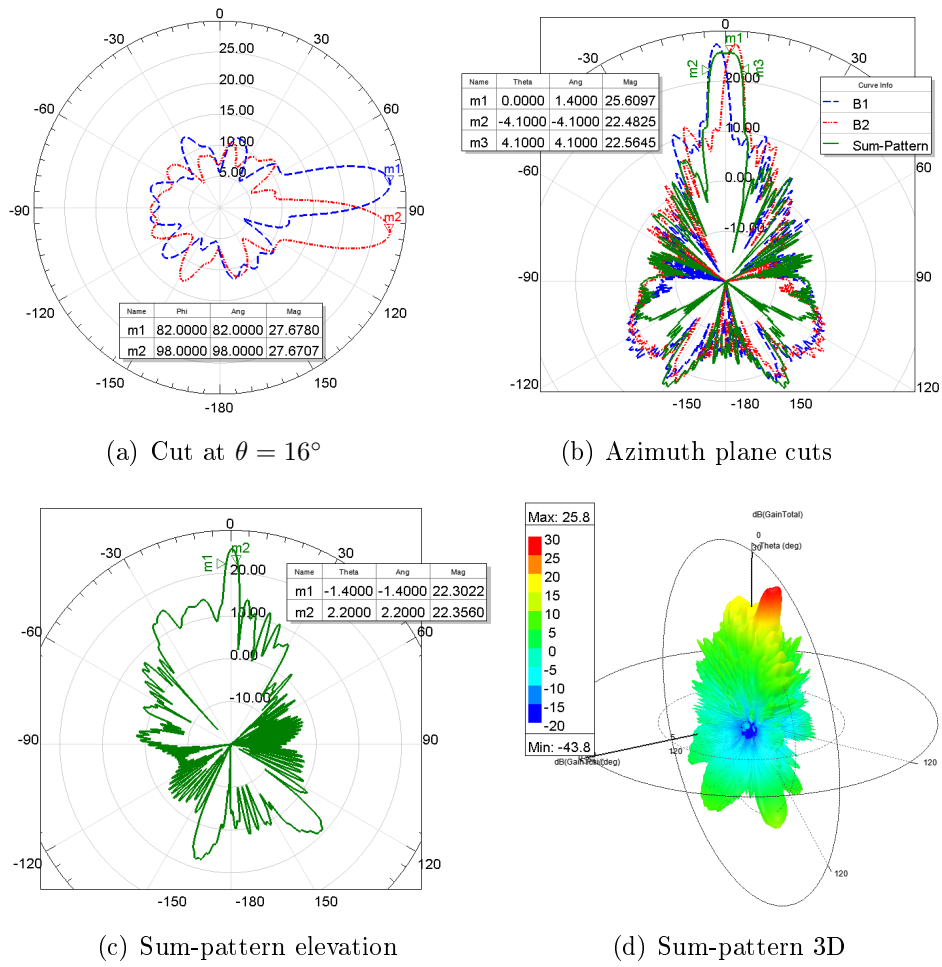


(d) Sum-pattern 3D

Figure 6.4: Simulated radiation pattern of designed reflectarray at 11 GHz.
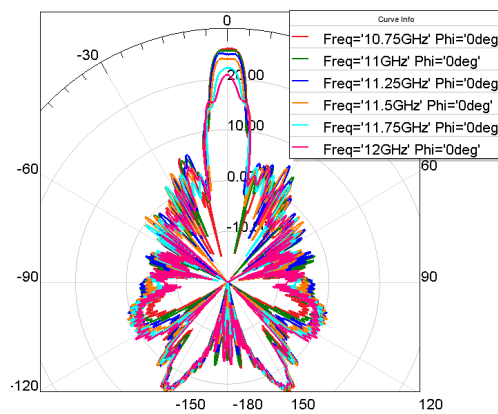


Figure 6.5: Sum-pattern azimuth plane sensitivity versus frequency.

## 6.2   Sectorial Beam Reflectarray Design through Multi-Beam Optimization

The design of a reflectarray with sectorial beam pattern, or in general any with shaped-pattern, usually requires that the phase distribution is calculated through an optimization process as there is not analytical expression for it. In the literature, different techniques were applied for direct estimation or optimization of the required phase in each element [163] [164]. In this section, a new method based on the estimation of the best steering of several contiguous beams is presented. The combination of the optimized contiguous beams allows to achieve a sectorial beam that suits perfectly in the PR system for the detection and tracking of ground targets. Presented results have been included in the paper entitled *Design and Validation of a Reflectarray Antenna with Optimized Beam for Ground Targets Monitoring with a DVB-S based Passive Radar* submitted to Sensors MDPI Journal as an extension of the work presented in [165]. This contribution is under review.

### 6.2.1   Design method

The method proposed for designing a sectorial beam reflectarray is based on the combination of several contiguous beams, located at a certain angular distance from each others. An optimization algorithm is employed to find the best steering of each beam that allows to form up the sectorial one with desired beamwidths and also minimizing SLL. A particle swarm optimization (PSO) algorithm has been chosen for this purpose [166].

The optimization vector is composed of 4 variables or *particles*. In the i-th iteration: $\mathbf{P_i} = [v_{b_1,i}; v_{b_2,i}; A_{b_0,i}; \phi_{cent,i}]$. Reflectarray pattern is calculated in UV coordinates. The two first variables of each particle are the $v$ positions of the maximum of radiation of two contiguous beams ($v_{b_1}$ and $v_{b_2}$). The $u$ position for all the beams is fixed by the desired steering of the final sectorial beam $\theta_{sa}$ (Equation 6.2).

$$u_b = sin(\theta_{sa}) \tag{6.2}$$

It is expected that, these two beams ($v_{b_1}$ and $v_{b_2}$) together with zero steering beam ($v_{b_0}$) and other two symmetrical beams to these at zero leftside ($-v_{b_1}$ and $-v_{b_2}$) achieve a sectorial beam of the required beamwidth. The weighted arithmetic mean of the phases required at each element for generating each of those beams (Equation 6.3) is taken for calculating the radiation pattern of a reflectarray of $M$ row elements by $N$ column elements through array theory formulation [132] (Equation 2.27). The coefficients employed in the weighted arithmetic mean are: $A_{b_0}$ for the phases that generate the zero steering beam; ones for the other 4 beam cases.

$$\phi_r(xi, yi) = \frac{\sum_{i=-2}^{2} A_{bi} \cdot k_0(d_i - (x_i cos\varphi_{bi} + y_i sin\varphi_{bi})sin\theta_{bi})}{\sum_{i=-2}^{2} A_{bi}} \tag{6.3}$$
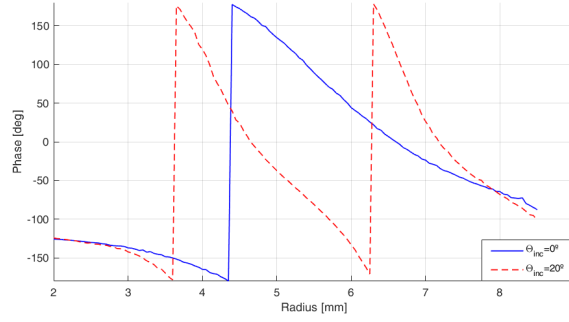
Figure 6.6: S-curve of a ring element for two incidence angles.

Being $tan\varphi_{bi} = \dfrac{u_b}{v_{bi}}$ and $sin\theta_{bi} = \sqrt{u_b^2 + v_{bi}^2}$.

The real phases achievable with the elements ($\phi_r$), previously obtained by electromagnetic simulations, are employed, instead of ideal ones, to calculate a most reliable radiation pattern, as well as the losses ($|s_{11}|$) introduced by each element. Figure 6.6 proves that the S-curve of the elements varies significantly as a function of the angle of incidence, being 0° the broadside direction. For this reason, the real phases and losses for a set of incidence angles comprising all the possible range, from normal to maximum incidence, are employed $\mathbf{\Theta_{inc}} = [0°, 5°, 10°, 15°, 20°, 25°, 30°, 40°, 50°]$, assigning to each element the nearest angle of $\mathbf{\Theta_{inc}}$. The fourth optimization variable fixes the phase of the central element, shifting the phases of all the element in order to not change the phase distribution. Optimizing this variable allows having the different elements in the most efficient distribution according to their real losses.

The radiation pattern of a reflectarray can be estimated through array summation from the feed pattern, the geometry knowledge and an accurate characterization of the reflection coefficients of the elements following Equation 2.27 for linear polarization, which is repeated here for convenience (Equation 6.4). The calculus of the radiation pattern (RP) is more useful in UV coordinates, because the optimization techniques employed to achieve the required radiation distribution are based on the comparison of the pattern with some masks, which are easily defined in UV space.

$$E_r(u,v) = \sum_{m=1}^{M} \sum_{n=1}^{N} E_{inc_{m,n}} |\Gamma_{m,n}| e^{j\phi_{m,n}} e^{jk_0(ux_{m,n}+vy_{m,n})} \tag{6.4}$$

The cost function to be minimized has been designed in such way that not only two main radiation cuts are optimized but all the pattern in the UV space is considered for better performance. A mask in azimuth plane ($mask_{inf}$) is employed to force the design to fulfil the required $-3$ dB beamwidth, but the SLL is estimated in all the space by means of a two dimensional mask ($mask_{2D}$) that delimits the area outside the main beam, being it defined by the $-10$ dB beamwidths (Figure 6.7). Only the points of that area in which the radiation is above a determined level are computed in the cost function, trying to minimize
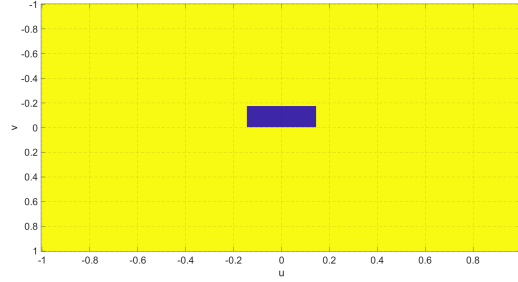
Figure 6.7: 2D mask in UV space to calculate the SLL outside (yellow part) the main beam (blue part) area.

the radiation outside the main beam, that is minimizing the SLL. A pseudo-directivity $(\widehat{dir})$ is considered as the ratio between the maximum radiation of the main beam and the mean radiation in the area outside the main beam (delimited by $mask_{2D}$, Equation 6.6). Three constants are employed to control the influence of each of the parameters: $K_1$ for pseudo-directivity, $K_2$ for azimuth beamwidth and $K_3$ for SLL.

$$C = -K_1 \hat{dir} + K_2 \sum_{v=-1}^{1} RP_{azi} < mask_{inf} + K_3 \sum_{v=-1}^{1} \sum_{u=-1}^{1} RP_{2D} > mask_{2D} \qquad (6.5)$$

Being:

$$\hat{dir} = \frac{max(E_r(u,v))}{\overline{E_r}(u_m,v_m)}; \quad (u_m, v_m) \in mask_{2D} \qquad (6.6)$$

$$RP_{azi} = \frac{E_r(u_b,v)}{max(E_r(u_b,v))}; \quad v \in [-1,1] \qquad (6.7)$$

$$RP_{2D} = \frac{E_r(u,v)}{max(E_r(u,v))}; \quad (u,v) \in [-1,1] \qquad (6.8)$$

## 6.2.2 Reflectarray Design Employing Commercial Feeding Structure

The method presented in previous section has been employed to design a reflectarray that could employ the feed, feedarm and aperture holding structure from a commercial parabolic dish antenna, allowing a cheap and fast assembling. The aperture is elliptical to help achieving a sectorial beam. This section presents each of the parameters employed for the designed and the simulation results.

### 6.2.2.1  Feed Characterization

The reflectarray will be fed with a commercial *Skyware* horn antenna. It is an axial corrugated horn in which the geometry's parameters cannot be measured, as its aperture

(a) Anechoic chamber assembly

(b) E-plane and H-plane cuts
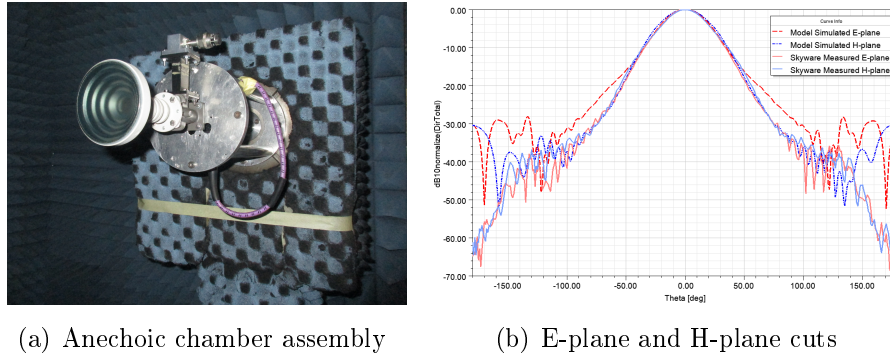
Figure 6.8: *Skyware* antenna study: assembly for characterization in anechoic chamber (a); measured radiation pattern and the simulated one with the model created from measurements (b).

is covered by a protective dielectric sheet, so it is difficult to model it in the electromagnetic simulator. In order to achieve an optimum design, the real aperture illumination must be taken into account, so the feed radiation pattern is obtained by characterizing it in the anechoic chamber of the *High Technology and Homologation Centre (CATECHOM)* of University of Alcalá (Figure 6.8(a)).

The results of the radiation pattern measurements in the anechoic chamber are directly employed for the first stage of the design process: it defines $E_{inc_{m,n}}$ of Equation 6.4 for the optimization process. But the measured radiation pattern has been also employed to model a feed in ANSYS HFSS for the second stage: the check of performance through electromagnetic simulation and fine adjustments. The feed has been modelled as a *Potter* horn [167], a kind of antenna that provides excellent radiation pattern with suppressed sidelobes, similar to the characteristics obtained in the measurement of the *Skyware*. The Potter antenna is composed of different cylinder and conical sections that serve as a step transition in diameter. The optimization of the different diameters and lengths of this sections allows to find a horn model that minimizes the differences with the measured RP, specially in the region of interest ($D_{norm} \geq -10$ dB). The comparison between the measured RP cuts and the simulated with the model created is shown in Figure 6.8(b).

### 6.2.2.2 Geometry Selection

The geometry of a reflectarray and its main parameters were shown in Figure 2.19, in which the origin of the coordinate system was fixed in the centre of the aperture. In the design carried out in this section, the main geometrical parameters are imposed by the commercial feed-arm and aperture holding structures (Figure 6.9):

- The feed is located at position $X_f = 138.7$ mm, $Y_f = 7.1$ mm (due to feedarm misalignment) and $Z_f = 179.7$ mm. This position implies a focal length $f =$

Figure 6.9: Commercial feed-arm and aperture holding structure employed for the design.

227 mm. It has an angle of rotation $\theta_f = 28.78°$ with respect to the normal of the aperture.

- The feed-arm limits physically the maximum semi-distance from the centre to one edge of the aperture in X axis dimension to $S_x = 220$ mm.

- The focal length to reflectarray diameter ratio $(F/D)$ is selected to maximize aperture efficiency $\eta_a$ in Y axis dimension while X axis size $(D_x)$ is increased from the one achieving maximum aperture efficiency in order to decrease the elevation beamwidth. According to the horn radiation pattern and focal length, the aperture efficiency in the normal plane to Y axis is maximum for $F/D_y = 0.83$ ($\eta_a = 68.6\%$), which means $D_y = 273$ mm. $D_x$ is fixed to be about 374 mm, achieving an aperture efficiency of $\eta_a = 61.4\%$ (Equation 2.24).

- The inter-element spacing is fixed to be 17 mm (Equation 2.25), so a reflectarray of $22 \times 16$ element can be designed.

### 6.2.2.3 Element selection

The element selection is a key step in reflectarray design, because it determines the reflection efficiency and the bandwidth of the antenna.

In order to cover all the range of phases needed ($\pm 180°$) with a smooth slope, two different elements are employed for the design (Figure 6.10) and their distribution is shown in table 6.1. The patch elements are located over a *FR4* substrate of 1.6 mm of thickness which is also over a 6 mm air substrate. Ground plane is located below the air substrate.

Table 6.1: Range of phases covered up by each element and its associated losses.

| Element type | Phases | Losses |
|:---:|:---:|:---:|
| Circle plus triangle | $(-180; -125.5] \cup [152; 180)$ | $|S_{11}| > -0.6$ dB |
| Ring $w_{ring} = 1.8mm$ | $(-125.5; -20]$ | $|S_{11}| > -3.0$ dB |
| Ring $w_{ring} = 2.8mm$ | $(-20; 152]$ | $|S_{11}| > -2.1$ dB |

(a) Circle + triangle           (b) Ring
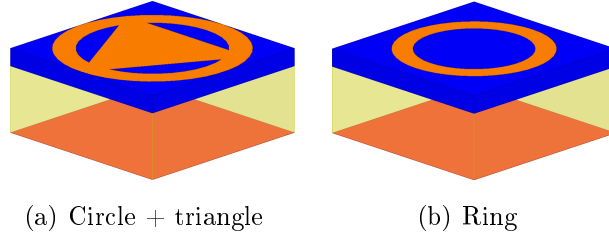
Figure 6.10: Elements selected for the design.



(a) Normal incidence ($\Theta_{inc} = 0°$)           (b) $\Theta_{inc} = 20°$
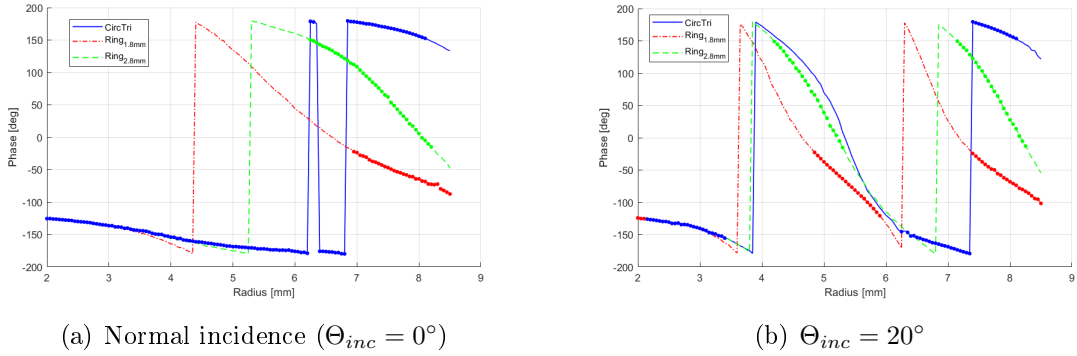
Figure 6.11: S-curve of selected elements for normal incidence and $\Theta_{inc} = 20°$, highlighting the valid ones in each case according to the maximum allowed losses.

The S-curves of the selected elements were simulated by unit cell analysis and configured for horizontal polarization in the final design. The results representing the variation of the phase as a function of the size are shown in Figure 6.11. The reflection coefficient phase varies significantly with the angle of incidence, so it must be taken into account in the reflectarray design process. There is a gap of non-covered phases within the range $[-120, -90]$ (Figure 6.11(a)) which does not happen for other incidences, so the proposed design method will solve this problem by not selecting these phases for the centre elements.

#### 6.2.2.4   Results for design based on commercial elements

The proposed method is configured with the following requirements and parameters for calculating the cost, besides the characteristics described in previous sections:

- Design frequency $f = 11$ GHz and $\theta_{sa} = -5°$.

- Azimuth 3 dB beamwidth: 10°. Elevation 3 dB beamwidth: 6°.

- Azimuth 10 dB beamwidth: 16°. Elevation 10 dB beamwidth: 9°.

- SLL: $-20$ dB.

- $K_1 = 0.1$; $K_2 = 2$; $K_3 = 10$.

(a) Azimuth and elevation cuts



(b) 3D RP and mask plot
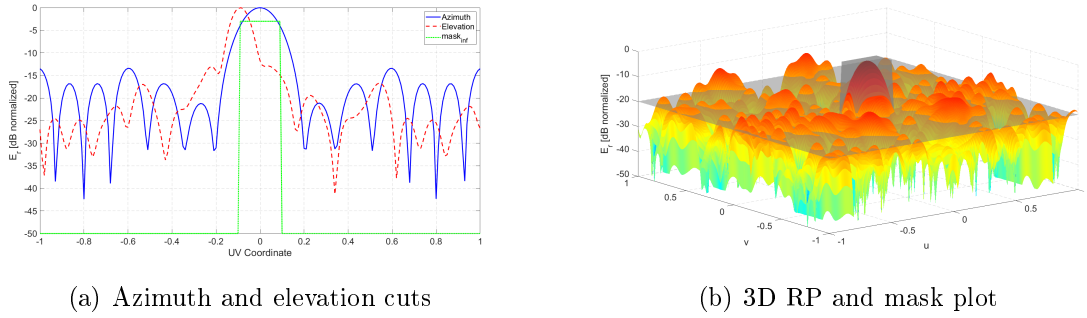
Figure 6.12: Results for reflectarray design at 11 GHz.

The method described in section 6.2.1 gives the best cost result ($C = 9.1$) for beams positions $\varphi_{b1} = 0.0509$ and $\varphi_{b2} = 0.0671$, zero-beam pondering as half ($A_{b0} = 0.5$) and central element phase $\phi_{cent} = 48.3°$ (ring element of $w_{ring} = 2.8$ mm). Azimuth and elevation cuts of resulting RP are shown together with $mask_{inf}$ in Figure 6.12(a). Figure 6.12(b) shows the 3D radiation pattern of the achieved design and the $mask_{2D}$ employed for SLL minimization.

The phase distribution obtained in the optimization process was employed to model a reflectarray in ANSYS HFSS with the elements and geometry parameters previously described. It has been simulated by employing the Finite Element-Boundary Integral (FE-BI) method, because the design is electrically large. It was fed with the *Potter* horn modelled to imitate the real *Skyware* antenna (Figure 6.13(a)). *Foam* spacers that will allow to have a thick air substrate between the *FR4* and the ground plane are also included in the simulation. The simulation results are shown in Figure 6.13(b). A 3 dB azimuth beamwidth of 9.4° is achieved as well as 5.2° elevation beamwidth, with a maximum directivity of 19.13 dBi. High radiation levels are observed in the elevation cut at angles between $-40°$ and $-20°$ due to the specular radiation from the feed.

## 6.2.3   Alternative designs for a DVB-S Passive Radar

The proposed method (Section 6.2.1) has been also employed for designing a reflectarray without the restrictions of commercial elements.

A feed that optimize the illumination efficiency has been designed. To achieve a sectorial beam, the aperture must be narrower in the dimension of the sector than in the opposite one, so a non-symmetrical feed is required. A "prolate" type horn [168] is employed to maximize the radiation contained in the main beam (Figure 6.14(a)). This horn was designed to maximize the directivity, which will improve also the reflectarray efficiency, fulfilling beamwidths of 15° × 20° in E and H planes, respectively (Figure 6.14(b)). This design will help to achieve a reflectarray with sector radiation in azimuthal plane and horizontal polarization.

The designed feed provides maximum aperture efficiency for $F/D_E = 1.8$ and $F/D_H = $

(a) Reflectarray design

(b) Directivity azimuth and elevation cuts at 11 GHz
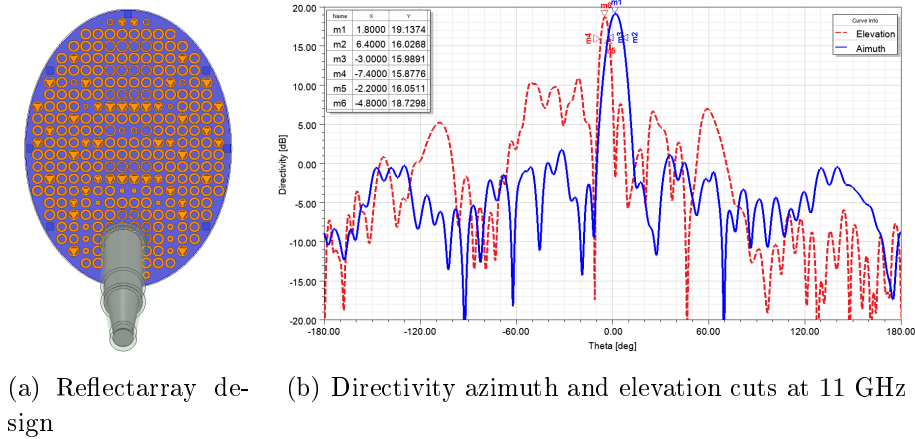
Figure 6.13: Reflectarray modelled in HFSS and simulation results showing radiation pattern cuts.



(a) Horn model

(b) Radiation pattern cuts
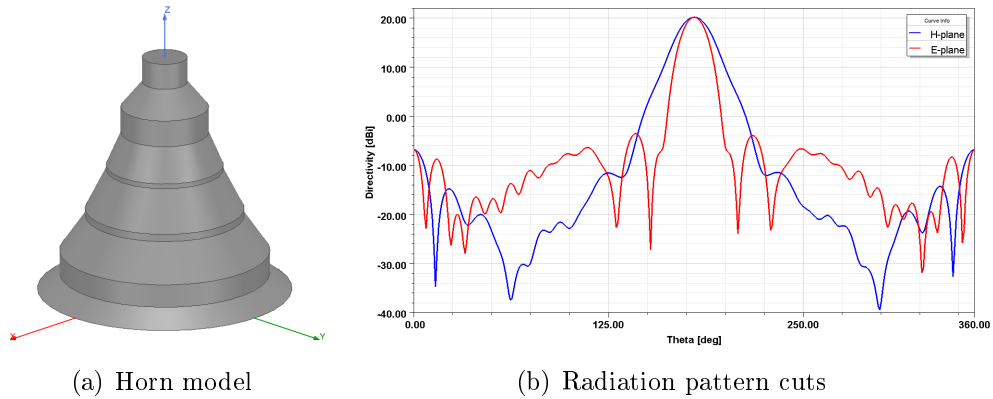
Figure 6.14: Model of designed "prolate" type horn and its directivity radiation pattern cuts for E and H planes.

1.4 for feed E and H planes, being them $\eta_{a_E} = 77.7\%$ and $\eta_{a_H} = 76.4\%$, respectively (Equation 2.24). If the maximum dimension of the reflectarray is fixed to around 80 cm, a reflectarray of $48 \times 36$ elements can be designed with a focal length of 1.1 m. If the rectangular lattice for element distribution is changed to an hexagonal lattice, the number of elements that can be located in the same area increases. In this design, in the same elliptical aperture, $55 \times 36$ elements can be located, so a performance improvement in radiation patterns is expected.

Figure 6.15(a) shows the designed reflectarray with hexagonal lattice modelled in ANSYS HFSS. The azimuth pattern cut comparing square with hexagonal lattice (Figure 6.15(b)) shows that the hexagonal lattice improves mainly the sidelobes around the main beam. Both designs achieve an azimuth beamwidth of 9.6° with a maximum directivity of 24.8 dBi.

In [165] it was proved that if the size of the reflectarray aperture is increased up to

(a) Reflectarray model                    (b) Azimuth pattern cuts
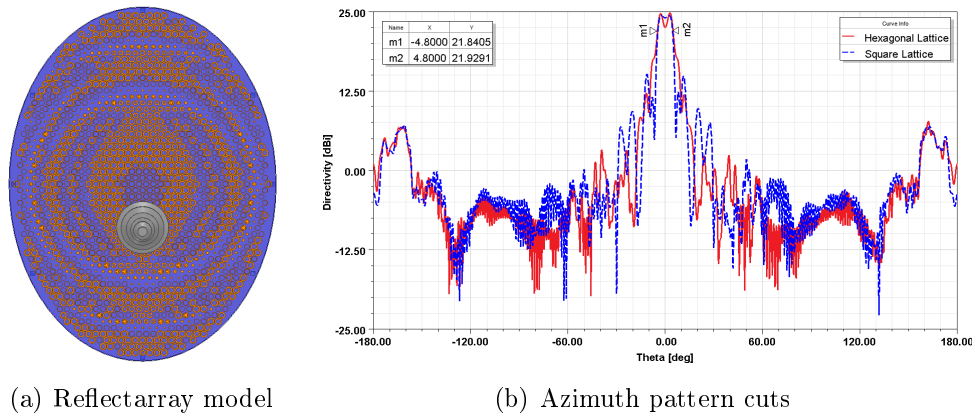
Figure 6.15: Hexagonal lattice reflectarray modelled in HFSS and simulation results comparing its azimuth cut with a same size square lattice reflectarray.

1.1 m in its maximum dimension, a maximum realized gain of 28.38 dBi can be achieved, with a bit narrower sector beamwidth of 7.4°.

## 6.3    Sectorial Beam Reflectarray Prototype based on commercial components

The elements distribution of the reflectarray designed in Section 6.2.2 was transferred to a $FR4$ Printed Circuit Board (PCB) through chemical etching. The reflectarray antenna was manufactured assembling the ground plane and the $FR4$ board that contains the patches, with foam spacers to generate the intermediate air substrate, and it was installed in the commercial holding structure and feed-arm for horn positioning described in Section 6.2.2. It was characterized in the anechoic chamber of the CATECHOM of University of Alcalá (Figure 6.16). Due to the dimensions of the anechoic chamber (L= 3.6 m) and the maximum diameter of the antenna (D= 40 cm), the measurements were carried out in near field and transformed to far field. The antenna under test (AUT) gain was estimated employing a standard gain antenna and applying the Friis transmission formula and the corresponding near field to far field conversion factors [169].

First a near field elevation cut was made at design frequency (11 GHz) in order to calibrate the manual elevation steer system of the antenna holding structure: with this first measurement the system was fixed in such way that the main beam steered approximately to the horizontal plane. After this first measurement, the calibrated position was marked in the steer scale and full pattern measurements in a range of frequencies between 10 GHz and 12.5 GHz were carried out.

Measurements results are shown in Figure 6.17. The main cuts at the design frequency (Figure 6.17(a)) are similar to the simulated ones and their beamwidths are 8.7° in azimuth plane and 5.2° in elevation. The gain is above 19 dBi in the frequencies range
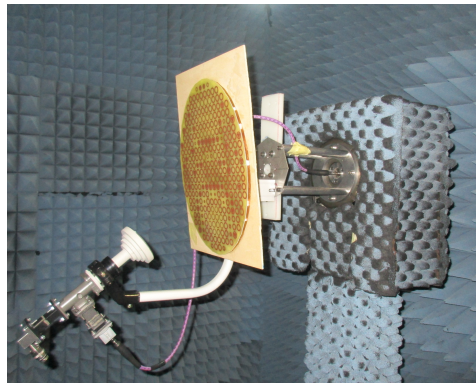
Figure 6.16: Assembly of reflectarray prototype in anechoic chamber for characterization.



(a) Measured gain cuts at 11 GHz

(b) Maximum measured gain
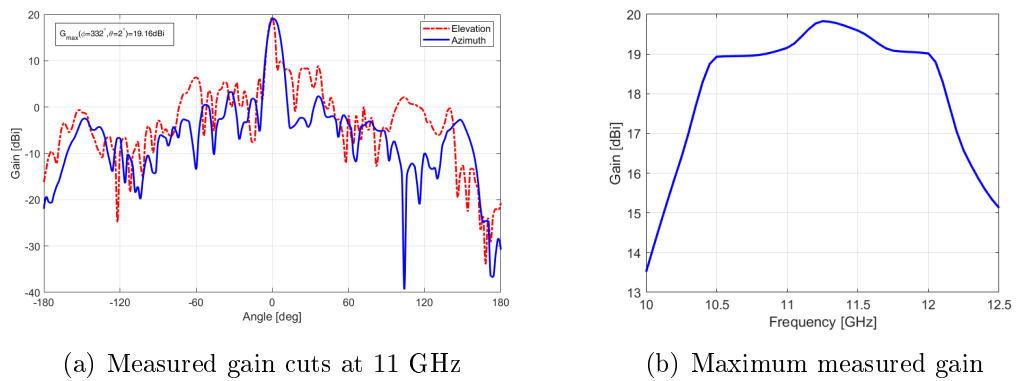
Figure 6.17: Reflectarray characterization results.

$[10.5 - 12]$ GHz, which means that the design antenna can operate in almost the full DVB-S band (Figure 6.17(b)).

## 6.3.1   Validation in Real Passive Radar Trials

To validate the reflectarray prototype, IDEPAR demonstrator was deployed in the two scenarios described in Section 3.4.1.2. A commercial parabolic dish antenna of 80 cm of diameter was employed in the reference channel to acquire the direct signal from *Hispasat 30W-5* satellite, while the designed reflectarray was integrated in the surveillance channel.

Acquisitions in both validation scenarios were carried out at a central frequency of 11.3 GHz, covering three DVB-S channels horizontally polarized, one of 30 MHz and two of 10 MHz (Figure 6.18). The signals were filtered digitally, to eliminate the noise at frequencies where there is no DVB-S channel and an Extensive Cancellation Algorithm (ECA) [21] was employed to mitigate the Direct Path Interference (DPI) improving targets detection. The coherent processing interval (CPI) was fixed to 200 ms generating a set of 75 RD maps from each acquisition of 15 s.
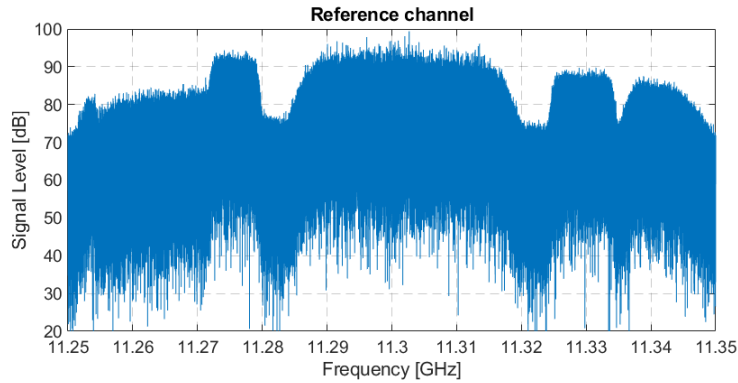


Figure 6.18: Spectrum of the signal acquired by reference channel.

The deployment next to Nursing School for the first trials with the reflectarray antenna was done on the $10^{th}$ of February of 2021. From all the measurements, in the selected one there were two cooperative targets: one of the cars was moving away from the PR and the other started at the end of the road and moved towards the PR. Besides those, there were two more cars in the street at that moment, one moving along each way. Figure 6.19(a) shows the RD map together with the GPS ground truth of cooperative targets for CPI 59. Figure 6.19(b) shows the cumulative of maxima from all the 75 RD maps, each of them normalized by its pedestal noise level, and the GPS ground truth during all the acquisition. The conversion of GPS data to Range-Doppler is not precise when the target is accelerating, because an small error in sample time gives a great difference in Doppler shift ($f_D$) due to the high operation frequency. It can be seen that some targets, bigger than cars, can be detected crossing the round at the end of the street, at range bin around 220.

Figure 6.19(b) can be compared with the results published in [17] in which a commercial dish antenna was employed for the surveillance channel in the same scenario. In it, cumulative of RD maxima of two acquisitions containing a car and a bus were presented.

(a) CPI 59                                    (b) Cumulative RD maxima
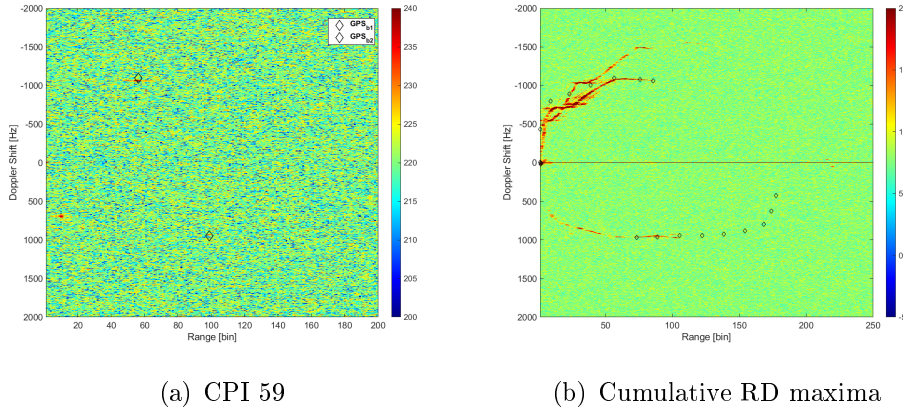
Figure 6.19: RD map results of trials next to Nursing School.

Comparing the car results, a great improvement is observed with the reflectarray antenna, as the signal to interference ratio for same kind of targets in ranges between 50 and 100 has increased considerably.

The deployment in the vicinity of M-121 was done on the $2^{nd}$ of March of 2021. In this scenario there is usually a lot of traffic, so a controlled target was not employed in the measurements. In the selected measurement, the following targets were in the surveillance scenario, checked by video ground truth (Figure 6.20(a)):

- **Moving away:** from nearer to further of the PR, a car probably out of the main beam, the next two vehicles are in the RD at ranges about $\sim 150$ and $\sim 200$ and $f_D \simeq -1700$ Hz (Figure 6.20(b)) and further another set of 2 cars, one of which appears at range $\sim 300$ and $f_D \simeq -1300$ Hz.

- **Approaching:** A concrete truck, that appears at range $\sim 330$ and $f_D \simeq 1100$ Hz, followed by a car that is not appreciated in the RD map.

The set of 75 CPIs were passed through a CA-CFAR (Cell Average-Constant False Alarm Rate) detection stage configured for desired false alarm probability $P_{fa} = 10^{-4}$ and $P_D = 80\%$ followed by a tracker stage based in Kalman filter. The cumulative results of the 75 CPIs for both scenarios trials are presented in Figure 6.21 showing the tracker tracks with their associated detections in black, the false alarms in grey and, in case of scenario next to Nursing School, the GPS ground truth for both targets. It can be checked than the same number of tracks as targets were obtained.
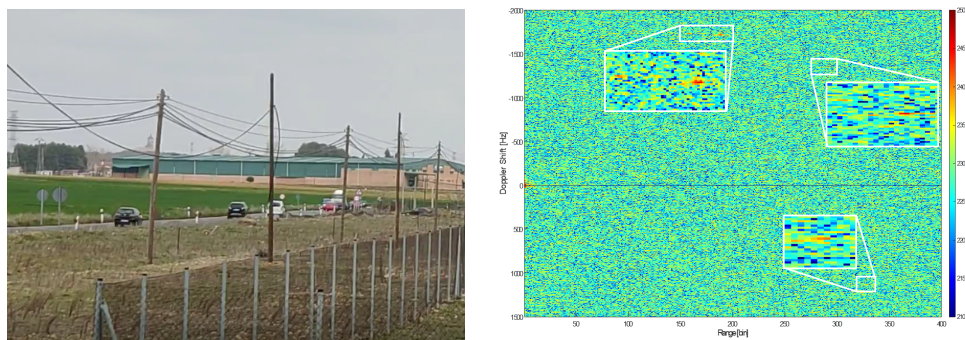
(a) Video frame CPI 35



(b) RD CPI 35
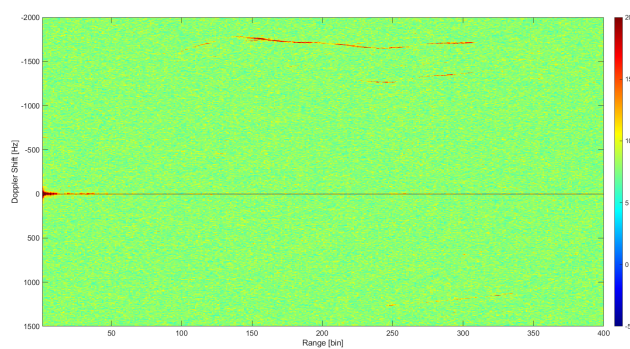


(c) Cumulative RD maxima

Figure 6.20: Video ground truth of an instant of the measurement in scenario in the vicinity of M-121 (a), its corresponding RD map (b) and the cumulative of RD maxima (c).
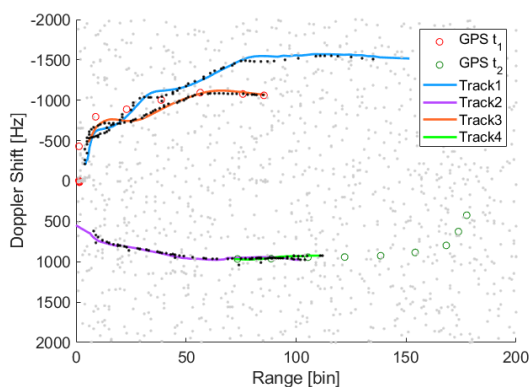


(a) Nursing School
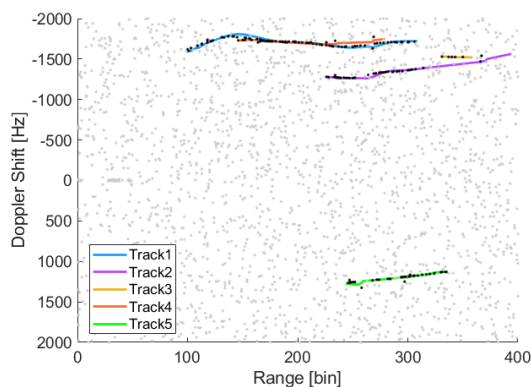


(b) M-121

Figure 6.21: Maps of cumulative detections at the output of CA-CFAR, tracker tracks with its associated detections marked and gps ground truth (only for first scenario).

# Chapter 7

# Study of Array Geometries with Commercial elements for DVB-S based PR

Targets angle of arrival estimation is an important capability in PR, because allows to locate them within the area of interest. In Section 6.1 a multi-beam reflectarray was proposed providing the possibility of angle estimation through amplitude-comparison monopulse techniques. An alternative for achieving angular location of targets is the employment of an array of antennas and DoA processing techniques.

The objective of this chapter is to study the potential performance of an array composed of commercial elements for DVB-S based PR. The main issue concerning this objective is that the size of commercial antennas at X-Ku band frequencies is usually electrically big, causing the appearance of grating lobes for relatively small steering angles.

## 7.1  Commercial elements

A low-cost commercial single element composed of a horn antenna and a Low Noise Block (LNB), to downconvert to intermediate frequency that the USRP X310 board is able to digitalize, is selected. It is commercialized joint with a Bias-Tee, for feeding the LNB, with 10 MHz clock input for synchronization purposes (Figure 7.1). This group operates in DVB-S frequency band employing a local oscillator of 9750 MHz with LNB conversion gain greater than 50 dB, switching horizontal or vertical polarization [170].

The commercial element antenna is an axially corrugated conical horn that has been disassembled to measure its parameters (Figure 7.2(a)). Its maximum diameter is 50.5 mm but with the protection radome it increases up to 60 mm. The horn has been modelled in ANSYS HFSS to characterize its radiation pattern (Figure 7.2(b)). The simulation results shows that it achieves a maximum realized gain of 13.9 dBi with a symetrical HPBW= 38.4° in both E and H planes (Figure 7.2(c)).
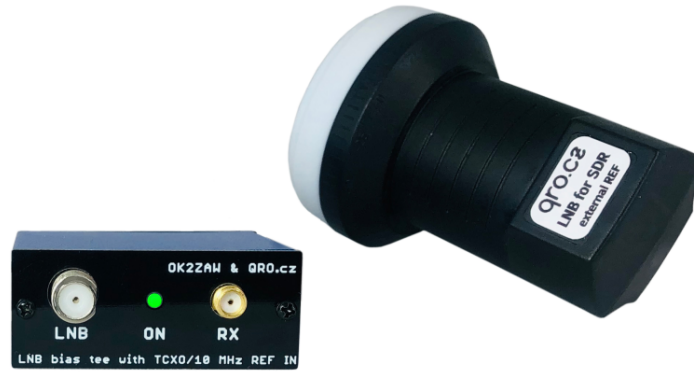
Figure 7.1: Commercial block including horn, LNB and bias-tee for feeding.



(a) Real antenna　　　　　(b) Antenna model　　　　　(c) Radiation pattern
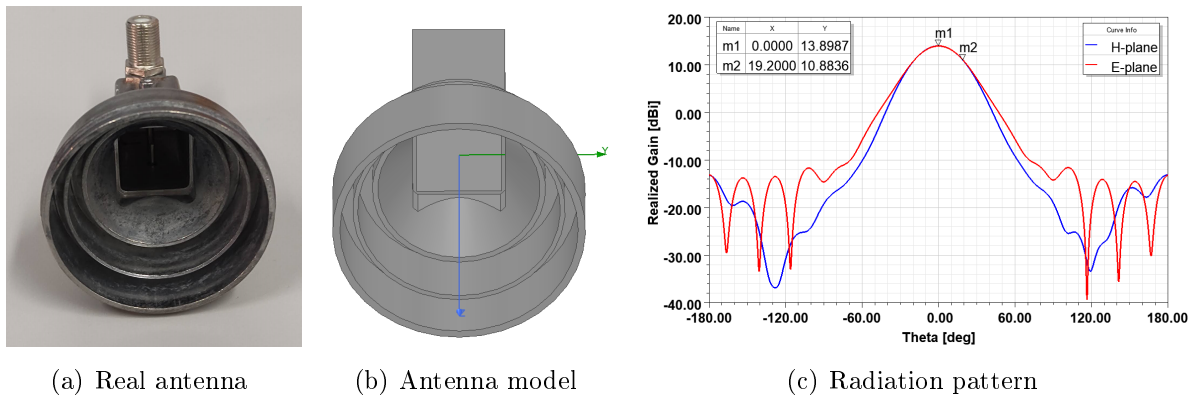
Figure 7.2: Characterization of commercial axially corrugated conical horn by modelling it in ANSYS HFSS.

## 7.2　Linear Array

The size of commercial antenna with radome is 60 mm which at 11 GHz is equal to $2.2\lambda$. The maximum radiation pattern of a linear array depends on the inter-element spacing and the angle of steering (Equation 2.19). Due to periodic repetition of sinusoidal function every $2\pi$, for a given phase distribution $\beta$ for steering angle $\theta_0$, ambiguities or grating lobes will appear at angles $\theta = \arcsin\left(\dfrac{m \cdot 2\pi + \beta}{kd}\right)$, for all $m = \pm 1, \pm 2, \ldots$ in which the arcsin function have a real solution. Table 7.1 summarizes the angles in which the first ambiguities will appear as a function of steering angle for a linear array with separation $d = 60$ mm at 11 GHz. According to this results, if the steering margin is set such as $\theta_0 \leq \pm 12°$, the grating lobes will occur out of the defined margin, so DoA ambiguity can be avoided.

Table 7.1: Position of grating lobes for different steering angles for a ULA with interelement spacing $d = 2.2\lambda$.

| Steering | Grating Lobe 1 | Grating Lobe 2 |
|:---:|:---:|:---:|
| 0° | −27° | 27° dB |
| 5° | −21.4° | 33° dB |
| 10° | −16° | 39.3° dB |
| 12° | −14° | 41.9° dB |
| 15° | −10.9° | 46.08° dB |

## 7.2.1 3-elements ULA: simulation and validation

In a first approach to the employment of these commercial elements, a ULA of 3 antennas is implemented. The objective is to validate the designed ULA as surveillance antennas of IDEPAR demonstrator based on DVB-S IoOs.

A 3-elements ULA with inter-element distance equal to the size of the antenna with radome ($d = 60$ mm) was simulated employed the model of the antenna created in ANSYS HFSS (Figure 7.3(a)). It was simulated at 11.3 GHz, and simulation results, showed in Figure 7.3(b), confirm the theoretical study carried out in Table 7.1: for steering angle $\theta_0 = 12°$ the grating lobe appears at 13.5° reaching almost the same directivity level than main desired lobe, so the steering margin to estimate DoA must be limited to $\theta_0 \in [-12°, +12°]$. The beamwidth, which defines the angular resolution, is around 7.7°, the maximum directivity is 18.6 dBi and SLL without considering the grating lobe is 8.3 dB in the worst case ($\theta_0 = 12°$).



(a) Array modelled in ANSYS          (b) Array azimuth radiation pattern
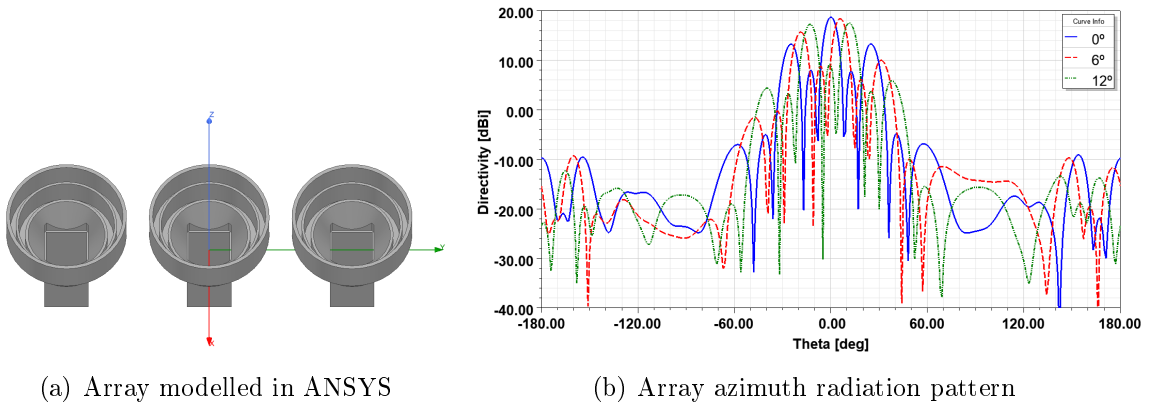
Figure 7.3: Simulation of an ULA of 3 axially corrugated conical horns for three posible steering angles $\theta_0 = \{0°, 6°, 12°\}$.

This array was also employed in the trials campaign developed for validating the designed reflectarray antenna in Scenario 2 (Figure 7.4(a)). Both surveillance antenna systems, reflectarray and horns array, were operating simultaneously, for comparison pur-

poses. The same acquisition than the one presented in Section 6.3.1 is analysed here. Observing the map of cumulative detections and tracks (Figure 7.4(b)) it can be seen that the detection probability is worse than in reflectarray case (Figure 6.21(b)) and therefore also tracking performance is worse: track one and two of actual results has less detected points than in reflectarray case and two valid tracks, one of a target approaching and one moving away, now do not have enough detected points to be validated and associated. The tracks 3 and 4 represent two targets approaching and slowing down, while rest of tracks around zero-doppler cannot be associated with targets. The results of DoA estimation with the 3 horns array is shown in Figure 7.4(c), probing that targets are located pretty good in the roads, despite only employing 3 elements, if the DoA margin is limited to avoid ambiguities ($\mid \theta_0 \mid \leq 12°$). Some ambiguities are yet appreciated showing points that give angles in the limits of the steering margin (blue lines).



(a) PR system deployment in scenario 2        (b) Cumulative detections and tracker tracks        (c) DoA estimation of valid tracks represented over Google Earth
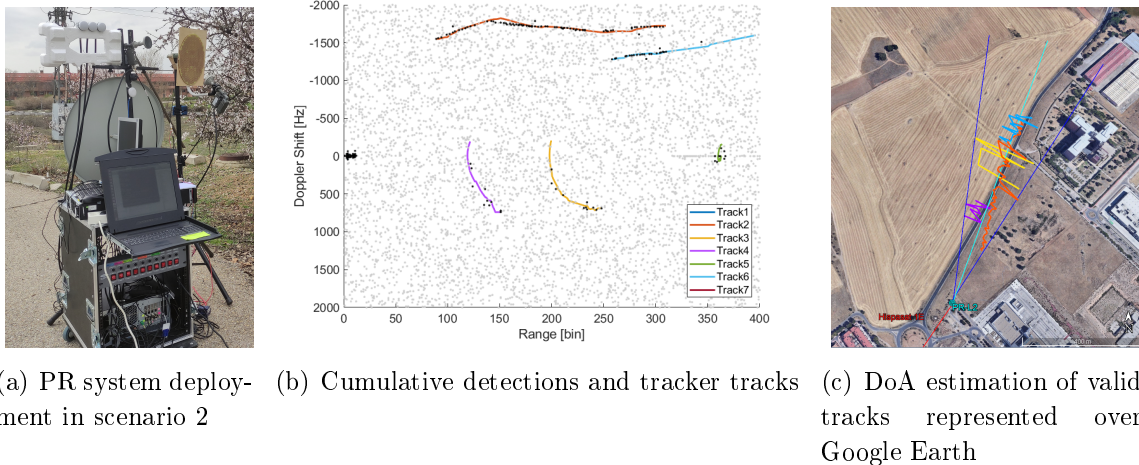
Figure 7.4: Validation results of the 3 commercial horns array through PR trials in Scenario 2 (Section 3.4.1.2).

## 7.2.2   7-element ULA: simulation results

After validating the suitability of this element for PR radar operation, 4 more elements were acquired. An array of 7 elements will improve detection as a higher gain will be achieved and tracking performance by improving angular resolution.

A 7-elements ULA with inter-element spacing $d = 60$ mm has been simulated. The results show that the maximum directivity is improved up to 22.3 dBi, the SLL is also increased up to 12.2 dBi and the beamwidth is reduced to 3.2°. The problem with the grating lobes remains the same than in the case of 3 elements, so the steering angles range must be limited to $\mid \theta_0 \mid \leq 12°$ (Figure 7.5).
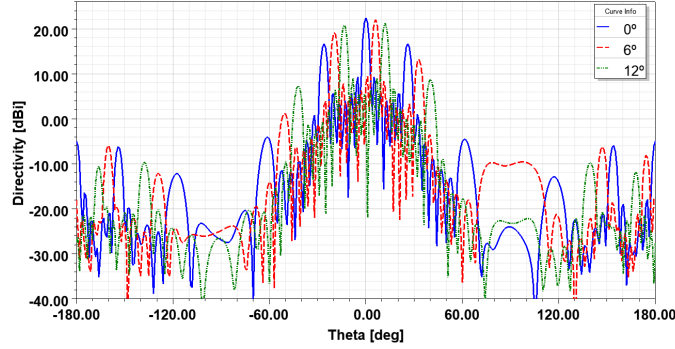
Figure 7.5: Simulation of an ULA of 7 axially corrugated conical horns for three possible steering angles $\theta_0 = \{0°, 6°, 12°\}$ at 11.3 GHz.

## 7.3 Planar array

Due to the size of the single radiating element, grating lobes could not be avoided in linear array geometries. This section is intended to study the potential of a planar array of commercial elements for DVB-S based PR, mainly for increasing the range of steering angles in which grating lobes will not cause ambiguities in DoA estimation.

In a planar array located in XY plane, the array factor (Equation 2.17) is calculated by detaching the inter-element distance in its components $d_x$ and $d_y$. Taking advantage of this fact the inter-element distance in one dimension can be decreased by locating elements between others, where there could not be physically, but in different position of the opposite dimension. As an example, two elements are located along X dimension with the inter-element distance $d_x$ equal to its size, if a third element is located in the middle of these two in X but in different Y position, the new inter-element distance $d_x$ between those elements is half the previous one.

Applying this basis, a planar array is designed by allocating the 7 elements in two linear arrays along X dimension, of 3 and 4 elements respectively. The centre of each element of one array is faced against the centre of inter-element spacing from the other array (Figure 7.6). The inter-element distances are: $d_x = 30.5$ mm and $d_y = 58$ mm. In this way, it is expected to avoid grating lobes in a wider range of steering angles in the azimuth plane (X-axis), as the inter-element spacing is around $1.15\lambda$ at 11.3 GHz.

The simulation results show that the main beam can be steered in azimuth plane in all the angles within the single element HPBW $\mid \theta_{0_a} \mid \leq 19°$ avoiding ambiguities due to grating lobes in that angular margin. For $\theta_{0_a} = 18°$ the grating lobe level becomes greater than SLL but it remains further, at around $-33°$ (Figure 7.7). The angular resolution worsens with respect the 7-elements ULA, as the aperture length in X-dimension decreases, being the beamwidth 6.2°. The maximum directivity achieved is 22.2 dBi and the SLL in the worst case ($\theta_{0_a} = 18°$) is 10.5 dB. For comparing in same conditions with respect the ULA array, the SLL for $\theta_{0_a} = 12°$ is 11.6 dB.

Besides the improvement of avoiding grating lobes in a wider azimuth steering range,
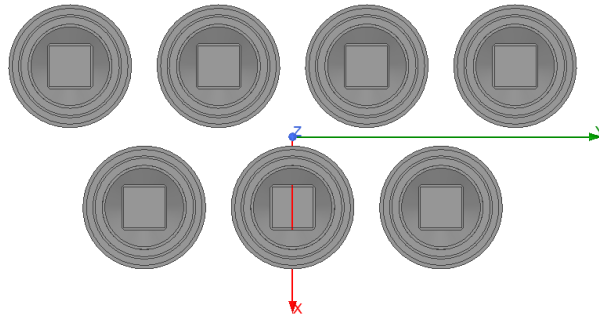
Figure 7.6: Model of proposed planar array to decrease the inter-element distance in X dimension.
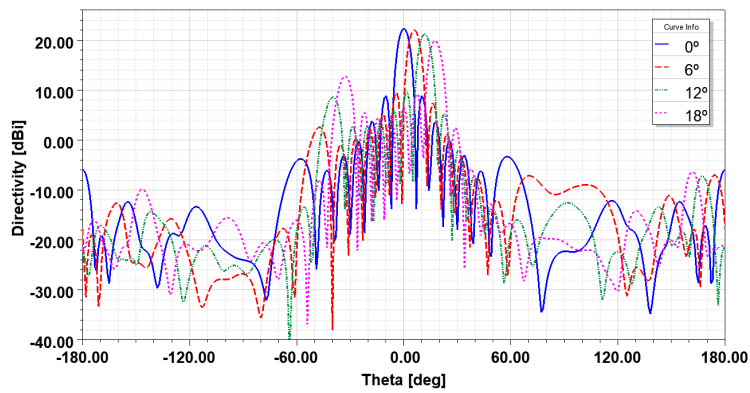


Figure 7.7: Azimuth radiation pattern of proposed planar array for steering angles $\theta_{0_a} = \{0°, 6°, 12°, 18°\}$ at 11.3 GHz.

the planar array also provides the capability of beam steering in the elevation plane. Due to the spacing in Y dimension, and the reduced number of elements in it, only two, the performance for DoA estimation in elevation is expected to be poor. Figure 7.8 shows the elevation cut for steering angles $\theta_{0_e} = 0°$ and $\theta_{0_e} = 13°$. It is proved that the beamwidth is 12.5° with a low difference between main beam and SLL. For steering $\theta_{0_e} = 13°$ there is a symmetrical grating lobe with respect to 0° that will cause ambiguities, but in the particular case of a passive radar in which the receptor is near to the ground surface, that ambiguities can be left out considering that a target cannot be below the ground. The planar array provides the possibility of steering to aerial and terrestrial targets simultaneously, by the application of beamforming techniques.
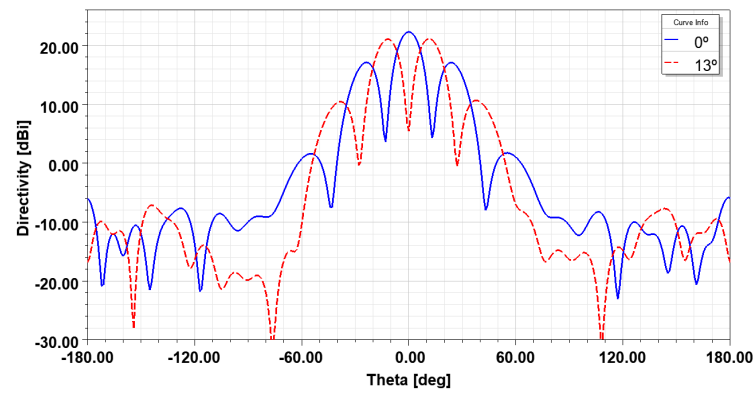
Figure 7.8: Elevation radiation pattern of proposed planar array for steering angles $\theta_{0_e} = \{0°, 13°\}$ at 11.3 GHz.

# Part IV

# Conclusions and Future research lines

# Chapter 8

# Conclusions

This PhD Thesis is the result of an intense research activity focussed on improving detection and tracking capabilities of passive radars in two different but closely related research lines that impact system performance: simulation of bistatic radar scenarios focusing on the modelling of the bistatic Radar Cross Section fluctuations of targets of interest as they move along trajectories, which are related to the movement capabilities of the targets and their objectives; radiating elements and array antennas for fulfilling design and performance requirements defined by passive radars, closely related to those defined by active ones, but making use of illumination signals non designed for detection purposes, and operating at frequencies different from the typical ones used in radar.

Objective scenarios have been analysed considering different types of illumination signals (terrestrial and satellite), which define specific radar geometries and design requirements. Ground, maritime and aerial targets have been considered, paying special attention to low reflectivity and slow movement ones, such as UAVs or drones. The reflectivity of targets has been modelled through simulation techniques for studying the detection range and, also, for defining the requirements of the antenna systems to improve the PR performance.

Classification of targets has been considered through two different approaches: studying fluctuation of the bistatic Radar Cross Section along the target trajectory and the micro-Doppler signature of rotary movement parts with a detailed study of the response of UAV air-screws and bistatic ISAR images simulation as starting point for design of synthetic databases and classification techniques.

Different antenna systems for the surveillance channel of a PR have been proposed, for exploiting DVB-T and DVB-S signals. Design of single radiating elements and array based solutions has been carried out and their suitability for the considered application has been validated through measurements in anechoic chamber and trials in different real scenarios.

The research work has been mainly carried out in the research group coordinated by Prof. María Pilar Jarabo Amores under two national research projects: MASTERSAT (*MultichAnnel paSsive radar receiver exploiting TERrestrial and SATellite Illuminators,*

TEC2015-71148-R) and KRIPTON (*A Knowledge based appRoach to passIve radar detection using wideband sPace adapTive prOcessiNg*, RTI2018-101979-B-I00); and research contracts funded by the Spanish Ministry of Defence under the framework of the European Defence Agency: MAPIS (*Multichannel passive ISAR imaging for military applications*) and JAMPAR (*JAMmer-based PAssive Radar*).

Two are the main objectives of this PhD Thesis: modelling the relevant signatures of the targets and their variation along the trajectory; design of surveillance antenna systems for passive radars exploiting DVB (terrestrial and satellite) IoOs. The contributions of the research work have the added value of having being designed for a real system and validated using data acquired by the technological demonstrator IDEPAR, developed and updated in the research group under previous projects. The proposed antenna system solutions have been integrated in the surveillance channel of the demonstrator and validated in real scenarios, some of them declared of interest by potential end users (Directorate General of Armaments and Material of the Spanish Ministry of Defence, Spanish National Institute of Aerospace Technology, Spanish Navy).

To achieve the defined general objectives, the research work was divided in different research tasks with specific objectives, that are repeated here for convenience:

- Targets electromagnetic modelling.

- Study of scenarios for different IoO geometries, and surveillance antenna system requirements definition.

- Single radiating element design for DVB-T as IoO.

- Array design for DVB-T as IoO improving SLL and directivity.

- Antenna design for DVB-S as IoO.

- Study of array geometries for DoA estimation in DVB-S based PR.

In the following sections, conclusions associated with each of the different reseacrh tasks are summarized.

# 8.1 Conclusions with regard to targets electromagnetic modelling

Targets electromagnetic characterization refers to the extraction of the properties related to the behaviour of a target when it is illuminated with and electromagnetic wave. In radar systems, targets characterization is achieved by measuring or simulating their RCS. The electromagnetic characterization of targets provides useful information for passive radar concerning different scopes or fields.

In this PhD Thesis, the study of RCS of different targets has been carried out through simulation in ANSYS HFSS. Two different approaches have been proposed considering the electric size of the target: for electrically small targets (size less than $10\lambda$) full-wave electromagnetic simulation is employed; for big targets, which RCS is in optical regime, a multi-bounce rays approach with physical theory of diffraction (PTD) correction is employed.

The study of bistatic RCS of targets following a trajectory, as well that as a function of the bistatic angle $\beta$, has been considered. The modulus of BRCS of targets has been employed to estimate PR coverages. This study allows to define the design requirements for surveillance antennas in terms of gain. As the study provides targets' reflection information in all the angles, it also allows to select better scenarios, geometries or targets trajectories. Besides that, a study of the potential use of targets bistatic RCS fluctuations along the trajectory for feature extraction and target classification has been presented. Special attention has been paid to drones simulation because of the complexity for generating radar images due to their small size.

The complex reflectivity has been employed for simulating bistatic inverse synthetic aperture images. It has been proved that this simulated images allows to identify the shape of the target and the distance between dominant scatterers, which could be used to classify targets as a function of their size. This images could be used to design and train a classification stage after detection, that employs image processing techniques for feature extractions joint with adaptive classification techniques such as neural networks.

Finally, the micro-Doppler signature of the air-screws of small unmanned aerial vehicles has also been studied with classification purposes. Radar simulations employing HFSS were carried out to model the Doppler components due to the air-screws movement. It was proved that the maximum Doppler frequency of those replicas has a direct relation with the size of the blades, the rotation speed and the bistatic geometry.

# 8.2 Conclusions with regard to the study of PR scenarios

Passive radar scenarios centred in different locations have been studied considering terrestrial and satellite IoOs. The main aim of these studies is to define the requirements

related to radiation pattern of antenna systems for the PR demonstrator:

- The geometry of each scenario and the possible area of interest was studied to define requirements in terms of beamwidth for surveillance antennas.

- The study of possible trajectories of targets in each of the selected scenarios, or possible bistatic angles if the targets can follow free trajectories, in combination with the knowledge of IoO transmitted power and system sensitivity, has allowed to define antenna gain requirements. Coverage curves in all scenarios were presented as a function of target BRCS.

For DVB-T scenarios, a single radiating element with around 80° of azimuth beamwidth provides enough angular coverage of the area of interest. An antenna of 6 dBi of maximum gain, will lead to a 7-elements array with a gain of at least 14.4 dBi, that will provide coverages between 1 and 2 km for small UAVs, around 7 km for small ground targets, 10 km for medium size ships and 13 km for planes.

In the case of employing satellite illuminators (DVB-S) with ground targets, an azimuth beamwidth of $8° - 10°$ was defined for being able to detect and track targets during some seconds. An antenna gain of 20 dBi was defined for being able to detect cars, in the proposed scenario, at a distance of 600 m far from the PR.

## 8.3 Conclusions with regard to the design of a single radiating element for DVB-T as IoO

Nowadays, DVB-T transmitters are widely employed as IoOs for PR due to its wide bandwidth, high and stable transmitted power and high availability.

The design of single radiating elements suitable for linear array formation has been considered taking into consideration that DVB-T signals can be horizontally or vertically polarized, as it is done in different European countries. An antenna for each polarization has been designed employing different techniques for bandwidth enhancement and radiation pattern improvement, specially the reduction of back radiation. The joint of some techniques available in the literature, studied and optimized for the considered application, with some novel ones allowed to achieve the challenging requirements imposed by the passive radar and array formation. Both antennas have been designed through simulation methods, characterized through measurements in anechoic chamber and validated in PR trials in real scenarios.

The antenna designed for vertical polarization consists of an E-shape patch fed by coaxial probe through a thick air substrate and a novel technique called boxed-ground. It achieves an impedance bandwidth of 150 MHz $(650 - 800$ MHz$)$ with a maximum gain of 6.7 dBi and HPBW of 84° and 56°, for E and H planes respectively, at 740 MHz.

Regarding the antenna for horizontal polarization, a circular patch modified with an slot has been built in over a thick air substrate, for improving the bandwidth. The feeding

is applied by aperture coupling technique through an H-shape slot. An study of different shape reflectors has been carried out selecting a boxed shape one for optimizing radiation characteristics. This antenna provides a wide bandwidth of 220 MHz ($581 - 801$ MHz), which means more than 30% of fractional bandwidth. In terms of radiation, it achieves an stable gain of around 6.5 dBi in all the band with HPBWs of 90° and 70° for E and H planes, respectively, at 740 MHz. It has appropriate dimensions for a linear array design for the surveillance channel of IDEPAR demonstrator employing DVB-T horizontally polarized signal.

## 8.4 Conclusions with regard to the design of an Array for DVB-T as IoO improving SLL and directivity

The employment of non-uniform distances in a linear array (NULA) provides some advantages in terms of directivity and SLL with respect uniform ones. In this thesis a method has been proposed that estimates the best distribution of inter-element spacing employing an optimization algorithm to maximize directivity and SLL. The method proposed employs the real radiation pattern of each element including coupling effects. It has been proved that there are small difference in the pattern of all non-edge elements but the two in the edges change significantly their radiation properties. Taking this into consideration, a method to reduce the required simulations has been proposed, and therefore the computational cost, for characterizing the pattern with coupling effects of the elements forming the array as a function of the distance to their neighbours.

The element proposed for horizontal polarization has been employed to design a 7-element NULA array. The coupling effects between elements have been characterized by simulation in ANSYS HFSS employing the proposed method that reduces the computational cost. The designed array improves the SLL almost 2 dB with respect to the case when the coupling effects were not included in the inter-element distances optimization process. The employment of the proposed element generates a gain 1.5 dB higher than the gain provided by the same array designed with commercial Televes 4G Nova. The final design achieves a maximum gain of 15.2 dBi, maintaining the SLL 13.6 dBi below the maximum in the worst case.

The proposed 7-elements NULA has been built in and integrated in the surveillance channel of IDEPAR v3 demonstrator. PR trials have been carried out in different scenarios. The trials with terrestrial, maritime and aerial targets have proved the suitability of the proposed array for PR systems and have shown an improvement in PR capabilites. Detection capability has improved till the point of being able to detect ground targets at distances of 5 km far from the PR, ships at 11 km and planes at 27 km. This improvement is due to, in part, the high gain achieved with the array and also to a couple of facts that shows a reduction of CAF background level: an improvement in matching with respect to commercial elements, that is traduced to a better noise figure, and the

fact that antenna operation is centred in the desired band, filtering out the signal coming from contiguous frequency, for example LTE mobile communications. The improvement in angular resolution and discrimination with the 7-elements NULA reducing SLL has provided an improvement in tracking stage and has assisted to the development of 3D tracking algorithms.

## 8.5 Conclusions with regard to the design of an antenna operating in X/Ku band for the employment of DVB-S as IoO

Satellite IoOs are under intense research due to the advantages that they present such as high availability, immunity against natural disasters and human attacks and the possibility of generation of ISAR images for target classification purposes as their high frequency and bandwidth assist to this task. The main drawback of this system as IoO is also related to the high frequency combined with the long way from the satellite transmitter to the target, that involves high propagation losses.

The commercial solutions for this system are parabolic dish antennas that provide high gain but a narrow pencil beam. This radiation pattern limits seriously the angular coverage of the PR or need a precise mechanical steering system to be able to follow targets for detecting during the required time for tracking them and, if it is the case, to generate an ISAR image with enough resolution for providing useful information about the target.

In this PhD thesis two solutions based on reflectarray antennas have been proposed to tackle the challenging requirement of achieving a high gain antenna with broad beamwidth, to allow detecting and tracking targets despite the high propagation losses.

The first proposal is a multi-beam reflectarray achieved by multi-feed. The design employs two WR90 E-plane horns and rectangular patches. The phase shift of the patches has been characterized as a function of width and length, through unit cell simulation. The main contribution is the estimation, through optimization, of the best position of each beam to minimize the difference between the phase distribution associated to each steering from each feed. The steering of each beam is adjusted to achieve two contiguous beams that increases the angular coverage through its sum pattern, and also provides the possibility of DoA estimation applying amplitude comparison monopulse technique. This solution has been characterized through simulation in ANSYS HFSS with a design of $54 \times 54$ cm$^2$, that achieves a maximum gain of 25.8 dBi with HPBW of 8.2° in azimuth plane and 3.6° in elevation one.

The second proposal consists of achieving a sectorial beam employing only one feed. An optimization method for reflectarray design has been presented based on the fact that several contiguous beams located at specific positions forms a sectorial one. In

this way, the optimization search estimates the best steering of N beams to achieve the required sectorial beam defined by a mask. The cost for optimization function computes the maximum directivity and the mean SLL in the 2D UV space out of the main beam. The proposed method has been employed to design a $37 \times 27$ cm$^2$ aperture employing commercial elements for the feed, feed-arm and aperture holding structure. A prototype of this design has been manufactured and measure in anechoic chamber showing the achievement of an stable realized gain of 19 dBi along almost all the DVB-S band with sectorial beam of $8.7° \times 5.2°$. This prototype has been employed for PR trials in two scenarios, validating it for this application as terrestrial targets at distances up to 600 m far away from the PR has been detected. The design method has been employed to proposed alternative solutions employing a bespoken feed and without the dimensions restriction imposed by the commercial element. Simulation of new designs has proved that a $81 \times 61$ cm$^2$ aperture, distributing the patches following an hexagonal lattice instead of rectangular can achieve an azimuth beamwidth of $9.6°$ maintaining a maximum realized gain of 24.8 dBi. If the size is increased to 1.1 m in the maximum dimension of the aperture the gain can be enhance up to 28.4 dBi reducing the azimuth beamwidth to $7.4°$.

## 8.6 Conclusions with regard to the study of array geometries in DVB-S based PR

Finally, it has been studied the feasibility of commercial elements composed of horn antenna plus LNB as single radiating element in array geometries. The main issue for this task is that the diameter of the aperture with the protective radome is more than $2\lambda$ in all the DVB-S band. The antenna of those elements has been modelled in the electromagnetic simulator to study the array performance.

In a first attempt, a linear array of 3 elements was formed up and employed in PR trials, probing that detection performance is a bit worse than in the reflectarray case and that the steering margin must be limited to $\pm 12°$ to avoid ambiguities due to grating lobes.

To deal with ambiguity problems due to the size of the antennas a planar geometry is proposed taking advantage of the fact that the centre position of each element in one dimension, for steering in one plane, can be reduced if they are translated in the opposite dimension. In this way a 7 element planar design has been proposed, achieving a maximum directivity of 22 dBi and avoiding grating lobes in within the beamwidth of the antenna, so the beam could be steered to $\pm 19°$.

# Chapter 9

# Future Research Lines

During the research carried out in this PhD thesis and from the knowledge acquired with it, different ideas and areas of further research have been identified.

## 9.1 Update single radiating element for DVB-T as IoO

By the third term of 2020 the second digital dividend were completely applied in Spain, keeping the 700 MHz band free for employing it in mobile services. Therefore, from then, the DVB-T band remains from 482 MHz to 694 MHz.

The *C-H$_a$ Antennas* designed in this thesis, which are being employed in the surveillance channel of IDEPAR demonstrator for PR trials in Spain, achieve a value of the reflection coefficient below $-10$ dB from 581 MHz. Even though some PR measurements has been realized at 540 MHz achieving good results, it is highly recommended to employ antennas with good matching in all the frequency band.

So, for this reasons, near future research must be oriented in the adjustment or redesign of the single radiating element for covering the new DVB-T band. The method proposed for estimating the best inter-element spacing could be employed with the new element, to design a NULA for updating the surveillance channel of IDEPAR demonstrator.

## 9.2 Design of new array geometries

In this PhD thesis, mainly linear array geometries have been studied. In DVB-T case, an L-shape array with six element in the horizontal plane and one below the first one has been employed to allow the DoA estimation in both azimuth and elevation planes. For DVB-S a planar array with commercial elements has been proposed to broaden the steering margin free of grating lobes.

Further research can be done in planar geometries, trying to design a method that can optimize the steering in both planes and the radiation pattern characteristics: directivity

and SLL. The method could be based in an extension of the one proposed for non-uniform linear array, estimating the positions of each element in a 2D plane.

Also, sparse array techniques can be explored to the design of new array geometries that improve the performance of IDEPAR demonstrator working woth both type of IoOs: DVB-T and DVB-S.

## 9.3   Study and research of antenna systems for new IoOs

Recently, trials with IDEPAR demonstrator employing GPS system as IoO has proved the feasibility of detection of small terrestrial targets. The main characteristic of GPS signals is that its level is below noise, so a more complex processing must be carried out to be able to detect faint target echoes in that conditions. During the trials, which were made with typical hemisphere GPS active antennas, cars were detected up to some tens of meters from the PR. The hemisphere antenna causes the acquisition of too much clutter and even direct signal from different GPS satellites, which limits the detection capability. Future research in directive circularly polarized antennas in GPS band or even array geometries, for the surveillance channel of IDEPAR employing GPS as IoO, is expected to enhance the performance providing more versatility and availability to the PR system as GPS has worldwide coverage.

The new 5G mobile communications could be appropriate for passive radars. This system is characterized by frequency sparsity that can also be really useful for PR: the 700 MHz band can be employed for detecting and tracking distant targets while the higher frequency bands, 3.5 GHz and 26 GHz, can be used for high resolution passive ISAR images generation. The design of antennas systems for employing 5G technology as IoO will be a challenging and interesting task leading to a intense research to tackle the frequency sparse characteristics through multi-band antennas or multiple antennas, as well as the different radiating patterns required for each of the mentioned uses of each band. A wide angular coverage must be desired in the low frequencies while directivity and gain will be the main focus in K-band.

## 9.4   Follow on targets classification approaches through targets electromagnetic characterization

In this thesis, different approaches have been proposed for targets classification based on the study of their electromagnetic characteristics, mainly the RCS. The work on those topics must follow on:

A. In the case of targets classification through their BRCS along a trajectory, the simulation process must be refined including the pitch and roll attitude parameters

in each point of the trajectory. Actually only yaw angle is considered for every point, while a representative value in each trajectory is selected for pitch and roll. Simulations of more targets and, what is more important, more real trajectories with different targets must be analysed to validate the potential of this approach for the interesting task of drones classification.

B. For following in ISAR image topics for classification, a great database of simulated images must be generated, considering several targets of different types and numerous images for all possible aspect angles. Different techniques for characteristics extraction from the images should be studied to design a good classifier. Real ISAR images generated from real data acquired with IDEPAR demonstrator will prove the performance of the classifier, as well as check that the simulated images generated with the proposed method in this thesis are worth.

## 9.5 Implementation of adaptive beamforming and DoA algorithms

Actual version of IDEPAR demonstrator is employing orthogonal beams with maximum directivity weights for detection stage while DoA estimation is based in a conventional beamforming generating beams which are swept to the angles defined within the surveillance margin, to search for signal peaks in the direction of the targets.

To improve detection stage, a first study generating nulls in the position of the IoO, other interference transmitters or powerful clutter, such as buildings should be done. The research of different adaptive beamforming techniques to maximize target echoes SNR or minimize the background clutter or noise will also improve targets detection.

In the same way, the previously studied adaptive beamforming techniques for stage one, will also improve DoA performance by employing those optimum weights instead of conventional one for sweeping the beam in all the angle within the surveillance margin. IDEPAR processing applies the DoA estimation in a second stage after detection, and only in the Range-Doppler cell where a detection or a valid track has been declared. Following this approach and assuming that in each RD cell only a target can be present, the employment of subspace based algorithms, such as MUSIC or ESPRIT, can be studied to improve targets localization accuracy. The validity of the assumption that only a target is present at a RD cell must be studied for each scenario, objective targets and considering the resolution of the PR system in both dimensions.

# Chapter 10

# Related contributions

In this chapter, author's contributions related to the PhD thesis are presented. These contributions were published in different journals and conferences at both, international and national levels.

## 10.1  Contributions directly related to this PhD Thesis

### 10.1.1  Journal papers

1. **Design and Validation of a Reflectarray Antenna with Optimized Beam for Ground Targets Monitoring with a DVB-S based Passive Radar**. Authors: Javier Rosado-Sanz, M. Pilar Jarabo-Amores, Jean-Yves Dauvignac, David Mata-Moya, Jérôme Lanteri, Claire Migliaccio; Sensor (MDPI), Delivered June 2021. (Journal citation report (JCR) impact factor: 3.275 (Quartile Q1)).

2. **Broadband modified-circle-shape patch antenna with H-aperture feeding for a passive radar array** [149]. Authors: Javier Rosado-Sanz, Maria-Pilar Jarabo-Amores, David Mata-Moya, Pedro-Jose Gómez-del-Hoyo, Nerea Del-Rey-Maestre; Aerospace Science and Technology (Elsevier), Vol. 110, March 2021 (Journal citation report (JCR) impact factor: 4.499 (Quartile Q1)).

3. **Passive Radar Array Processing with Non-Uniform Linear Arrays for Ground Target's Detection and Localization** [135]. Authors: Nerea Del-Rey-Maestre, David Mata-Moya, Maria-Pilar Jarabo-Amores, Pedro-Jose Gómez-del-Hoyo, Jose-Luis Bárcena-Humanes, Javier Rosado-Sanz; Remote Sensing, Vol. 9, Issue 7, paper 756, July 2017 (Journal citation report (JCR) impact factor: 3.408 (Quartile Q2)).

4. **IDEPAR, uso del radar pasivo para la detección de drones** [134]; Authors: M.P. Jarabo Amores, D. Mata Moya, N. Rey Maestre, P.J. Gómez del Hoyo, J.

Rosado Sanz, <u>National Journal</u>: Boletín de Información Tecnológica en Defensa, No. 61, Segundo Trimestre, 2019.

## 10.1.2    Specialists' Meetings and workshops.

1. **Modelling of Drone Bistatic RCS Fluctuations for UHF Passive Radar Scenarios Simulation.** In NATO MSG-SET-183 Specialists' Meeting on "Drone Detectability: Modelling the Relevant Signature [143].

2. **Passive radar distributed sensor network for detecting silent aerial and maritime targets in coastal waters.** Authors: M.P. Jarabo-Amores, David Mata-Moya, N. ,del Rey-Maestre, P. Gómez-del Hoyo. In NATO SET-284 Specialists' Meeting on Enhanced Situation Awareness using Active-Passive Radar Systems in Military Scenarios [171].

3. **DVB-S based passive radar for ground targets detection and tracking.** Authors: Pedro Gómez-del-Hoyo, Maria-Pilar Jarabo-Amores, David Mata-Moya, Javier Rosado-Sanz, Nerea Del-Rey-Maestre. In the 7th PCL Focus Days 2019 (Invited) [172].

## 10.1.3    Conference contributions

1. **High Gain Sectorial Beam Reflectarray Design for DVB-S Passive Radar through Multi-Beam Optimization.** Authors: J. Rosado-Sanz, M. P. Jarabo-Amores, D. Mata-Moya, J. Y. Dauvignac, J. Lanteri and C. Migliaccio; 2020 23rd International Microwave and Radar Conference (MIKON), 2020, pp. 361-366, [165] (DOI: 10.23919/MIKON48703.2020.9253846) 5-7 Oct. 2020.

2. **On the Impact of Drone Airscrews Signature on Passive Radar Detection and Tracking Stages.** Authors: Jarabo-Amores, M.P.; Mata-Moya, D.; Gómez-del-Hoyo, P.; del Rey-Maestre, N.; Rosado-Sanz, J.; In IEEE Radar Conference 2020 [173] Oct. 2020 (Invited contribution).

3. **DVB-S Passive Radar Performance Evaluation in Semi-Urban Ground Scenario.** Authors: J. Rosado-Sanz, M. P. Jarabo-Amores, D. Mata-Moya, N. del-Rey-Maestre and A. Almodóvar-Hernández; 2020 21st International Radar Symposium (IRS), 2020, pp. 232-235, [17]
(DOI: 10.23919/IRS48640.2020.9253838) 5-7 Oct. 2020.

4. **Contoured-beam reflectarray for improving angular coverage in DVB-S passive radars.** Authors: J. Rosado-Sanz; M.P. Jarabo-Amores; D. Mata-Moya; P.J. Gómez-del-Hoyo; N. Del-Rey-Maestre; 2019 20th nternational Radar Symposium (IRS2019) [160], pp. 1-8, 26-28
(DOI: 10.23919/IRS.2019.8768107), June 2019.

5. **Advantages of non-uniform linear arrays based on COTS elements in passive radar applications.** Authors: J. Rosado-Sanz, N. Rey-Maestre, D. Mata-Moya, M. P. Jarabo-Amores, M. Rosa-Zurera and J. L. Bárcena-Humanes; 2018 22nd International Microwave and Radar Conference (MIKON), 2018, pp. 199-203, [151] (DOI: 10.23919/MIKON.2018.8405177).

6. **Conductivity Estimation of Composite Materials Used on UAV Airframes** Authors: J. Rosado-Sanz, M. Jarabo-Amores, D. Mata-Moya, P. Gomez-del-Hoyo and M. Benito-Ortiz; 2018 IEEE Conference on Antenna Measurements & Applications (CAMA), 2018, pp. 1-4, [174]
(DOI: 10.1109/CAMA.2018.8530642).

7. **Design of a Broadband Patch Antenna for a DVB-T based Passive Radar Antenna Array.** Authors: J. Rosado-Sanz, M.P. Jarabo-Amores, D. Mata-Moya, N. del-Rey-Maestre, P. Gomez-del-Hoyo; 17th IEEE International Conference on Ubiquitous Wireless Broadband [153], pp. 1-5, 12-15 Sept. 2017. **Awarded as best student paper.**

8. **Validation of a Broadband E-shaped Antenna in a Real Semi-Urban Passive Radar.** Authors: J. Rosado-Sanz; M.P. Jarabo-Amores; P.J. Gomez-Hoyo; N. del-Rey-Maestre; D. Mata-Moya; 42th International Conference on Infrared, Millimeter and Terahertz Waves [175] (DOI: 10.1109/IRMMW-THz.2017.8067172), 27 Aug.- 1 Sep. 2017.

9. **SLL Optimization of Passive Radar Non-uniform Linear Arrays Based on Commercial UHF Antennas**. Authors: J. Rosado-Sanz, M. P. Jarabo-Amores, D. Mata-Moya, N. del-Rey-Maestre and J. L. Bárcena-Humanes; 2017 International Conference on Control, Artificial Intelligence, Robotics & Optimization (ICCAIRO), 2017, pp. 89-92, [176] (DOI: 10.1109/ICCAIRO.2017.27.).

### 10.1.3.1 National conferences and workshops

1. **IDEPAR, radar pasivo basado en TDT, en entornos costeros.** Authors: María Pilar Jarabo Amores, David Mata Moya, Nerea del Rey Maestre, Pedro José Gómez del Hoyo, Javier Rosado Sanz, María de Cortes Benito Ortiz. In the *VII Congreso Nacional de I+D en Defensa y Seguridad (DESEi+d 2019)* [177].

2. **Validación de radares pasivos basados en la TDT para la detección de drones.** Authors: Nerea del Rey Maestre, Pedro J. Gómez del Hoyo, Javier Rosado Sanz, David Mata Moya, M. Pilar Jarabo Amores, Francisco Javier Gaitán Cabanas. In the *Congreso Nacional de I+D en Defensa y Seguridad (DESEi+d 2018)* [178].

# 10.2   Other contributions with some relation to this PhD Thesis

## 10.2.1   Conference contributions

1. **Study of the effect of wideband sparse frequency signals in UHF passive radar resolution.** Authors: Anabel Almodóvar Hernández, M.P. Jarabo Amores, D. Mata Moya, P.J. Gómez del Hoyo, J. Rosado-Sanz, 9th Microwave and Radar Week (MRW2020) 2020, pp. 82-87 [179], (DOI: 10.23919/IRS48640.2020.9253955), 5-7 Oct. 2020.

2. **First Approach on Ground Target Detection with GPS Based Passive Radar: Experimental Results.** Authors: Pedro Gomez-del-Hoyo, María-Pilar Jarabo-Amores, David Mata-Moya, Nerea del-Rey-Maestre, and Javier Rosado-Sanz, Signal Processing Symposium (SPSympo 2019). pp. 71-75 (**1st Price Young Scientist Contest Award**) [19],
(DOI: 10.1109/SPS.2019.8881962), 17-19 Sept. 2019.

3. **Statistical Characterization of DVB-S Bistatic Clutter for Ground Target Detection.** Authors: Nerea del-Rey-Maestre, David Mata-Moya, María-Pilar Jarabo-Amores, Pedro-José Gómez-del-Hoyo and Javier Rosado-Sanz; 16th European Radar Conference (EuRAD 2019) [29], pp. 149-152. 2-4 Oct. 2019

4. **Optimum Beamforming to Improve UAVs Detection Using DVB-T Passive Radars.** Authors: Nerea del-Rey-Maestre; David Mata-Moya; María-Pilar Jarabo-Amores; Pedro-José Gomez-del-Hoyo; Javier Rosado-Sanz; 2019 International Radar Conference 2019 (Invited) [180]
(DOI: 10.1109/RADAR41533.2019.171288), 23-17 Sept. 2019.

5. **Drone detection feasibility with passive radars.** Authors: M. Pilar Jarabo-Amores; David Mata-Moya; Pedro J. Gómez-del-Hoyo; J.L. Bárcena-Humanes; J. Rosado-Sanz; N. Rey-Maestre; M. Rosa-Zurera; 15th European Radar Conference, pp. 313-316, 26-28 Sept. 2018 [146].

6. **First Approach to Motion Compensation Considerations for Passive Radar System Based on GPS Signal.** Authors: J.L Bárcena-Humanes; P.J. Gómez-del-Hoyo; M.P. Jarabo-Amores; J. Rosado-Sanz; M.C Benito-Ortiz; 2018 19th International Radar Symposium (IRS 2018) [181], pp. 1-10, (DOI: 10.23919/IRS.2018.8448032), 20-22 June 2018

7. **Study of the ghost target phenomenon on a real DVB-T passive radar scenario.** Authors: P. Gomez-del-Hoyo; J.-L. Barcena-Humanes; N. del-Rey-Maestre; J. Rosado-Sanz; M. P. Jarabo-Amores; 2017 Signal Processing Symposium (SPSympo) [25] (DOI: 10.1109/SPS.2017.8053683), 12-14 Sept. 2017.

8. **Nondesired Effects in DVB-T Based Passive Radar Due to Sporadic Interference.** Authors: N. del-Rey-Maestre ; J.-L. Bárcena-Humanes ; J. Rosado-Sanz ; P. Gómez-del-Hoyo ; D. Mata-Moya; 2017 Signal Processing Symposium (SPSympo) [182] (DOI: 10.1109/SPS.2017.8053682), 12-14 Sept. 2017.

9. **Coherent VI-MLP-CFAR Detector for IDEPAR Demonstrator (DVB-T passive radar) in Ground Traffic Monitoring.** Authors: N. del-Rey-Maestre, J. Rosado-Sanz, P. Gómez-del-Hoyo, D. Mata-Moya, M.P. Jarabo-Amores; 2017 IEEE International Instrumentation and Measurement Technology Conference (I2MTC) (DOI: 10.1109/I2MTC.2017.7969737) [156], 22-25 May 2017.

10. **DoA Estimation Based on a ULA of Commercial Antennas in Semi-Urban Passive Radar Scenario.** Authors: N. del-Rey-Maestre, D. Mata-Moya, M.P. Jarabo-Amores, J. Rosado-Sanz, P. Gómez-del-Hoyo; 2017 International Conference on Control, Artificial Intelligence, Robotics & Optimization (ICCAIRO) [183], pp. 74-77, 20-22 May 2017.

11. **On the potentials of satellite based passive radars for smart sensors networks in smart cities.** Authors: J.L Bárcena-Humanes; P.J. Gómez-del-Hoyo; M.P. Jarabo-Amores; D. Mata-Moya; J. Rosado-Sanz; IEEE 17th International Conference on Ubiquitous Wireless Broadband (ICUWB17) Smart Cities & Industries [184], (DOI: 10.1109/ICUWB.2017.8250980), 12-15 Sept. 2017.

12. **DVB-T based Passive radar performance sensitivity with respect to channel availability.** Authors: Nerea del-Rey-Maestre; José-Luis Bárcena-Humanes; Javier Rosado-Sanz; Pedro Gómez-del-Hoyo; David Mata-Moya; 14th European Radar Conference (EuRAD 2017) [185] (DOI: 10.23919/EURAD.2017.8249177), 11-13 Oct. 2017.

# Part V

# Bibliography

# Bibliography

[1] N. J. Willis. Bistatic Radar. SciTech Publishing Inc., 2005.

[2] Richard Klemm, Ulrich Nickel, Christoph Gierull, Pierfrancesco Lombardo, Hugh Griffiths, and Wolfgang Koch, editors. Novel Radar Techniques and Applications Volume 1: Real Aperture Array Radar, Imaging Radar, and Passive and Multistatic Radar, volume 1. Institution of Engineering and Technology, 2017.

[3] Mateusz Piotr Malanowski. Signal Processing for Passive Bistatic Radar. Artech-House, 685 Canton Street, Norwood, MA 02062 USA, 2019.

[4] Francesco Fioranelli, Hugh Griffiths, Matthew Ritchie, and Alessio Balleri. Micro-doppler radar and its applications. The Institute of Engineering and Technology (IET), 2020.

[5] A. Farina, P. Holbourn, T. Kinghorn, and L. Timmoneri. Aesa radar — pan-domain multi-function capabilities for future systems. In 2013 IEEE International Symposium on Phased Array Systems and Technology, pages 4–11, 2013.

[6] IEEE. IEEE Standard for Radar Definitions. IEEE Std 686-2017 (Revision of IEEE Std 686-2008), pages 1–54, 2017.

[7] H. Griffiths and N. Long. Television-based bistatic radar. In IEE Proceedings on Comunications, Radar, and Signal Processing, volume 133, pages 649–657, 1986.

[8] P. E. Howland, D. Makisimiut, and G. Reitsma. FM radio based bistatic radar. In IEE Proceedings on Radar, Sonar and Navigation, volume 152, pages 107–115, 2005.

[9] M. Malanowski, K. Kulpa, and J. Misjurewicz. PaRaDe - Passive Radar Demostrator family development at Warsaw University of Technology. Microwaves, Radar and Remote Sensing Symposium, pages 75–78, 2008.

[10] C. J. Coleman, R. A. Watson, and H. Yardley. A practical bistatic passive radar system for use with dab and drm illuminators. In 2008 IEEE Radar Conference, pages 1–6, May 2008.

[11] R. Zemmari, U. Nickel, and W. Wirth. GSM Passive Radar for medium range surveillance. EuRAD, pages 49–52, 2009.

[12] D. Petri, A. Capria, M. Martorella, and F. Berizzi. Ambiguity function study for UMTS Passive Radar. EuRAD, pages 41–44, 2009.

[13] R. Saini and M. Cherniakov. DTV signal ambiguity function analysis for radar applications. In IEE Proc. on Radar, Sonar and Navigation, volume 152, pages 133–142, 2005.

[14] D. W. O'Hagan, M. Schroder, V. Basavarajappa, P. Knott, H. Kuschel, and M. Simeoni. Wideband antenna array for digital video broadcast terrestrial-based passive bistatic radar applications. IET Radar, Sonar Navigation, 8(2):106–113, 2014.

[15] P. Marques, A. Ferreira, F. Fortes, P. Sampaio, H. Rebelo, and L. Reis. A pedagogical passive radar using dvb-s signals. In 2011 3rd International Asia-Pacific Conference on Synthetic Aperture Radar (APSAR), pages 1–4, Sep. 2011.

[16] I. Pisciottano, D. Cristallini, and D. Pastina. Maritime target imaging via simultaneous dvb-t and dvb-s passive isar. IET Radar, Sonar Navigation, 13(9):1479–1487, 2019.

[17] J. Rosado-Sanz, María-Pilar Jarabo-Amores, David Mata-Moya, Nerea del Rey-Maestre, and A. Almodóvar-Hernández. Dvb-s passive radar performance evaluation in semi-urban ground scenario. In 2020 21th International Radar Symposium (IRS), pages 1–4, 2020.

[18] Eamonn Glennon, Andrew Dempster, and Chris Rizos. Feasibility of air target detection using gps as a bistatic radar. Journal of Global Positioning Systems, 5:119–126, 12 2006.

[19] P. Gomez-del-Hoyo, M. Jarabo-Amores, D. Mata-Moya, N. del-Rey-Maestre, and J. Rosado-Sanz. First approach on ground target detection with gps based passive radar: Experimental results. In 2019 Signal Processing Symposium (SPSympo), pages 71–75, 2019.

[20] J.-L. Bárcena-Humanes. Improved Signal Processing Techniques for Passive Radar applications. Design of a technological demonstrator. PhD thesis, University of Alcalá, 2016.

[21] F. Colone, D. W. O'Hagan, P. Lombardo, and C. J. Baker. A multistage processing algorithm for disturbance removal and target detection in passive bistatic radar. IEEE Transactions on Aerospace and Electronic Systems, 45(2):698–722, 2009.

[22] G. Clark, S. Mitra, and S. Parker. Block implementation of adaptive digital filters. IEEE Transactions on Circuits and Systems, 28(6):584–592, 1981.

[23] Y.D. Zhao, Y.K. Zhao, X.D. Lu, and M.S. Xiang. Block nlms cancellation algorithm and its real-time implementation for passive radar. In IET International Radar Conference 2013, pages 1–5, 2013.

[24] Osama Mahfoudia, François Horlin, and Xavier Neyt. Optimum reference signal reconstruction for dvb-t based passive radars. In 2017 IEEE Radar Conference (RadarConf), pages 1327–1331, 2017.

[25] P. Gómez-del Hoyo, J.-L. Bárcena-Humanes, N. del Rey-Maestre, J. Rosado-Sanz, and M.P. Jarabo-Amores. Study of the ghost target phenomenon on a real DVB-T passive radar scenario. In Signal Proc. Symposium, pages 1–6, Sept 2017.

[26] T. Cao, J. Palmer, and P. Berry. False alarm control of CFAR algorithms with experimental bistatic radar data. IEEE Radar Conference, pages 156–161, 2010.

[27] D. Langellotti, F. Colone, P. Lombardo, and M. Sedehi. DVB-T based Passive Bistatic Radar for maritime surveillance. In IEEE Radar Conference, pages 1197–1202, 2014.

[28] N. del Rey-Maestre, M.P. Jarabo-Amores, D. Mata-Moya, J. Rosado-Sanz, and M.C. Benito-Ortíz. Performance of conventional and lr based passive radar detectors in ground traffic applications. In 2018 International Conference on Control, Artificial Intelligence, Robotics Optimization (ICCAIRO), pages 23–26, 2018.

[29] N. del-Rey-Maestre, D. Mata-Moya, M. Jarabo-Amores, P. Gómez-del-Hoyo, and J. Rosado-Sanz. Statistical characterization of dvb-s bistatic clutter for ground target detection. In 2019 16th European Radar Conference (EuRAD), pages 149–152, 2019.

[30] D. Mata-Moya, N. del Rey-Maestre, V.-M. Peláez-Sánchez, M.-P. Jarabo-Amores, and J. Martín-Nicolás. MLP-CFAR for improving coherent radar detectors robustness in variable scenarios. Expert systems with applications, 2015.

[31] P. E. Howland, D. Makisimiut, and G. Reitsma. FM radio based bistatic radar. In IEE Proceedings on Radar, Sonar and Navigation, volume 152, pages 107–115, 2005.

[32] M. Malanowski and K. Kulpa. Analysis of bistatic tracking accuracy in passive radar. In 2009 IEEE Radar Conference, pages 1–6, 2009.

[33] María-Pilar Jarabo-Amores, Jose-Luis Bárcena-Humanes, Pedro-Jose Gomez-del Hoyo, Nerea del Rey-Maestre, Diego Juara-Casero, Francisco-Javier Gaitán-Cabañas, and David Mata-Moya. IDEPAR: a multichannel digital video

broadcasting-terrestrial passive radar technological demonstrator in terrestrial radar scenarios. IET Radar, Sonar and Navigation, pages 1–9, 2016.

[34] A. Farina. Tracking function in bistatic and multistatic radar systems. IEE Proceedings F - Communications, Radar and Signal Processing, 133(7):630–637, 1986.

[35] D. Pasculli and et al. DVB-T passive radar tracking on real data using Extended Kalman Filter with DOA estimation. In 14th Int. Radar Symposium, volume 1, pages 184–189, June 2013.

[36] H. W. Li and J. Wang. Particle filter for manoeuvring target tracking via passive radar measurements with glint noise. IET Radar, Sonar Navigation, 6(3):180–189, 2012.

[37] Victor C. Chen and Marco Martorella. Inverse Synthetic Aperture Radar Imaging: Principles, Algorithms and Applications. SciTech Publishing, 2014.

[38] D. Olivadese, E. Giusti, D. Petri, M. Martorella, A. Capria, and F. Berizzi. Passive isar with dvb-t signals. IEEE Transactions on Geoscience and Remote Sensing, 51(8):4508–4517, Aug 2013.

[39] I. Pisciottano, D. Pastina, and D. Cristallini. Dvb-s based passive radar imaging of ship targets. In 2019 20th International Radar Symposium (IRS), pages 1–7, June 2019.

[40] Pilar Jarabo-Amores, Elisa Giusti, Manuel Rosa-Zurera, Alessio Bacci, Amerigo Capria, and David Mata-Moya. Target classification using passive radar isar imagery. In 2017 European Radar Conference (EURAD), pages 155–158, 2017.

[41] A. De Maio, G. Foglia, N. Pasquino, and M. Vadursi. Measurement and analysis of clutter signal for GSM/DCS-based Passive Radar. IEEE Radar Conference, pages 1–6, 2008.

[42] A. De Maio et al. Measurement and comparative analysis of clutter for GSM and UMTS Passive Radar. IET Radar, Sonar and Nav., 4(3):421–423, 2010.

[43] F. Filippini, F. Colone, and A. De Maio. Threshold region performance of multi-carrier maximum likelihood direction of arrival estimator. IEEE Transactions on Aerospace and Electronic Systems, 55(6):3517–3530, Dec 2019.

[44] A. Aubry, V. Carotenuto, A. De Maio, and L. Pallotta. Localization in 2d pbr with multiple transmitters of opportunity: A constrained least squares approach. IEEE Transactions on Signal Processing, 68:634–646, 2020.

[45] Tom Derham, Shaun Doughty, Karl Woodbridge, and Christopher J. Baker. Realisation and evaluation of a low cost netted radar system. In 2006 CIE International Conference on Radar, pages 1–4, 2006.

[46] S. Alhuwaimel, S. Coetzee, P. Cheng, D. Du Plessis, F. Fioranelli, H. Griffiths, M.R. Inggs, D. Jordan, W. Miceli, D. O'Hagan, R. Palama, S. Paine, M. Ritchie, J.S. Sandenbergh, and A. Stevens. First measurements with nextrad, a polarimetric x/l band radar network. In 2017 IEEE Radar Conference (RadarConf), pages 1663–1668, 2017.

[47] M. Ritchie, F. Fioranelli, K. Woodbridge, H. Griffiths, L. Daniel, A. De Luca, S. Hristov, M. Gashinova, and M. Cherniakov. Simultaneous data collection of small maritime targets using multistatic radar and forward scatter radar. IET Radar, Sonar Navigation, 11(6):937–945, 2017.

[48] Riccardo Palamà, Francesco Fioranelli, Matthew Ritchie, M.R. Inggs, Simon Lewis, and Hugh Griffiths. Measurements of multistatic x l band radar signatures of uavs. In 2019 International Radar Conference (RADAR), pages 1–5, 2019.

[49] Francesco Fioranelli, Matthew Ritchie, and Hugh Griffiths. Bistatic human micro-doppler signatures for classification of indoor activities. In 2017 IEEE Radar Conference (RadarConf), pages 0610–0615, 2017.

[50] A. G. Stove, M. S. Gashinova, S. Hristov, and M. Cherniakov. Passive maritime surveillance using satellite communication signals. IEEE Transactions on Aerospace and Electronic Systems, 53(6):2987–2997, Dec 2017.

[51] L. Daniel, S. Hristov, X. Lyu, A. G. Stove, M. Cherniakov, and M. Gashinova. Design and validation of a passive radar concept for ship detection using communication satellite signals. IEEE Transactions on Aerospace and Electronic Systems, 53(6):3115–3134, Dec 2017.

[52] R. Saini, M. Cherniakov, and V. Lenive. Direct path interference suppression in bistatic system: DTV based radar. In Radar Conference, 2003. Proceedings of the International, pages 309–314, Sept 2003.

[53] Debora Pastina, Fabrizio Santi, Federica Pieralice, Michail Antoniou, and Mikhail Cherniakov. Passive radar imaging of ship targets with gnss signals of opportunity. IEEE Transactions on Geoscience and Remote Sensing, 59(3):2627–2642, 2021.

[54] M. Malanowski and K. Kulpa. Digital beamforming for passive coherent location radar. In IEEE Radar Conf., 2008.

[55] M Malanowski, K. Kulpa, M Bączyk, L. Maślikowski, and E Janas. Passive Coherent Location DBV-T demonstrator at Warsaw University of Technology. 3rd FHR Focus Days on PCL, Wachtberg-Werthhoven, 2011.

[56] Marek Płotka, Mateusz Malanowski, Piotr Samczyński, Krzysztof Kulpa, and Karol Abratkiewicz. Passive bistatic radar based on vhf dvb-t signal. In 2020 IEEE International Radar Conference (RADAR), pages 596–600, 2020.

[57] F. Colone, C. Bongioanni, and P. Lombardo. Multifrequency integration in FM radio-based passive bistatic radar. Part II: Direction of arrival estimation. IEEE Aerospace and Electronic Systems Magazine, 28(4):40–47, April 2013.

[58] Z. Li, F. Santi, D. Pastina, and P. Lombardo. Passive radar array with low-power satellite illuminators based on fractional fourier transform. IEEE Sensors Journal, 17(24):8378–8394, Dec 2017.

[59] Octavio Cabrera, Carlo Bongioanni, Fabiola Colone, and Pierfrancesco Lombardo. Non-coherent dvb-s passive radar demonstrator. In 2020 21st International Radar Symposium (IRS), pages 228–231, 2020.

[60] D. Langellotti, F. Colone, P. Lombardo, M. Sedehi, and E. Tilli. Dvb-t based passive bistatic radar for maritime surveillance. In 2014 IEEE Radar Conference, pages 1197–1202, 2014.

[61] S. Pisa, E. Piuzzi, E. Pittella, P. Lombardo, A. Genovese, D. Bloisi, D. Nardi, P. d'Atanasio, and A. Zambotti. Numerical and experimental evaluation of the radar cross section of a drone. In 2018 15th European Radar Conference (EuRAD), pages 309–312, Sep. 2018.

[62] S. Pisa, E. Piuzzi, E. Pittella, P. Lombardo, N. Ustalli, W. Cao, D. Bloisi, D. Nardi, P. D'Atanasio, and A. Zambotti. Evaluating the radar cross section of the commercial iris drone for anti-drone passive radar source selection. In 2018 22nd International Microwave and Radar Conference (MIKON), pages 699–703, May 2018.

[63] A. Capria, D. Petri, C. Moscardini, M. Conti, A. C. Forti, R. Massini, M. Cerretelli, S. Ledda, V. Tesi, E. Dalle Mese, G. B. Gentili, F. Berizzi, M. Martorella, R. Soleti, T. Martini, and A. Manco. Software-defined Multiband Array Passive Radar (SMARP) demonstrator: A test and evaluation perspective. In OCEANS 2015 - Genova, pages 1–6, 2015.

[64] C. Moscardini and et al. Spatial adaptive processing for passive bistatic radar. In IEEE RadarConf., volume 1, pages 1061–1066, 2014.

[65] Amerigo Capria, Michele Conti, Christian Moscardini, and Fabrizio Berizzi. Software-defined multiband array passive radar (smarp) project: An overview. In 2017 18th International Radar Symposium (IRS), pages 1–9, 2017.

[66] Andrea Manno-Kovacs, E Giusti, Fabrizio Berizzi, and Levente KovÃ¡cs. Image based robust target classification for passive isar. IEEE Sensors Journal, PP:1–1, 10 2018.

[67] H. Kuschel and et al. On the potentials of passive, multistatic, low frequency radars to counter stealth and detect low flying targets. In Proc. of Int. Radar Conf., pages 1–6, 2008.

[68] M Glende, J Heckenbach, H Kuschel, S Müller, J Schell, and C Schumacher. Experimental passive radar systems using digital illuminators (DAB/DVB-T). In Proceedings of the International Radar Symposium (IRS), page 17, 2007.

[69] P. Knott, T. Nowicki, and H. Kuschel. Design of a disc-cone antenna for passive radar in the DVB-T frequency range. In 2011 German Microwave Conference, pages 1–4, March 2011.

[70] G. Bournaka and et al. A two stage beamforming approach for low complexity CFAR detection and localization for passive radar. In 2016 IEEE Radar Conf., pages 1–4, 2016.

[71] Georgia Bournaka, Christoph Schwark, Diego Cristallini, and Heiner Kuschel. Beam space transformation based direction of arrival estimation and auto calibration for a circular array in passive radar. In 2017 IEEE Radar Conference (RadarConf), pages 0745–0748, 2017.

[72] G. Bournaka, M. Ummenhofer, D. Cristallini, J. Palmer, and A. Summers. Experimental study for transmitter imperfections in dvb-t based passive radar. IEEE Transactions on Aerospace and Electronic Systems, 54(3):1341–1354, June 2018.

[73] G. Bournaka, D. W. O'Hagan, and H. Kuschel. Array pattern synthesis techniques for circular array of antennas for passive radar applications. In 2014 11th European Radar Conference, pages 133–136, 2014.

[74] Hongbo Sun, Danny K. P. Tan, and Yilong Lu. Aircraft target measurements using a gsm-based passive radar. In 2008 IEEE Radar Conference, pages 1–6, 2008.

[75] Yuqi Liu, Xianrong Wan, Hui Tang, Jianxin Yi, Yiyao Cheng, and Xun Zhang. Digital television based passive bistatic radar system for drone detection. In 2017 IEEE Radar Conference (RadarConf), pages 1493–1497, 2017.

[76] V. Navrátil, J. L. Garry, A. O'Brien, and G. E. Smith. Utilization of terrestrial navigation signals for passive radar. In 2017 IEEE Radar Conference (RadarConf), pages 0825–0829, 2017.

[77] Jamie H. Huang, Matthew N. Barr, J. L. Garry, and G. E. Smith. Subarray processing for passive radar localization. In 2017 IEEE Radar Conference (RadarConf), pages 0248–0252, 2017.

[78] Jamie H. Huang, J. Landon Garry, Graeme E. Smith, and Danny K.P. Tan. In-field calibration of passive array receiver using detected target. In 2018 IEEE Radar Conference (RadarConf18), pages 0715–0720, 2018.

[79] A. A. Lysko and F. D. V. Maasdorp. South african passive radar and towards its characterisation. In 2017 Progress In Electromagnetics Research Symposium - Spring (PIERS), pages 3795–3801, 2017.

[80] Christof Schüpbach, Christian Patry, Francois Maasdorp, Urs Böniger, and Peter Wellig. Micro-uav detection using dab-based passive radar. In 2017 IEEE Radar Conference (RadarConf), pages 1037–1040, 2017.

[81] F.D.V. Maasdorp, J.E. Cilliers, and C.A. Tong. Propeller modulation analysis of 4-blade, 4-engine aircraft in fm-band multistatic passive radar. In 2020 IEEE International Radar Conference (RADAR), pages 1029–1034, 2020.

[82] J. Lanteri, C. Migliaccio, J-Y. Dauvignac, and Ch. Pichot. Reflectarray using an offset prolate feed at 94 ghz. In 2008 IEEE Antennas and Propagation Society International Symposium, pages 1–4, 2008.

[83] J. Lanteri, A. Zeitler, J.-Y. Dauvignac, Ch. Pichot, C. Migliaccio, P. Feil, and W. Menzel. Investigation of wideband millimetre-wave reflectarrays for radar applications operating in the w band. In 2009 3rd European Conference on Antennas and Propagation, pages 826–830, 2009.

[84] C. Migliaccio, K. Mazouni, A. Bréard, A. Zeitler, J. Lanteri, J. Dauvignac, C. Pichot, N. Yonemoto, A. Kohmura, and S. Futatsumori. Reflectarrays for mm-wave radar applications. In 2011 IEEE International Symposium on Antennas and Propagation (APSURSI), pages 105–108, 2011.

[85] N.T. Nguyen, G. Clementi, C. Migliaccio, N. Fortino, J.-Y. Dauvignac, J. Willebois, and C. Chekroun. Wideband vivaldi antenna array with mechanical support and protection radome for land-mine detection radar. In 2015 European Radar Conference (EuRAD), pages 537–540, 2015.

[86] Alexander G. Yarovoy, Timofey G. Savelyev, Pascal J. Aubry, Pidio Ekoue Lys, and Leo P. Ligthart. Uwb array-based sensor for near-field imaging. IEEE Transactions on Microwave Theory and Techniques, 55(6):1288–1295, 2007.

[87] A.G. Yarovoy, T.G. Savelyev, P.J. Aubry, and L.P. Ligthart. Array-based gpr for shallow subsurface imaging. In 2007 4th International Workshop on, Advanced Ground Penetrating Radar, pages 12–15, 2007.

[88] X. Zhuge, T.G. Savelyev, A.G. Yarovoy, and L.P. Ligthart. Subsurface imaging with uwb linear array: Evaluation of antenna step and array aperture. In 2007 IEEE International Conference on Ultra-Wideband, pages 66–70, 2007.

[89] Oleg A. Krasnov, Leo P. Ligthart, Zhijian Li, Pidio Lys, and Fred van der Zwan. The parsax - full polarimetric fmcw radar with dual-orthogonal signals. In 2008 European Radar Conference, pages 84–87, 2008.

[90] Yanki Aslan, Massimo Candotti, and Alexander Yarovoy. Synthesis of multi-beam space-tapered linear arrays with side lobe level minimization in the presence of mutual coupling. In 2019 13th European Conference on Antennas and Propagation (EuCAP), pages 1–5, 2019.

[91] Simon P. Hehenberger, Alexander Yarovoy, and Andreas Stelzer. A 77-ghz fmcw mimo radar employing a non-uniform 2d antenna array and substrate integrated waveguides. In 2020 IEEE MTT-S International Conference on Microwaves for Intelligent Mobility (ICMIM), pages 1–4, 2020.

[92] H. Kuschel. Passive radar technology. applications. In NATO Lecture Series SET-243. Passive Radar Technology, 2019.

[93] A. Di Lallo, E. Tilli, L. Timmoneri, T. Battisti, and A. Campana. Design, analysis and implementation of a passive integrated mobile system for detection and identification of air targets. In 2012 13th International Radar Symposium, pages 32–36, 2012.

[94] R. Fulcoli, M. Sedehi, E. Telli, and L. Timmoneri. AULOS, A Passive Covert Radar System. In Microwave Yournal, January 2015.

[95] Annarita Di Lallo, Alfonso Farina, Riccardo Fulcoli, Sandro Immediata, Matteo Sedehi, Enrico Tilli, Luca Timmoneri, Annarita Di Lallo, Alfonso Farina, Riccardo Fulcoli, Sandro Immediata, Matteo Sedehi, Enrico Tilli, and Luca Timmoneri. Aulos: Finmeccanica family of passive sensors. IEEE Aerospace and Electronic Systems Magazine, 31(11):24–29, 2016.

[96] R. Mancinelli. AULOS, Italian Passive Coherent Location (PCL). In Virtuelle Instrumente in der Praxis VIP, October 2010.

[97] A. Schroder. Second-generation mobile multiband passive radar demonstrator. 3rd FHR Focus Days on PCL, Wachtberg-Werthhoven, 2011.

[98] A. Schroeder, M. Edrich, and V. Winkler. Multiband PCR systems in multistatic configurations for enhanced air and ground surveillance. In Sensors & Electronics Technology Panel Workshop SET-177 Athens, 2012.

[99] IEEE. IEEE Standard for Definitions of Terms for Antennas. IEEE Std 145-2013 (Revision of IEEE Std 145-1993), pages 1–50, 2014.

[100] Constantine A. Balanis. Antenna Theory: Analysis and Design. John Wiley & Sons, Inc., 2016.

[101] ITU-R.1365. Reference radiation patterns of omnidirectional, sectoral and other antennas for the fixed and mobile services for use in sharing studies in the frequency range from 400 MHz to about 70 GHz. International Telecommunication Union - Radiocommunication Sector, F.1365-5, 2019.

[102] K. Guney and H. Hancer. Improved formulas for narrow and wide aperture dimensions of optimum gain pyramidal horn. Int. J. RF Microwave Computer-aided Eng., 13(3):239–245, 2003.

[103] Constantine A. Balanis. Modern Antenna Handbook. John Wiley & Sons, Ltd, 2008.

[104] Peter J. Gibson. Coplanar patch antenna, US4873529A, 1989.

[105] A. Kumar, J. Kaur, and R. Singh. Performance analysis of different feeding techniques. 2013.

[106] G. A. Deschamp. Microstrip microwave antennas. in Proceedings of the Antenna Applications Symposium, 1953.

[107] J. R. James and P. S. Hall. Handbook of Microstrip Antennas. Peter Peregrinus Ltd., 1989.

[108] A. Sabban. A new broadband stacked two-layer microstrip antenna. In 1983 Antennas and Propagation Society International Symposium, volume 21, pages 63–66, 1983.

[109] G. Kumar and K. P. Ray. Broadband Microstrip Antennas. Artech House, Inc., 2003.

[110] Zi Dong Liu, P. S. Hall, and D. Wake. Dual-frequency planar inverted-f antenna. IEEE Transactions on Antennas and Propagation, 45(10):1451–1458, 1997.

[111] K.L. Wong. Compact and Broadband Microstrip Antennas. John Wiley & Sons, Ltd, 2002.

[112] F. Yang, Xue-Xia Zhang, Xiaoning Ye, and Y. Rahmat-Samii. Wide-band e-shaped patch antennas for wireless communications. IEEE Transactions on Antennas and Propagation, 49(7):1094–1100, 2001.

[113] Jaume Anguera, E. Martinez, C. Puente, C. Borja, and J. Soler. Broad-band dual-frequency microstrip patch antenna with modified sierpinski fractal geometry. IEEE Transactions on Antennas and Propagation, 52(1):66–73, 2004.

[114] B. Biswas, R. Ghatak, and D. R. Poddar. A fern fractal leaf inspired wideband antipodal vivaldi antenna for microwave imaging system. IEEE Transactions on Antennas and Propagation, 65(11):6126–6129, 2017.

[115] W. Stutzman. Synthesis of shaped-beam radiation patterns using the iterative sampling method. IEEE Transactions on Antennas and Propagation, 19(1):36–41, 1971.

[116] Junli Liang, H.C. So, Jian Li, Alfonso Farina, and Deyun Zhou. On optimizations with magnitude constraints on frequency or angular responses. Signal Processing, 145:214–224, 2018.

[117] Microwave Journal. Comprehensive survey of commercial mmwave phased array companies, 2020. Accessed = 2020-12-30.

[118] J. Yang, W. Ryoo, W. Sung, J.-H. Kim, and J. Park. 3d antenna structures using uniform triangular arrays for efficient full-directional multiuser transmission. International Journal of Antennas and Propagation, 2019.

[119] A. J. Fenn, D. J. Pippin, C. M. Lamb, F. G. Willwerth, H. M. Aumann, and J. P. Doane. 3d printed conformal array antenna: Simulations and measurements. In 2016 IEEE International Symposium on Phased Array Systems and Technology (PAST), pages 1–4, 2016.

[120] R.L. Haupt. Thinned arrays using genetic algorithms. IEEE Transactions on Antennas and Propagation, 42(7):993–999, 1994.

[121] D.W. Boeringer and D.H. Werner. Particle swarm optimization versus genetic algorithms for phased array synthesis. IEEE Transactions on Antennas and Propagation, 52(3):771–779, 2004.

[122] Eva Rajo-Iglesias and Oscar Quevedo-Teruel. Linear array synthesis using an ant-colony-optimization-based algorithm. IEEE Antennas and Propagation Magazine, 49(2):70–79, 2007.

[123] Warren L. Stutzman and Gary A. Thiele. Antenna Theory and Design. John Wiley & Sons, third edition, 2012.

[124] Robert J. Mailloux. Phased Array Antenna Handbook. Artech House, Inc., second edition, 2005.

[125] Hubregt J. Visser. Array and Phased Array Antenna Basics. John Wiley & Sons, 2006.

[126] H.L. Van Trees. <u>Optimum array processing: Detection, estimation, and modulation theory</u>. Wiley, 2013.

[127] D. Berry, R. Malech, and W. Kennedy. The reflectarray antenna. <u>IEEE Transactions on Antennas and Propagation</u>, 11(6):645–651, 1963.

[128] J. Baracco, P. Ratajczak, P. Brachat, and G. Toso. Dual frequency ka-band reflectarray for ground terminal application. In <u>The 8th European Conference on Antennas and Propagation (EuCAP 2014)</u>, pages 1437–1440, 2014.

[129] J. A. Encinar, M. Arrebola, L. F. de la Fuente, and G. Toso. A transmit-receive reflectarray antenna for direct broadcast satellite applications. <u>IEEE Transactions on Antennas and Propagation</u>, 59(9):3255–3264, 2011.

[130] C. Tienda, M. Younis, P. Lopez-Dekker, and P. Laskowski. Ka-band reflectarray antenna system for sar applications. In <u>The 8th European Conference on Antennas and Propagation (EuCAP 2014)</u>, pages 1603–1606, 2014.

[131] Y. Shen, S. Hu, and W. Dou. 38 ghz folded reflectarray antenna for point-to-point 5g communications. In <u>2016 IEEE 5th Asia-Pacific Conference on Antennas and Propagation (APCAP)</u>, pages 369–370, 2016.

[132] P. Nayeri, F. Yang, and A.Z. Elsherbeni. <u>REflectarray Antennas</u>. John Wiley & Sons, 2018.

[133] John Huang and José A. Encinar. <u>Reflectarray Antennas</u>. John Wiley & Sons, 2008.

[134] M P Jarabo-Amores, D Mata-Moya, N del Rey-Maestre, P J Gómez del Hoyo, and J Rosado-Sanz. Idepar, uso del radar pasivo para la detección de drones. <u>Boletín de Información Tecnológica en Defensa</u>, 61:11–15, 2019.

[135] Nerea del Rey-Maestre, David Mata-Moya, María-Pilar Jarabo-Amores, Pedro-José Gómez-del Hoyo, José-Luis Bárcena-Humanes, and Javier Rosado-Sanz. Passive radar array processing with non-uniform linear arrays for ground target's detection and localization. <u>Remote Sensing. Special Issue Radar Systems for the Societal Challenges</u>, 9:756, 07 2017.

[136] Hispasat. Hispasat 30w-5 satellite characteristics, 2021. Last accessed: June 2021.

[137] KVH. Astra 1kr coverage, 2021. Last accessed: June 2021.

[138] Levent Sevgi. <u>Complex Electromagnetic Problems and Numerical Simulation Approaches</u>. John Wiley & Sons, 2003.

[139] Ansys. Ansys hfss, 3d electromagnetic field simulator for rf and wireless design, 2020. Last accessed: March 2020.

172

[140] ITU-R.526. Propagation by diffraction. International Telecommunication Union - Radiocommunication Sector, P.526-15, 2019.

[141] ITU-R.530. Datos de propagación y métodos de predicción necesarios para el diseño de sistemas terrenales con visibilidad directa. International Telecommunication Union - Radiocommunication Sector, P.526-13, 2009.

[142] ITU-R.618. Datos de propagación y métodos de predicción necesarios para el diseño de sistemas de telecomunicación tierra-espacio. International Telecommunication Union - Radiocommunication Sector, P.618-13, 2017.

[143] M. Jarabo-Amores, D. Mata-Moya, N. del-Rey-Maestre, J. Rosado-Sanz, and P. Gómez-del-Hoyo. Modelling of drone bistatic rcs fluctuations for uhf passive radar scenarios' simulation. In NATO MSG-SET-183 Specialists' Meeting on "Drone Detectability: Modelling the Relevant Signature, 2020.

[144] V. C. Chen, F. Li, S. . Ho, and H. Wechsler. Micro-doppler effect in radar: phenomenon, model, and simulation study. IEEE Transactions on Aerospace and Electronic Systems, 42(1):2–21, 2006.

[145] S. Björklund and N. Wadströmer. Target detection and classification of small drones by deep learning on radar micro-doppler. In International Radar Conference (RADAR), pages 1–6, 2019.

[146] M. P. Jarabo-Amores, D. Mata-Moya, P. J. Gómez-del-Hoyo, J. L. Bárcena-Humanes, J. Rosado-Sanz, N. Rey-Maestre, and M. Rosa-Zurera. Drone detection feasibility with passive radars. In 2018 15th European Radar Conference (EuRAD), pages 313–316, 2018.

[147] María-Pilar Jarabo-Amores, David Mata-Moya, Pedro-José Gómez-del Hoyo, Nerea del Rey-Maestre, and Javier Rosado-Sanz. On the impact of drone airscrews signature on passive radar detection and tracking stages. In 2020 IEEE Radar Conference (RadarConf20), pages 1–6, 2020.

[148] Caner Ozdemiir. Inverse Synthetic Aperture Radar Imaging and Its Basic Concepts, chapter Four, pages 121–186. John Wiley & Sons, Ltd, 2012.

[149] J. Rosado-Sanz, M.P. Jarabo-Amores, D. Mata-Moya, P.J. Gómez del Hoyo, and N. Del-Rey-Maestre. Broadband modified-circle-shape patch antenna with h-aperture feeding for a passive radar array. Aerospace Science and Technology, 110:106445, 2021.

[150] D.E. Goldberg. Genetic Algorithm in Search, Optimization and Machine Learning. Addison-Wesley, 1989.

[151] J. Rosado-Sanz, N. Rey-Maestre, D. Mata-Moya, M. P. Jarabo-Amores, M. Rosa-Zurera, and J. L. Bárcena-Humanes. Advantages of non-uniform linear arrays based on cots elements in passive radar applications. In 2018 22nd International Microwave and Radar Conference (MIKON), pages 199–203, 2018.

[152] R. Carrel. The design of log-periodic dipole antennas. In 1958 IRE International Convention Record, volume 9, pages 61–75, 1961.

[153] J. Rosado-Sanz, M. Jarabo-Amores, D. Mata-Moya, N. del-Rey-Maestre, and P. Gomez-del-Hoyo. Design of a broadband patch antenna for a dvb-t based passive radar antenna array. In 2017 IEEE 17th International Conference on Ubiquitous Wireless Broadband (ICUWB), pages 1–5, 2017.

[154] Sumanpreet Kaur Sidhu and J. S. Sivia. Comparison of different types of microstrip patch antennas. 2015.

[155] Robert Michael Lewis and Virginia Torczon. Pattern search methods for linearly constrained minimization. SIAM Journal on Optimization, 10(3):917–941, 2000.

[156] N. del-Rey-Maestre, J. Rosado-Sanz, P. Gómez-del-Hoyo, D. Mata-Moya, and M. P. Jarabo-Amores. Coherent vi-mlp-cfar detector for idepar demonstrator (dvb-t passive radar) in ground traffic monitoring. In 2017 IEEE International Instrumentation and Measurement Technology Conference (I2MTC), pages 1–6, 2017.

[157] Nerea Del-Rey-Maestre, María-Pilar Jarabo-Amores, David Mata-Moya, Anabel Almodóvar-Hernández, and Pedro-José Gómez-del Hoyo. A dvb-t passive radar 3d-detection approach based on non-coherent spatial integration. In 2020 17th European Radar Conference (EuRAD), pages 362–365, 2021.

[158] W. Menzel, M. Al-Tikriti, and R. Leberer. A 76 ghz multiple-beam planar reflector antenna. In 2002 32nd European Microwave Conference, pages 1–4, 2002.

[159] Min Zhou and Stig B. Sørensen. Multi-spot beam reflectarrays for satellite telecommunication applications in ka-band. In 2016 10th European Conference on Antennas and Propagation (EuCAP), pages 1–5, 2016.

[160] J. Rosado-Sanz, M. P. Jarabo-Amores, D. Mata-Moya, P. J. Gómez-del-Hoyo, and N. Del-Rey-Maestre. Contoured-beam reflectarray for improving angular coverage in dvb-s passive radars. In 2019 20th International Radar Symposium (IRS), pages 1–8, 2019.

[161] M. I. Skolnik. Radar Handbook. 3th Ed. Mc-Graw Hill, 2008.

[162] M. Valeri, S. Barbarossa, A. Farina, and L. Timmoneri. Monopulse estimation of target doa in external noise fields with adaptive arrays. In Proceedings of International Symposium on Phased Array Systems and Technology, pages 386–390, 1996.

[163] J.A. Zornoza, R. Leberer, J.A. Encinar, and W. Menzel. Folded multilayer microstrip reflectarray with shaped pattern. IEEE Transactions on Antennas and Propagation, 54(2):510–518, 2006.

[164] Min Zhou, Stig B. Sørensen, Oleksiy S. Kim, Erik Jørgensen, Peter Meincke, and Olav Breinbjerg. Direct optimization of printed reflectarrays for contoured beam satellite antenna applications. IEEE Transactions on Antennas and Propagation, 61(4):1995–2004, 2013.

[165] J. Rosado-Sanz, M.P. Jarabo-Amores, D. Mata-Moya, J.Y. Dauvignac, J. Lanteri, and C. Migliaccio. High gain sectorial beam reflectarray design for dvb-s passive radar through multi-beam optimization. In 2020 23rd International Microwave and Radar Conference (MIKON), pages 361–366, 2020.

[166] J. Kennedy and R. Eberhart. Particle swarm optimization. In Proceedings of ICNN'95 - International Conference on Neural Networks, volume 4, pages 1942–1948 vol.4, 1995.

[167] P. Potter. A new horn antenna with suppressed sidelobes and equal beamwidths. In Microwave Journal, pages 71–78, 1963.

[168] J. Lanteri, C. Migliaccio, J-Y. Dauvignac, and Ch. Pichot. Improvement of reflectarrays and lenses radiation pattern by prolate spheroidal functions in w band. In Proccedings of EUCAP 2006, 2006.

[169] IEEESTD. Ieee standard test procedures for antennas. ANSI/IEEE Std 149-1979, 1979.

[170] RemoteQTH. 10 ghz lnb plus bias-tee. Last accessed: May 2021.

[171] M. Jarabo-Amores, D. Mata-Moya, N. del-Rey-Maestre, P. Gómez-del-Hoyo, and J. Rosado-Sanz. Passive radar distributed sensor network for detecting silent aerial and maritime targets in coastal waters. In NATO SET-284 Specialists' Meeting on Enhanced Situation Awareness using Active-Passive Radar Systems in Military Scenarios, 2020.

[172] P. J. Gómez-del-Hoyo, M. P. Jarabo-Amores, D. Mata-Moya, J. Rosado-Sanz, and N. Del-Rey-Maestre. Dvb-s based passive radar for ground targets detection and tracking. In 7th PCL Focus Days 2019, 2019.

[173] M. Jarabo-Amores, D. Mata-Moya, P. Gómez-del-Hoyo, N. del-Rey-Maestre, and J. Rosado-Sanz. On the impact of drone airscrews signature on passive radar detection and tracking. In IEEE Radar Conference, 2020.

[174] Javier Rosado-Sanz, María-Pilar Jarabo-Amores, David Mata-Moya, Pedro Gomez-del Hoyo, and Mari-Cortes Benito-Ortiz. Conductivity estimation of composite materials used on uav airframes. In 2018 IEEE Conference on Antenna Measurements Applications (CAMA), pages 1–4, 2018.

[175] J. Rosado-Sanz, M.-P. Jarabo-Amores, P.-J. Gómez-Hoyo, N. del Rey-Maestre, and D. Mata-Moya. Validation of a broadband E-shaped antenna in a real semi-urban passive radar scenario. In 2017 42nd International Conference on Infrared, Millimeter, and Terahertz Waves (IRMMW-THz), pages 1–2, 2017.

[176] J. Rosado-Sanz, M. P. Jarabo-Amores, D. Mata-Moya, N. del Rey-Maestre, and J. L. Bárcena-Humanes. Sll optimization of passive radar non-uniform linear arrays based on commercial uhf antennas. In 2017 International Conference on Control, Artificial Intelligence, Robotics Optimization (ICCAIRO), pages 89–92, 2017.

[177] M. Jarabo-Amores, D. Mata-Moya, N. del-Rey-Maestre, P. Gómez-del-Hoyo, J. Rosado-Sanz, and M. Benito-Ortiz. Idepar, radar pasivo basado en tdt, en entornos costeros. In VII Congreso Nacional de I+D en Defensa y Seguridad (DESEi+d 2019), 2019.

[178] N. del-Rey-Maestre, P. Gomez-del-Hoyo, J. Rosado-Sanz, D. Mata-Moya, M. Jarabo-Amores, and F.G. Gaitan-Caba nas. Validación de radares pasivos basados en la tdt para la detección de drones. In Congreso Nacional de I+D en Defensa y Seguridad (DESEi+d 2018), pages 1–8, 2018.

[179] A. Almodovar-Hernandez, M. Jarabo-Amores, D. Mata-Moya, P. Gómez-del-Hoyo, and J. Rosado-Sanz. Study of the effect of wideband sparse frequency signals in uhf passive radar resolution. In The 9th Microwave and Radar Week (MRW2020), 2020.

[180] N. del-Rey-Maestre, D. Mata-Moya, M. Jarabo-Amores, P. Gomez-del-Hoyo, and J. Rosado-Sanz. Optimum beamforming to improve uav's detection using dvb-t passive radars. In 2019 International Radar Conference (RADAR), pages 1–6, 2019.

[181] J. L. Bárcena-Humanes, P. J. Gómez-del-Hoyo, M. P. Jarabo-Amores, J. Rosado-Sanz, and M. C. Benito-Ortiz. First approach to motion compensation considerations for passive radar system based on gps signals. In 2018 19th International Radar Symposium (IRS), pages 1–10, 2018.

[182] N. del Rey-Maestre, J.-L. Bárcena-Humanes, J. Rosado-Sanz, P.-J. Gómez-del Hoyo, and D. Mata-Moya. Nondesired effects in DVB-T based passive radar due to sporadic interference. In 2017 Signal Processing Symposium (SPSympo), pages 1–6, 2017.

176

[183] N. Del-Rey-Maestre, D. Mata-Moya, M. P. Jarabo-Amores, J. Rosado-Sanz, P. G. Del-Rey-Maestre, D. Mata-Moya, M. Jarabo-Amores, J. Rosado-Sanz, and P. Gomez-del-Hoyo. Doa estimation based on a ula of commercial antennas in semi-urban passive radar scenario. In 2017 International Conference on Control, Artificial Intelligence, Robotics Optimization (ICCAIRO), pages 74–77, 2017.

[184] J.-L. Bárcena-Humanes, P.-J. Gómez-del Hoyo, M.-P. Jarabo-Amores, D. Mata-Moya, and J. Rosado-Sanz. On the potentials of satellite based passive radars for smart sensors networks in smart cities. In 2017 IEEE 17th International Conference on Ubiquitous Wireless Broadband (ICUWB), pages 1–5, 2017.

[185] N. del Rey-Maestre, J.-L. Bárcena-Humanes, J. Rosado-Sanz, P.-J. Gómez-del Hoyo, and D. Mata-Moya. DVB-T based passive radar performance sensitivity with respect to channel availability. In 2017 European Radar Conference (EURAD), pages 183–186, 2017.